Stochastic representation and analysis of rough surface topography by random fields and integral geometry – Application to the UHMWPE cup involved in total hip arthroplasty

Ola Ahmad

Ecole Nationale Supérieure des Mines
SAINT-ETIENNE

NNT : 2013 EMSE 0704

THÈSE

présentée par

Ola AHMAD

pour obtenir le grade de
Docteur de l'École Nationale Supérieure des Mines de Saint-Étienne

Spécialité : **Image, Vision, Signal**

STOCHASTIC REPRESENTATION AND ANALYSIS OF ROUGH SURFACE TOPOGRAPHY BY RANDOM FIELDS AND INTEGRAL GEOMETRY

Application to the UHMWPE cup involved in total hip arthroplasty

soutenue à Saint-Étienne, le XX Septembre 2013

Membres du jury

Président :	Philippe KAPSA	Professeur, ECL (Lyon)
Rapporteurs :	Michel SCHMITT	Directeur de recherche, MINES ParisTech (Paris)
	Marc ARNOUDON	Professeur, IMB (Bordeaux)
Examinateur(s) :	Olivier GUYEN	Professeur, CHU et UFR (Lyon)
Co-encadrant :	Yann GAVET	Docteur, ENSMSE (Saint-Étienne)
	Jean GERINGER	Docteur, ENSMSE (Saint-Étienne)
Co-directeur :	Frédéric FARIZON	Professeur, UJM et CHU (Saint-Étienne)
Directeur de thèse :	Jean-Charles PINOLI	Professeur, ENSMSE (Saint-Étienne)
Invité éventuel:	Maxence BIGERELLE	Professeur, UVHC (Valenciennes)

Spécialités doctorales :	Responsables :
SCIENCES ET GENIE DES MATERIAUX	K. Wolski Directeur de recherche
MECANIQUE ET INGENIERIE	S. Drapier, professeur
GENIE DES PROCEDES	F. Gruy, Maître de recherche
SCIENCES DE LA TERRE	B. Guy, Directeur de recherche
SCIENCES ET GENIE DE L'ENVIRONNEMENT	D. Graillot, Directeur de recherche
MATHEMATIQUES APPLIQUEES	O. Roustant, Maître-assistant
INFORMATIQUE	O. Boissier, Professeur
IMAGE, VISION, SIGNAL	JC. Pinoli, Professeur
GENIE INDUSTRIEL	A. Dolgui, Professeur
MICROELECTRONIQUE	

EMSE : Enseignants-chercheurs et chercheurs autorisés à diriger des thèses de doctorat (titulaires d'un doctorat d'État ou d'une HDR)

AVRIL	Stéphane	PR2	Mécanique et ingénierie	CIS
BATTON-HUBERT	Mireille	PR2	Sciences et génie de l'environnement	FAYOL
BENABEN	Patrick	PR1	Sciences et génie des matériaux	CMP
BERNACHE-ASSOLLANT	Didier	PR0	Génie des Procédés	CIS
BIGOT	Jean Pierre	MR(DR2)	Génie des Procédés	SPIN
BILAL	Essaid	DR	Sciences de la Terre	SPIN
BOISSIER	Olivier	PR1	Informatique	FAYOL
BORBELY	Andras	MR(DR2)	Sciences et génie de l'environnement	SMS
BOUCHER	Xavier	PR2	Génie Industriel	FAYOL
BRODHAG	Christian	DR	Sciences et génie de l'environnement	FAYOL
BURLAT	Patrick	PR2	Génie Industriel	FAYOL
COURNIL	Michel	PR0	Génie des Procédés	DIR
DARRIEULAT	Michel	IGM	Sciences et génie des matériaux	SMS
DAUZERE-PERES	Stéphane	PR1	Génie Industriel	CMP
DEBAYLE	Johan	CR	Image Vision Signal	CIS
DELAFOSSE	David	PR1	Sciences et génie des matériaux	SMS
DESRAYAUD	Christophe	PR2	Mécanique et ingénierie	SMS
DOLGUI	Alexandre	PR0	Génie Industriel	FAYOL
DRAPIER	Sylvain	PR1	Mécanique et ingénierie	SMS
FEILLET	Dominique	PR2	Génie Industriel	CMP
FOREST	Bernard	PR1	Sciences et génie des matériaux	CIS
FORMISYN	Pascal	PR0	Sciences et génie de l'environnement	DIR
FRACZKIEWICZ	Anna	DR	Sciences et génie des matériaux	SMS
GARCIA	Daniel	MR(DR2)	Génie des Procédés	SPIN
GERINGER	Jean	MA(MDC)	Sciences et génie des matériaux	CIS
GIRARDOT	Jean-jacques	MR(DR2)	Informatique	FAYOL
GOEURIOT	Dominique	DR	Sciences et génie des matériaux	SMS
GRAILLOT	Didier	DR	Sciences et génie de l'environnement	SPIN
GROSSEAU	Philippe	DR	Génie des Procédés	SPIN
GRUY	Frédéric	PR1	Génie des Procédés	SPIN
GUY	Bernard	DR	Sciences de la Terre	SPIN
GUYONNET	René	DR	Génie des Procédés	SPIN
HAN	Woo-Suck	CR	Mécanique et ingénierie	SMS
HERRI	Jean Michel	PR1	Génie des Procédés	SPIN
INAL	Karim	PR2	Microélectronique	CMP
KERMOUCHE	Guillaume	PR2	Mécanique et Ingénierie	SMS
KLOCKER	Helmut	DR	Sciences et génie des matériaux	SMS
LAFOREST	Valérie	MR(DR2)	Sciences et génie de l'environnement	FAYOL
LERICHE	Rodolphe	CR	Mécanique et ingénierie	FAYOL
LI	Jean Michel		Microélectronique	CMP
MALLIARAS	Georges	PR1	Microélectronique	CMP
MOLIMARD	Jérôme	PR2	Mécanique et ingénierie	CIS
MONTHEILLET	Franck	DR	Sciences et génie des matériaux	SMS
PERIER-CAMBY	Laurent	PR2	Génie des Procédés	DFG
PIJOLAT	Christophe	PR0	Génie des Procédés	SPIN
PIJOLAT	Michèle	PR1	Génie des Procédés	SPIN
PINOLI	Jean Charles	PR0	Image Vision Signal	CIS
POURCHEZ	Jérémy	CR	Génie des Procédés	CIS
ROUSTANT	Olivier	MA(MDC)		FAYOL
STOLARZ	Jacques	CR	Sciences et génie des matériaux	SMS
SZAFNICKI	Konrad	MR(DR2)	Sciences et génie de l'environnement	CMP
TRIA	Assia		Microélectronique	CMP
VALDIVIESO	François	MA(MDC)	Sciences et génie des matériaux	SMS
VIRICELLE	Jean Paul	MR(DR2)	Génie des Procédés	SPIN
WOLSKI	Krzystof	DR	Sciences et génie des matériaux	SMS
XIE	Xiaolan	PR1	Informatique	CIS

ENISE : Enseignants-chercheurs et chercheurs autorisés à diriger des thèses de doctorat (titulaires d'un doctorat d'État ou d'une HDR)

BERGHEAU	Jean-Michel	PU	Mécanique et Ingénierie	ENISE
BERTRAND	Philippe	MCF	Génie des procédés	ENISE
DUBUJET	Philippe	PU	Mécanique et Ingénierie	ENISE
FORTUNIER	Roland	PR	Sciences et Génie des matériaux	ENISE
GUSSAROV	Andrey	Enseignant contractuel	Génie des procédés	ENISE
HAMDI	Hédi	MCF	Mécanique et Ingénierie	ENISE
LYONNET	Patrick	PU	Mécanique et Ingénierie	ENISE
RECH	Joël	MCF	Mécanique et Ingénierie	ENISE
SMUROV	Igor	PU	Mécanique et Ingénierie	ENISE
TOSCANO	Rosario	MCF	Mécanique et Ingénierie	ENISE
ZAHOUANI	Hassan	PU	Mécanique et Ingénierie	ENISE

Mise à jour : 07/04/2013

PR 0	Professeur classe exceptionnelle
PR 1	Professeur 1ère classe
PR 2	Professeur 2ème classe
PU	Professeur des Universités
MA (MDC)	Maître assistant
DR	Directeur de recherche

Ing.	Ingénieur
MCF	Maître de conférences
MR (DR2)	Maître de recherche
CR	Chargé de recherche
EC	Enseignant-chercheur
IGM	Ingénieur général des mines

SMS	Sciences des Matériaux et des Structures
SPIN	Sciences des Processus Industriels et Naturels
FAYOL	Institut Henri Fayol
CMP	Centre de Microélectronique de Provence
CIS	Centre Ingénierie et Santé

Résumé étendu

La topographie d'une surface se compose généralement de plusieurs échelles, depuis l'échelle macroscopique (sa géométrie physique), jusqu'aux échelles microscopiques ou atomiques appelées rugosité. L'évolution spatiale et géométrique de la rugosité de surface fournit une description plus complète de l'état de ses microstructures, et une interprétation physique des certains problèmes importants tels que le frottement et les mécanismes d'usure pendant le contact mécanique entre deux surfaces. La topographie d'une surface rugueuse est de nature aléatoire. Cela se traduit par des altitudes spatialement corrélées, appelées pics et vallées. La relation entre leurs densités de probabilité, et leurs propriétés géométriques sont les aspects fondamentaux qui ont été développés dans cette thèse, en utilisant la théorie des champs aléatoires et la géométrie intégrale.

Un modèle aléatoire approprié pour représenter une surface rugueuse a été mis en place et étudié au moyen des paramètres les plus significatifs, dont les changements influencent la géométrie des ensembles de niveaux (excursion sets) de cette surface, constitués des points avec des hauteurs supérieures à un seuil donné. Les ensembles de niveaux ont été quantifiés par des fonctionnelles connues sous le nom de fonctionnelles de Minkowski, ou d'une manière équivalente sous le nom de volumes intrinsèques. Ces fonctionnelles ont en pratique plusieurs interprétations physiques. Leurs formules analytiques permettent d'estimer les paramètres du modèle de surface, et d'apporter une analyse statistique de ses ensembles de niveaux et de la rugosité. Ces sujets ont été essentiellement considérés dans cette thèse.

Dans un premier temps, les volumes intrinsèques des ensembles de niveaux sont calculés analytiquement sur une classe de modèles mixtes, qui sont définis par la combinaison linéaire d'un champ aléatoire Gaussien et d'un champ de $t-$student ($t-$field), et ceux d'une classe de champs aléatoires asymétriques appelés skew$-t$. Ces volumes sont comparés et testés sur des surfaces produites par des simulations numériques.

Dans un second temps, les modèles aléatoires proposés ont été appliqués sur des surfaces réelles acquises à partir d'une cupule d'UHMWPE (Ultra-High-Molecular-Weight Polyéthylène), utilisée pour une prothèse totale de hanche, avant et après les processus d'usure. Les résultats ont montré que le champ aléatoire skew$-t$ est un modèle mieux approprié pour décrire la rugosité de surfaces usées, contrairement aux modèles Gaussien et skew$-$Gaussien adoptés dans la littérature. Une analyse statistique, basée sur le champ aléatoire skew$-t$, est ensuite proposée. Elle vise à estimer hiérarchiquement les ensembles de niveaux comprenant les pics/vallées affectés par l'usure. L'évolution de la moyenne des pics/vallées détectés à ces niveaux a permis de décrire le comportement de la surface d'UHMWPE en fonction du temps d'usure, et d'indiquer les mécanismes d'usure prédominants. Les résultats obtenus sont prometteurs, et des développements ultérieurs théoriques et pratiques

sont proposés.

Mot-clés : Champs Aléatoires ; Géométrie Intégrale ; Ensembles de Niveaux ; Volumes Intrinsèques ; Rugosité ; Topographie ; Simulation ; Caractérisation ; Analyse Statistique ; Usure Mécanique ; UHMWPE (Ultra-High-Molecular-Weight Polyéthylène).

Organisation du manuscrit

Le manuscrit présente tout d'abord une introduction générale à la thèse. Celle-ci expose la problématique au niveau médical et scientifique, pour introduire les motivations et le but de ce travail de recherche.

Ensuite, il est composé de cinq parties.

Première partie : Caractérisation de la rugosité de la topographie de surface

La première partie (Part I) présente une étude bibliographique sur la caractérisation de la rugosité de la topographie de surface. Les approches classiques et standards provenant de la métrologie de surface sont d'abord introduites, pour exposer les paramètres de la rugosité de surface, et les fonctions caractéristiques comme la courbe d'Abbott-Firestone et la fonction d'autocorrèlation. Les méthodes basées sur l'étude géométrique des ensembles de niveaux de surface ont permis de définir des fonctionnelles géométriques caractéristiques appelées volumes intrinsèques ou fonctionnelles de Minkowski. Ces dernières sont liées à la courbe d'Abbott-Firestone ainsi qu'aux paramètres de rugosité. Des méthodes basées sur la modélisation de la topographie de surface sont également introduites pour décrire la rugosité. Les avantages et les limitations sont présentés, afin de démontrer l'importance et la motivation de l'étude théorique des champs aléatoires intégrée avec l'étude de la géométrie de leurs ensembles de niveaux, pour repondre au probléme pratique constitué par l'évolution de la rugosité de surface.

Deuxième partie : Champs aléatoire et géométrie intégrale

La deuxième partie (Part II) de ce manuscrit est consacrée aux principes théoriques et fondamentaux des champs aléatoires et de la géométrie intégrale de leurs ensembles de niveaux (excursion sets).
Le chapitre 2 porte sur les champs aléatoires et leurs propriétés mathématiques, stationnarité au sens faible, stationnarité au sens fort, isotropie, anisotropie, et représentation spectrale. Le champ aléatoire gaussien a été essentiellement introduit en tant que brique de base. Ce dernier est uniquement défini par les moments d'ordre un et deux, la moyenne et la fonction de covariance, respectivement,

afin d'introduire des modèles aléatoires à base de gaussien, appelés les gaussiens-associés, comme les champs $t-$field, χ^2, $F-$field, etc. Ces derniers ont des propriétés intéressantes en pratique, et leur loi de probabilité marginale est asymptotiquement simple et bien définie analytiquement. Celle-ci a permis d'étudier la géometrie des ensembles de niveaux de ces modèles, et de fournir des formules asymptotiques de certaines mesures de ces ensembles, comme les mesures de Minkowski.

Le chapitre 3 porte sur la géométrie intégrale des champs aléatoires. Ce chapitre poursuit les rappels des ensembles de niveaux des champs aléatoires, et présente les outils théoriques nécessaires pour estimer les mesures géométriques et topologiques de ces ensembles aléatoires. Ces mesures sont les volumes intrinsèques (d'une manière équivalente les fonctionnelles de Minkowski) : l'aire, le périmètre et le nombre d'Euler-Poincaré pour une ensemble bi-dimensionnel. Des formules explicites des volumes intrinsèques peuvent être obtenues pour les champs aléatoires gaussiens et les gaussiens-associés qui respectent certaines conditions de régularité, en utilisant la formule de Hadwiger et la théorie de Morse. En pratique, les formules explicites permettent d'estimer les paramètres caractéristiques d'une surface aléatoire, et de fournir une description complète de l'état de la surface.

Cependant, les champs aléatoires introduits dans l'état de l'art de ce manuscrit ne sont pas suffisants pour l'application proposée, ce qui justifie les développements théoriques de cette thèse.

Troisième partie : Développements théoriques

Cette troisième partie (Part III) est consacrée aux développements réalisés durant cette thèse dans le domaine théorique des champs aléatoires et dans l'estimation des volumes intrinsèques de leurs ensembles de niveaux en formules analytiques explicites. Cette partie comporte deux chapitres. Le premier chapitre (chapitre 4) introduit une classe de champs aléatoires mixtes créés par la combinaison linéaire d'un champ gaussien et d'un champ appelé $t-$field. Le deuxième chapitre de cette partie (chapitre 5) est consacré aux modèles aléatoires asymétriques, précisement les champs aléatoires skew$-t$. Les volumes intrinsèques appelés également Lipschitz-Killing curvatures (LKCs) ont été calculés explicitement, dans l'espace euclidien $\mathbb{R}^N$, pour les modèles de ces deux chapitres, en étendant les résultats publiés dans la littérature pour les modèles gaussiens et gaussiens-associés. Les nombres moyens des valeurs extrêmes (maxima/minima) ont été aussi estimés, et la relation entre ces nombres moyens et la fonction d'Euler-Poincaré caractéristique a été également établie. Des résultats de simulations numériques dans ces deux chapitres sont présentés.

Quatrième partie : Application

La quatrième partie (Part IV) concerne une application de la prothèse totale de hanche. L'étude théorique introduite dans la partie précédente a été initiée par un problème pratique : l'analyse de l'évolution de rugosité, et la caractérisation de la

topographie des surfaces représentées par des modèles stochastiques durant l'usure mécanique. Ce problème pratique est associé à l'application médicale proposée pour cette thèse : les cupules UHMWPE (Ultra-High-Molecular-Weight Polyethylene) utilisées dans certaines prothèses totales de hanche. Le but de ce problème pratique est de mettre en oeuvre des outils pour décrire le comportement de UHMWPE avec l'usure, afin d'améliorer la durée des implants prothétiques de la hanche.

Le premier chapitre (chapitre 6) de cette partie pose précisément l'application médicale : les principes de la prothèse totale de hanche, le choix des matériaux utilisés pour ces prothèses, et les problèmes principaux rapportés avec les matériaux utilisés, en particulier l'usure de la surface de UHMWPE. Le chapitre 7 établit les développements expérimentaux : il explore les dispositifs expérimentaux aboutissant à générer artificiellement (*in-vitro*) l'usure sur la surface UHMWPE, et les outils techniques exploités pour observer les surfaces usées et pour fournir la carte de rugosité.

Le chapitre 8 met en pratique les développements théoriques précédents sur les surfaces réelles observées concrètement sur la cupule de UHMWPE avant et pendant le processus d'usure. Ensuite, une analyse statistique, basée sur les volumes intrinsèques des ensembles de niveaux du champ aléatoire skew$-t$, a été proposée. Elle permet d'estimer l'évolution des pics/vallées affectés par l'usure, en considérant que ces dernières sont du même ordre de grandeur que l'erreur systématique (l'erreur de mesures). Ainsi, un seuillage a été établi hiérarchiquement sur la surface en utilisant la fonction d'Euler-Poincaré caractéristique du model aléatoire skew$-t$. L'aire moyenne de pics/vallées détectés et leurs niveaux d'altitudes sont ensuite calculés et utilisés pour présenter l'évolution de paramètres de rugosités fonctionnelles qui décrivent le comportement et la fonctionnalité de la surface avec l'usure.

Cette analyse a été appliquée à huit échantillons observés autour de différentes régions de la surface hémisphérique de UHMWPE, telles que les régions aux latitudes à 45° et 100°. Les résultats ont démontré que les zones à 100° sont beaucoup moins affectées par l'usure, contrairement aux zones à 45°. Cela indique un comportement non-homogène du mécanisme d'usure sur les zones observées aux différentes latitudes de la cupule. Les résultats ont également montré que le comportement de la surface de UHMWPE, pour les échantillons mesurés autour la zone la plus usée (c'est-à-dire la zone à 45° de latitude) est homogène, et contrôlé, d'une manière alternative par deux types d'usure appelés abrasion et adhésion.

Cinqième partie : Conclusion générale et perspectives

La dernière partie (Part V) de ce manuscrit conclut le travail de cette thèse. Le chapitre 9 présente tout d'abord des perspectives, sur la modélisation spatio-temporelle. Il introduit le modèle skew$-t$ dans l'espace et temps, et présente les formules explicites des volumes intrinsèques de ses ensembles de niveaux. L'approche spatio-temporelle portée sur les champs aléatoires fournit des outils très intéressants et originaux sur la modélisation de la topographie de surface, l'analyse spatio-temporelle de sa rugosité pendant le temps d'usure, et la prédiction de

la fonctionnalité de la surface au travers des paramètres de rugosité prévus. Cependant, ce travail nécessite de conduire des investigations théoriques et pratiques supplémentaires.

Le chapitre 10 tire une conclusion générale qui récapitule la thèse et fournit les suggestions et les idées utiles pour d'autres améliorations, et ouvre la discussion vers des domaines différents d'application.

Finalement, les annexes sont composées de deux chapitres. La premier chapitre expose les théorèmes et les lemmes utilisés pour calculer les volumes intrinsèques des modèles proposés dans la deuxième partie du manuscrit. Le chapitre suivant introduit les outils pratiques pour générer la topographie des surfaces à partir des modèles aléatoires gaussiens isotropes et/ou anisotropes à partir de la représentation spectrale (transformée de Fourier) ou de la décomposition orthogonale de la matrice de covariance, suivis d'illustrations de simulation numérique.

List of publications

Part of the contributions and publications introduced in the following list belongs to the Ph.D. thesis, and another part has been written and published during the Ph.D. on research work related to my M.Sc. Thesis.

Journal papers:

[1]. O. Ahmad, J. Debayle, and J.-C. Pinoli. "A geometric-based method for recognizing overlapping polygonal-shaped and semi-transparent particles in gray tone images", *Pattern Recognition Letters* 32(15), 2068–2079, 2011.

[2]. O. Ahmad, J. Debayle, N. Gherras, B. Presles, G. Févotte, and J.-C. Pinoli. "Quantification of overlapping polygonal-shaped particles based on a new segmentation method of in situ images during crystallization.", *Journal of Electronic Imaging*, 21(2), 021115, 2012.

[3]. O. Ahmad and J.-C. Pinoli. "On the linear combination of the Gaussian and student's t random field and the integral geometry of its excursion sets", *Statistics & Probability Letters*, 83(2), 559–567, 2013. (Ph.D. Thesis research)

[4]. O. Ahmad and J.-C. Pinoli. "Lipschitz-Killing Curvatures of the Excursion Sets of Skew Student's t Random Fields.", *Stochastic Models - Taylor & Francis*, 29(2), 273–289, 2013. (Ph.D. Thesis research)

[5]. O. Ahmad, Y. Gavet, J. Geringer and J.-C. Pinoli. "Statistical analyses of worn surfaces using skew student's t random field and the integral geometry of its excursion sets", *SIAM Journal on Imaging Sciences*, In review. (Ph.D. Thesis research)

Conference and proceeding's papers:

[1]. O. Ahmad, J. Debayle, N. Gherras, B. Presles, G. Févotte, and J.-C. Pinoli. "Recognizing overlapped particles during a crystallization process from in situ video images for measuring their size distributions.", *In 10th SPIE International Conference on Quality Control by Artificial Vision (QCAV)*, Saint-Etienne, France, June 2011.

[2]. O. Ahmad, N. Gherras, J. Debayle, B. Presles, G. Févotte, and J.-C. Pinoli. "Recognizing overlapped particles during a crystallization process from in situ video images for measuring their size distributions.", *In International Symposium on Industrial Crystallization (ISIC)*, Zurich, Switzerland, 2011.

[3]. O. Ahmad, J. Debayle, N. Gherras, G. Févotte, and J.-C. Pinoli. "Mesure de la distribution granulométrique de cristaux aciculaires par analyse d'images acquises á l'aide d'une sonde vidéo in situ.", *In Proceedings of the SFGP*, 2011.

[4]. O. Ahmad and J.-C. Pinoli. "On the linear combination of the Gaussian and student's t random field and the integral geometry of its excursion sets",

Proceedings of The World Congress on Engineering and Computer Science, San Francisco, USA, 2012, pp604-608. (Ph.D. Thesis research)

[5]. O. Ahmad and J.-C. Pinoli. "Lipschitz-Killing Curvatures of the Excursion Sets of Skew Student-t Random Fields", *Proceedings of 2nd Annual International Conference on Computational Mathematics, Computational Geometry & Statistics*, Singapore, 2013, pp140-147. (Ph.D. Thesis research)

[6]. O. Ahmad, Y. Gavet, J. Geringer and J.-C. Pinoli."Roughness variability estimation of microscopic surfaces during engineering wear process–Application to total hip implant", *In 11th International Conference on Quality Control by Artificial Vision*, Fukuoka, Japan, 2013. (Ph.D. Thesis research)

Awards of the Ph.D. thesis

Best conference proceeding's paper award at CMCGS 2013:

– O. Ahmad and J.-C. Pinoli. "Lipschitz-Killing Curvatures of the Excursion Sets of Skew Student-t Random Fields", *Proceedings of 2nd Annual International Conference on Computational Mathematics, Computational Geometry & Statistics*, Singapore, 2013, pp140-147.

Contents

Introduction **1**
Preface . . . 1
Medical Issue . . . 1
Scientific Issue . . . 1
Aimes and Scopes . . . 2
Thesis Outline . . . 3

I SURFACE CHARACTERIZATION **5**

1 Characterization of surface topography **7**
1.1 Introduction . . . 7
1.2 Surface metrology . . . 8
1.2.1 Two-dimensional approaches . . . 8
1.2.2 Three-dimensional approaches . . . 8
1.3 Geometry of level sets for surface characterization and analysis . . . 12
1.4 Surface roughness representation . . . 13
1.4.1 Wavelet models . . . 13
1.4.2 Fractal models . . . 13
1.4.3 Numerical models . . . 14
1.4.4 Random field models . . . 15
1.5 Conclusion . . . 16

II RANDOM FIELDS THEORY AND THEIR GEOMETRY **17**

2 Random Fields Theory **19**
2.1 Random fields . . . 19
2.1.1 Definition . . . 19
2.2 Stationarity, Isotropy, and Anisotropy . . . 20
2.2.1 Stationarity . . . 20
2.2.2 Isotropy . . . 21
2.2.3 Anisotropy . . . 21
2.2.4 Spectral representation on $\mathbb{R}^N$ . . . 21
2.3 Gaussian random fields . . . 22
2.3.1 Definition . . . 22
2.3.2 Spectral moments of Gaussian random fields . . . 23
2.4 Non-Gaussian random fields . . . 24
2.5 Conclusion . . . 25

3 Geometry of random fields **27**
3.1 Excursion sets . . . 27
3.2 Regularity conditions . . . 28
3.3 Expectations . . . 29
3.3.1 Case of isotropy . . . 29
3.3.2 Non-isotropic random fields on smooth manifolds . . . 30
3.3.3 Stationary random fields over rectangles on $\mathbb{R}^N$ . . . 31
3.4 Mean intrinsic volumes of excursion sets . . . 32
3.5 Conclusion . . . 33

III THEORETICAL DEVELOPMENTS **35**

4 Linear mixture random fields **37**
4.1 Introduction . . . 37
4.2 Linear mixed Gaussian$-t$ distribution . . . 37
4.2.1 Univariate distribution . . . 37
4.2.2 Mixed Gaussian$-t$ multivariate distribution . . . 38
4.3 Mixed Gaussian$-t$ random field, GT_β^ν . . . 38
4.3.1 Definition . . . 38
4.3.2 Representation of derivatives . . . 39
4.4 The EC densities of the GT_β^ν excursion sets . . . 40
4.5 The extreme values of the Gaussian$-t$ random field . . . 43
4.6 The expected intrinsic volumes of the GT_β^ν excursion sets over rectangles of $\mathbb{R}^2$ . . . 44
4.7 Simulation Results . . . 44
4.8 Conclusion . . . 46

5 Skew$-t$ random fields **49**
5.1 Introduction . . . 49
5.2 Representation of skew$-t$ distribution . . . 49
5.2.1 Univariate skew$-t$ distribution . . . 50
5.2.2 Multivariate skew$-t$ distribution . . . 50
5.3 Skew student's t random field . . . 51
5.3.1 Definition . . . 51
5.3.2 Representation of derivatives . . . 52
5.4 The EC densities of the skew$-t$ excursion sets . . . 54
5.5 The extreme values of the skew$-t$ random field . . . 57
5.6 Simulation results on two-dimensional rectangles . . . 58
5.7 Conclusion . . . 59

IV APPLICATION: CASE STUDY 61

6 Medical and scientific issue 63
6.1 Total hip replacement . . . 63
6.2 Choice of materials . . . 63
6.3 Wear of UHMWPE . . . 64
6.4 Motivations and objectives . . . 65

7 Experimental developments 67
7.1 Wear engineering simulation . . . 67
7.2 Surface roughness topographical measurements . . . 69
7.2.1 Instrumental measurements . . . 69
7.2.2 Removing gross geometry and form errors . . . 70
7.3 Conclusion . . . 72

8 Methodological developments 75
8.1 Introduction . . . 75
8.2 Modelling the topographic roughness of the UHMWPE surface before wear . . . 76
8.2.1 Parameter's estimation . . . 76
8.2.2 Validation . . . 78
8.3 Modelling the topographic roughness of the worn UHMWPE surfaces 80
8.3.1 Parameter's estimation . . . 81
8.3.2 Validation . . . 83
8.4 Statistical analysis of worn surfaces . . . 83
8.4.1 Estimation of the significant levels from uncertainty heights . 83
8.4.2 Comments . . . 85
8.4.3 Wear analysis induced by the statistical analysis of surface roughness . . . 85
8.5 Results and discussion . . . 89
8.5.1 Worn regions of the UHMWPE surface at the latitude 45° . . 89
8.5.2 Quantitative comparison between worn regions at 45° and 100° latitudes . . . 92
8.6 Conclusion . . . 92

V GENERAL CONCLUSION AND FUTURE WORK 95

9 Space−Time Skew−t Random Fields 97
9.1 Introduction . . . 97
9.2 Preliminaries . . . 98
9.3 Definition . . . 98
9.4 Expectations . . . 99
9.5 Simulation example . . . 100
9.6 Application . . . 101

9.7 Conclusion 105

10 Conclusion and future work **107**
10.1 General Conclusion 107
10.2 Future work 109

APPENDICES **111**

A Lemmas **113**

B Simulation of Gaussian random fields with isotropic/anisotropic correlation functions **115**
B.1 Orthogonal expansion (Karhunen-Loève expansion) 115
B.2 Spectral expansion using Fourier transform 116
B.3 Some isotropic covariance functions 117
B.4 Numerical simulation of anisotropic stationary GRFs 118

List of Abbreviations **123**

Notation Index **125**

Bibliography **127**

List of Figures

1.1 Probability density function of skewed random variables 10
1.2 Probability density function of different models 10
1.3 Example of three level sets 13
1.4 Simulation example of a Brownian sheet 14
1.5 Simulation example of a negatively skewed, isotropic, Gaussian surface 15

3.1 A simulation example of a two-dimensional Gaussian random field on a unit rectangle. 27
3.2 Example of a rectangle in $\mathbb{R}^3$ 32

4.1 An exemplary illustration of a two-dimensional GT^{ν}_{β} random field . . 45
4.2 Fitting the analytical and the simulated mean Minkowski functionals 45
4.3 Comparison between the expected Euler-Poincaré characteristic for GT^{ν}_{β} and Gaussian RFs 46

5.1 Three illustrations of the contour plot of the bivariate skew$-t$ pdf . . 51
5.2 First exemplary simulation 59
5.3 Second exemplary simulation 60

6.1 An illustration of the total hip implant 64

7.1 General view of the one-station hip wear simulator 68
7.2 Diagram of the artificial hip components 68
7.3 A synthetic $3D-$dimensional simulation of the convex UHMWPE acetabular cup 70
7.4 Surface topography of four selected samples of the worn UHMWPE surfaces 71
7.5 Gross geometry of the four selected samples 73
7.6 Roughness restored from the topography of the four selected samples 74

8.1 The autocorrelation function of a real 3D rough surface 77
8.2 Log-Plot of the number of the real local maxima 78
8.3 A real sample of 3D rough surface before the wear of UHMWPE . . 79
8.4 A contact deformation model 80
8.5 A real sample of the worn UHMWPE surface 81
8.6 Normal Q-Q plot of the surface roughness heights versus the normal distribution 82
8.7 The autocorrelation function of the worn rough surface 82
8.8 Fitting the empirical and the expected LKCs 83
8.9 Extreme values (maxima and minima) at wear process time 13×10^6 cycles 84

8.10 Surface roughness component after removing uncertain heights, and the Q-Q plot of its heights 86
8.11 Fitting the analytical and empirical LKCs for the real heights after thresholding 87
8.12 Hills and valleys at wear process time 13×10^6 cycles 87
8.13 Detection of significant upcrossing levels of a sample measured from the UHMPWE at latitude 45° along 19×10^6 cycles of wear time . . 88
8.14 Evolution of the difference between the bearing area and the void area at their significant levels over wear time 89
8.15 The height maps of one sample of the worn UHMWPE surface at wear times $0 - 3 \times 10^6$ cycles 90
8.16 3-D height map of one sample of the worn UHMWPE surface at wear times $4 \times 10^6 - 10 \times 10^6$ cycles 90
8.17 Significant levels over wear time for (5) UHMWPE samples at 45° latitude 91
8.18 The evolution of the difference between the bearing and the void volumes at the detected levels 91
8.19 A quantitative comparison between the hills/valleys levels of samples located at 45° and 100° latitudes 93

9.1 A space−time separable covariance function model 100
9.2 A synthesized spatio-temporal skew−t random field 101
9.3 Spatio-temporal skew−t random field over time 102
9.4 Euler-Poincaré characteristic of spatio-temporal excursion sets 103
9.5 The empirical spatio-temporal Euler-Poincaré characteristic 104
9.6 Estimation of the skewness index variability from real measurements 104
9.7 Prediction of the skewness evolution with time 105
9.8 Illustration of the variance of the error term of the predicted skewness index 106

B.1 Different isotropic continuous and positive definite covariance functions 119
B.2 Numerical simulation of stationary isotropic Gaussian random fields 120
B.3 Examples of a two-dimensional anisotropic exponentially damped cosine covariance function 121
B.4 Numerical simulation of two-dimensional stationary anisotropic GRFs 121

List of Tables

7.1 Wear test conditions of MTS-858 testing machine: 69

8.1 roughness parameters 76
8.2 Roughness parameters of one worn sample topography 85

Introduction

Preface

The present thesis has been established with the mathematical imaging and pattern analysis group in the LGF laboratory (Laboratoire Georges Friedel, UMR CNRS 5307) at Ecole Nationale Supérieure des Mines de Saint-Etienne (ENSM-SE), in collaboration with the center COT (Centre Chirurgie Orthopédique et Traumatologie) of the Hôpital Nord de Saint-Etienne. The experimental tests have all been realised in the ENSM-SE laboratories.

Medical Issue

Total hip arthroplasty is a reconstructive procedure which has improved the management of those diseases of the hip joint, that have responded poorly to conventional medical therapy, such as osteoarthritis. One of the most used total hip implants involves insertion of a femoral prosthesis, composed of a stem and small-diameter head, inside the femur, and an acetabular component, composed of ultra-high-molecular-weight polyethylene articulating surface, is inserted into the acetabulum cartilage. The hip prosthesis should insure high stability in the bone using either cemented or uncemented designs. Nowadays, the hip arthroplasty is one of the most widely performed surgeries in France (120000 hip prosthesis per year), and in Europe (about 800000), due to its increased role in reducing the pain, and in restoring the hip joint functions after sever degradation, and bony outgrowths related with different reasons, such as accidents, bone diseases, and ageing. Nevertheless, serious complications after hip replacement surgery might occur due to reasons caused by the wear of the prosthetic components.

Scientific Issue

The success of the total joint arthroplasty, during the last 30 years, is largely due to the use of the ultra-high-molecular-weight polyethylene (UHMWPE) as a bearing surface, which has a good resistance to wear. However, wear does occur in UHMWPE and sometimes can be excessive in younger and more active patients. The factors that affect the wear might include without limitation, design, material, surgical and patient factors. One of the most intrinsic wear factors are those related with the surface properties of the used materials, especially the surface roughness.

Generating the wear on the surface topography, of the UHMWPE component, has been achieved *in-vitro* using a joint simulator machine, in order to emulate the *in-vivo* joint implant (i.e.; the joint implant inside the patients). The worn surfaces

have been measured and observed using the three-dimensional white light interferometer. This technique enables three-dimensional topographical measurements within a limited field of view, in a fast and contacltless way. The topography of the observed surface can span many length scales, ranging from the physical form, to the very small-scale structures (microstructural features) defined by the local hills (summits) and valleys (or pits), and referred as roughness. The evolution of the surface roughness during this simulation process contributes understanding the *in-vivo* wear mechanisms, and the functional behaviour of the worn surface, to finally improve the prosthesis quality and its life-duration.

Aims and Scopes

The evolution of the surface roughness, and more precisely the hills (summits) [1] and valleys at certain height levels, is one of the basic factors that governs a number of important phenomena during mechanical contact between surfaces, such as the wear of materials. Due to the random nature of the topography of rough surfaces, these hills and valleys can be robustly estimated and determined by the random field theory. An appropriate random field model should be defined by significant statistical parameters that describe the roughness evolution of the worn surface, such as the second, third and fourth order moments, referred to as variance, skewness and kurtosis, respectively.

Studying the geometry generated by random fields has been well established via the integral geometry of their excursion sets, more precisely the intrinsic volumes including the Euler-Poincaré characteristic of those sets. An excursion set of a random field is defined by the set of points where their random variables exceed some threshold. The geometric properties of these excursion sets have numerous intrinsic benefits. For example, without limitation, they quantify the content of the excursion sets, such as the volume, area, length of boundaries. Furthermore, the Euler-Poincaré characteristic of the excursion set detected at high levels is a good estimate of the number of connected components (number of hills/or valleys). These intrinsic volumes have been expected for Gaussian random fields [Adl81, AH76] and extended to χ^2, t, F, and Hotelling's T^2 random fields by [Wor94, CW99]. Although the interesting results are obtained from these random fields in many applications, they are limited to give robust representation of the worn topography. Thus, the aim of this thesis, firstly concerns on extending the theoretical results to two types of random fields (one is defined by the linear mixture of Gaussian and t random fields, and the second is the skew$-t$ random field). Then, these random fields have been applied to real surfaces observed from a UHMWPE component, in order to represent, and to analyze the roughness topography of those surfaces, in

1. hills, summits and peaks are all synonyms to the local maxima of the surface. A hill might be considered more general, since it could also refer to local maxima which are not extremely high including significant amount of topographic prominence. So, it will be used inside the content of this thesis to refer to the local maxima.

both machined and worn states, respectively.

A Guide to this thesis

The thesis is organized into five parts as follows.
The first part (Part I) consists of chapter 1, which introduces a brief background of the surface roughness metrology. This chapter is also focused on the methods, reported in the literature, that have been used to characterize and to represent the surface roughness such as geometrical, and model-based methods. Advantages and limitations have been discussed to finally demonstrate the importance of the random field theory in combination with the geometry of their excursion sets, for topographical representation and analysis of rough surfaces.

The second part (Part II) reviews the basic framework of random fields (chapter 2) and the integral geometry of their excursion sets (chapter 3). The first chapter includes the mathematical definition and the basic properties of the random fields, giving some interesting examples. The second chapter explores the excursion sets and their geometric properties derived by the integral geometry such as Crofton's and Hadwiger's formulas, and the differential topology (Morse theory).

The third part (Part III) extends the theoretical results about the geometry of the excursion sets of some known random fields to the mixture model field defined by the linear combination of Gaussian and t random fields (chapter 4) and skew$-t$ random field (chapter 5). In chapter 4, the mean intrinsic volumes (Lipschitz-Killing curvatures (LKCs)), also known by Minksowski functionals with some normalization and order's change, have been expected for the two-dimensional Gaussian$-t$ random field. Furthermore, the behaviour of the expected Euler-Poincaré characteristic at high threshold for this mixture model is also discussed. Chapter 5, derives the expected formulae of the Lipschitz-Killing curvatures for the $N-$dimensional skew$-t$ random field. Furthermore, the mean number of the local maxima and minima of the skew t random field at high threshold is also derived analytically. The expected Euler-Poincaré characteristic is then expressed in the special case for $N = 2$. Simulation results in both chapters are established to compare the analytical results with the simulated ones.

The fourth part (Part IV) is concerned on applying these theoretical developments in the application defined by the total hip implant. Chapter 6 explores the basic concepts about the artificial hip prosthesis, design, and the choice of materials. Furthermore, the main problems related with some of these materials that motivated studying the surface roughness topography have been discussed.
The wear on the materials of the artificial hip prosthesis components have been generated in an experimental environment introduced in chapter 7. This chapter

also presents the technical methods used to measure and export the topographic map of surface roughness.
Chapter 8 provides the developments investigated on the real surfaces measured from the UHMWPE component during wear simulation process. A statistical analysis approach has been proposed based on the expected Euler-Poincaré characteristic of the skew$-t$ random field in order to estimate the hills and the valleys of the worn surface, and hence to estimate the roughness evolution during wear time.

The last part (Part V) is structured into two chapters, chapter 9 introduces a work in progress about the spatio-temporal skew$-t$ random field and the LKCs of its excursion sets, one of the interesting and original topics towards modelling the surface topography during wear time, analysing the spatio-temporal roughness variability for predicting the future behaviour of the worn surface. Then, chapter 10 draws a global conclusion that summarizes the thesis and provides suggestions and ideas that can be realized in the future research areas for further ameliorations, or even in other applications.

Part I

SURFACE CHARACTERIZATION

Chapter 1

Characterization and modelling of surface roughness topography

Contents

1.1 Introduction 7
1.2 Surface metrology 8
1.2.1 Two-dimensional approaches 8
1.2.2 Three-dimensional approaches 8
1.3 Geometry of level sets for surface characterization and analysis 12
1.4 Surface roughness representation 13
1.4.1 Wavelet models 13
1.4.2 Fractal models 13
1.4.3 Numerical models 14
1.4.4 Random field models 15
1.5 Conclusion 16

1.1 Introduction

The spatial and geometrical evolution of the topographic roughness of engineering surfaces avail understanding many important physical phenomena, such as friction, lubrication (liquid flow behaviour), and wear mechanism during mechanical contact between adjoined surfaces. Surface topography observed in microscopic scales are in fact extremely rough and of random nature. They are composed of alternating hills and valleys of various dimensions referred to as surface heights, *or asperities and valleys*. On the other hand, the height maps observed by the optical instruments can be digitized and stored as 2D images, and so they can be characterized using numerous image processing methods, such as filtration techniques [Bla06, JBS01b], spectral analysis [Wu00], texture analysis [SP08, SP01], and feature extraction techniques [Sco09, Sco04, JZS+08]. However, understanding the mechanical contact between adjoined surfaces requires definition of the geometry of the adjoined hills, quantifying their number and their size, and estimating their height levels [Adl81]. Furthermore, the surface lubrication properties can be described by quantifying the size and the number of the valleys and pits. Such

problems can not be resolved without a mathematical model that describes the microgeometry of these hills and valleys and predicts their real heights. The next section will review the traditional and technical methods in the surface metrology framework for the surface roughness characterization. A special interest in this chapter will be given to the model-based methods and the geometry of the level sets, precisely the intrinsic volumes, developed in the literature to answer the previous problems.

1.2 Surface metrology

In surface metrology science, a set of roughness parameters, and characterizing functions were defined to describe rough surfaces. They were categorized between 2-D and 3-D roughness parameters accordingly with the approaches being used to describe the surface.

1.2.1 Two-dimensional approaches

The early characterization methods of surface roughness were established on the two-dimensional surface profiles [JSWB07a, DS95, Whi94]. Statistical parameters such as the amplitude and the spacing parameters are used to describe the roughness and the joint distribution of the surface profiles. One of the widely used parameters to describe the roughness are the amplitude parameters. They quantify either the profile heights relatively to a reference line, such as the absolute mean height, R_a, and the root mean square deviation, R_q, or the shape of the height's distribution by measuring its symmetry and peakedness, such as the skewness, R_{sk}, and the kurtosis, R_{ku}, respectively. Besides the amplitude parameters, other techniques aim at measuring the spacing parameters between the profile heights. These spacing parameters are computed from the autocorrelation function (ACF) of the profile. Another numerous parameters are defined in the standards [ISO97, Cor04].
The problem associated with the two-dimensional methods is that they are not descriptive. For example, one can find the same values of the amplitude parameters for two different surface profiles [NBMI06, Cos00]. Furthermore, the surface profiles do not contain any textural information of the surface topography such as isotropy/anisotropy, periodicity, hills/valleys shape or size [DS95].

1.2.2 Three-dimensional approaches

Following the development of the 3D measurement techniques, in the last years, the three-dimensional approaches have been arisen for characterizing the two-dimensional surface topography. All the roughness parameters derived by the two-dimensional approaches have been extended by the three-dimensional methods and computed from the surface topography. Additionally, other parameters are defined to quantify the surface texture properties, surface bearing area, material

and void volumes. These parameters are designated under the name "S parameters" to be distinguished from the "R parameters" given by the two-dimensional methods [DSS94, SSD+93].

1.2.2.1 Statistical methods based on height's distribution

These methods describe some amplitude-related parameters based on the height's distribution, as seen in the two-dimensional case. The amplitude parameters are used to describe the dispersion of the surface heights from a reference plane such as the mean arithmetic deviation, S_a, and the root mean square arithmetic deviation (RMS), S_q, given by their following digital formula for a surface Z defined on a rectilinear lattice in $\mathbb{R}^2$, with $(M \times N)$ points, [SSD+93]:

$$\begin{aligned} S_a &= \frac{1}{MN} \sum_{i=1}^{M} \sum_{j=1}^{N} |Z(x_i, y_j)| \\ S_q &= \sqrt{\frac{1}{MN} \sum_{i=1}^{M} \sum_{j=1}^{N} Z^2(x_i, y_j)} \end{aligned} \tag{1.1}$$

where x_i is the ith $x-$coordinate, and y_j is the jth $y-$coordinate of the discrete lattice in $\mathbb{R}^2$. These parameters are, in both one-dimensional and two-dimensional cases, sensitive to the length (size) of the sampling interval (area), respectively [SSD+93]. A surface being digitized on the same measurement domain with two different sampling intervals will have different values of S_a and S_q.
The shape of the joint distribution function of the surface heights is described by two significant parameters, namely skewness S_{sk} and kurtosis S_{ku} equivalently to the one dimensional case. The skew parameter measures the symmetry of the height's distribution (Fig. 1.1). Its discrete form is defined as [SSD+93]:

$$S_{sk} = \frac{1}{MNS_q^3} \sum_{i=1}^{M} \sum_{j=1}^{N} Z^3(x_i, y_j) \tag{1.2}$$

and the kurtosis parameter measures the peakedness (or flatness) of the height's distribution (Fig. 1.2), and it is given by [SSD+93]:

$$S_{ku} = \frac{1}{MNS_q^4} \sum_{i=1}^{M} \sum_{j=1}^{N} Z^4(x_i, y_j) \tag{1.3}$$

Note that the amplitude parameters of the surface topography do not have any descriptive information about the surface texture.

1.2.2.2 Autocorrelation function and spectral methods

In order to describe the spatial relation between two height values, the traditional areal autocorrelation function (AACF) and the areal power spectral density

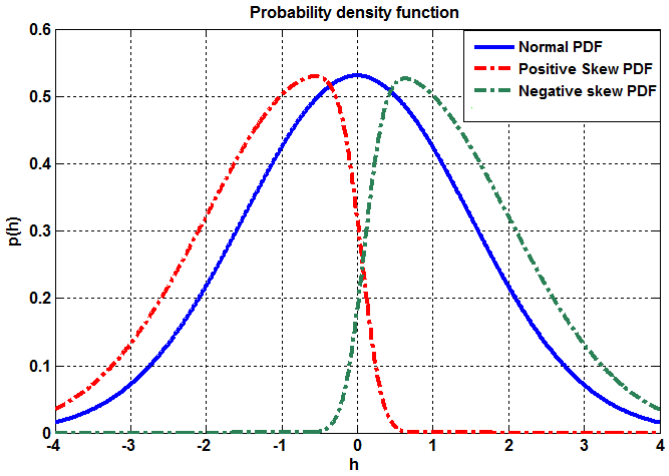

Figure 1.1: Probability density function of skew random heights with different values of skewness and different symmetry behaviors.

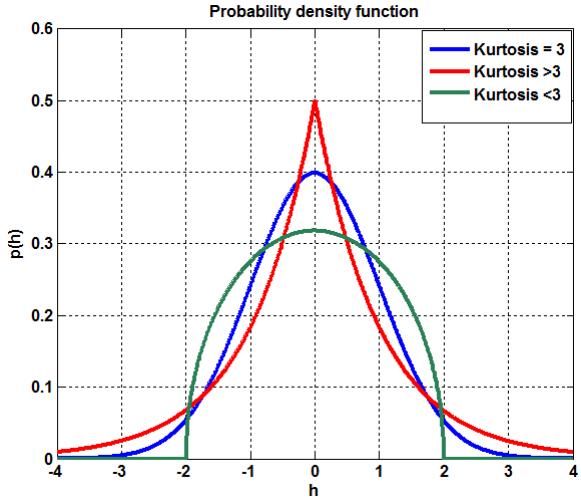

Figure 1.2: Probability density function of different symmetric, and unit variance random models with different kurtosis values, (Gaussian; kurtosis = 3), (Laplace; kurtosis >3), and (Wigner semicircle; kurtosis <3).

(APSD) of the surface have been used. Spacing parameters can be quantified from the AACF and the APSD that measure the isotropy/anisotropy of the surface, the texture direction and the distances between correlated heights [Bra00]. These spacing parameters are the fastest decay correlation length S_{al} which measures the texture length-scale, and the texture aspect ratio $0 < S_{tr} \leq 1$, that measures the degree of anisotropy of a surface [Bra00]. For example, isotropic surfaces have similar correlation length decay along all directions and the S_{tr} value is near 1. The direction of the texture, denoted S_{td}, can be obtained directly for stationary surfaces from the areal power spectral density function APSD using the two-dimensional Fourier transform [Bra00]. It is defined by the angle where the maximum value of the APSD occurs [SSD+93]. Additionally, the density of surface summits, denoted S_{ds}, is defined as a spatial parameter and derived from the AACF. It is given by the number of the surface hills and valleys in the unit sampling area [SSD+93]. Unfortunately, for a surface topography, they are defined by many ways . In [JP68], a hill or valley is defined as the highest or deepest point lying within a four or eight nearest neighbours, and in [Wal69], it is defined by a contour-based summit detection method. So, the number of the surface summits will vary according to the way the hills and valleys are defined [1].
Some of the spacing parameters, likely the amplitude parameters, are sensitive to the sampling interval (spatial resolution), and they should be given and compared based on that later [SSD+93].

Surface parameters are not limited to the previous discussed ones. Further parameters are reported in [SSD+93, Bla06, DS95, Whi94] and in the different versions of the standard ISO [ISO05, ISO06], like the hybrid parameters which are based on both the amplitude and spacing parameters, and the functional parameters that describe the surface bearing area, material volume and void volume [SSD+93, JSWB07b]. The functional parameters, as they called, describe the functional properties of the surface such as bearing, wear running-in and fluid retention [SSD+93]. These parameters can be estimated using Abbott-Firestone curve [AF33].

1.2.2.3 Abbott-Firestone curve

Abbott-Firestone curve [AF33], equivalently called by marginal ratio curve or bearing area curve, was the early characterizing function for the surface roughness. Firstly, it was computed from the surface profile, then, it was extended for the two-dimensional surface heights [SSD+93]. Abbott-Firestone curve is one of the important tools in surface characterization. The surface functional parameters such as core roughness depth S_k, reduced peak height S_{pk}, reduced valley depth S_{vk} bearing area parameters SM_{r_1}, SM_{r_2} have been defined from Abbott-Firestone curve [SSD+93]. Abbott-Firestone curve measures the density of the surface hills

1. This is one of main reasons why a mathematical modelling arises and becomes the more robust way to define the surface hills and valleys rather than experimental methods

(valleys) above (below) a height value. It has been used for studying the stress, in some contact deformation problems, and to predict the bearing behaviour and the fluid retention properties of the surface.

In summary, there is 14 parameters for characterizing the surface topography and they are classified between amplitude, spacing, hybrid and functional parameters. Their significance depends on the surface property and the application needs.

1.3 Geometry of level sets for surface characterization and analysis

A level set, can be simply defined here, as the result of hitting the surface by a plane at certain height level, and keeping all the points above this level. Thus, the level set can be seen as a result of threshold process of the surface heights in $\mathbb{R}^2$. The geometric properties of a given level set are quantified by some measures, which define the size and the boundaries of its content, and its connectivity, known as Minkowski measures (more details can be seen in chapter 3).

Those characterizing measures have a very interesting physical interpretations [Sch06], and they are correlated with most of the surface roughness parameters defined in surface meteorology, as will be seen in the next chapters of this thesis. The area of the level sets, calculated at different height thresholds, gives the material area ratio or equivalently the related Abbott-Firestone curve [AF33]. Complementary, computing the area of the level sets below those thresholds (where the plane does not hit the part of material that is out of contact with it) defines the void area (the area of valleys and cavities or holes) which is also could be associated with the Abbott-Firestone curve discussed in subsection 1.2.2.3.

The contour length of the level sets enables measuring some spatial features of those sets [Sch06], and it describes how much the level is smooth. For rough surfaces, a level set might include much small-scale structures, and structures of irregular boundaries. In this case, the contour length will be much higher than the one estimated from level sets of smooth surfaces. Besides the material/void area ratio, and the contour length, one can estimate the number of holes, cavities, and peaks, which could be counted by the so-called Euler-Poincaré characteristic (see chapter 3). The Euler-Poincaré characteristic has an important interpretation of the surface percolation context [Mec00, Mec98]. A negative value of the Euler-Poincaré characteristic indicates that the material is governed by holes, where the fluid will be trapped inside. Thus, the number and the size of those holes could be the most significant features in the level set, in this case. Likewise; a positive value implies that the level set mainly consists of isolated blobs (or regions) of the material, so the fluid in such case can flow freely on the surface (see Fig. 1.3).

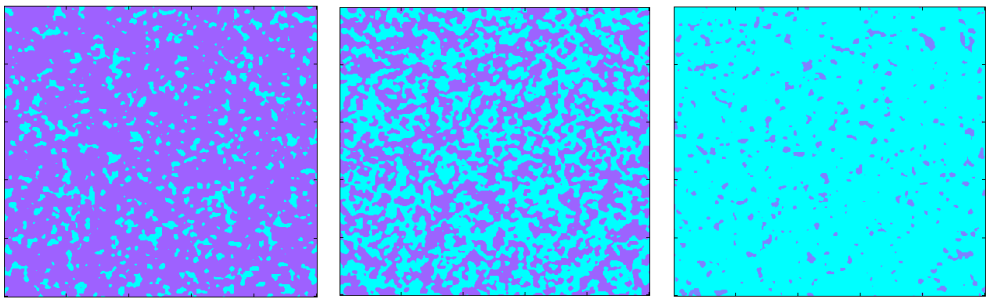

(a) (b) (c)

Figure 1.3: Example of three level sets composed of objects (materials and voids) with different Euler-Poincaré characteristics (χ). (a) $\chi = 388$. (b). $\chi = 39$ (c) $\chi = -462$. The materials and voids are represented as by: ■ materials and ■ voids.

1.4 Model-based methods for surface roughness representation and analysis

Model-based methods state that the measured roughness component of the surface topography is perceived according to an appropriate model, which is identified by some parameters that represent the most important textural information of the surface topography, and also have a direct physical interpretation. These methods are used for analysis, and for simulation of rough surfaces.

1.4.1 Wavelet models

A multi-scale representation of rough surface is suggested by wavelet models [WM97, LXLZ05, JBL02, LZCM98, JBS01a, JSW08]. A sequence of spatial filters of different kernel models are defined over a range of scales to represent the multi-scale surfaces. The appropriate wavelet model depends on the surface structure and the manufacturing process. The range of the significant scales can be determined by the wavelet decomposition of the surface and hence from the wavelet coefficients that significantly describes the surface. In wear analysis applications, the multi-scale descriptors are statistically dependent over some scales, and the dependence between the wavelet coefficients is often unknown. Furthermore, the descriptors that might be significant in one scale at one wear time might not have any significance at another scale and time.

1.4.2 Fractal models

The topography of rough surfaces have been characterized and represented by the geometry of fractal [ZVL98, ST78, Rus94, TRA99, PS00, Whi02, PS99, Cos00, PG07, WPS10, PS05], which states that the geometric features (lines, curves, area and etc.) of rough surfaces exhibit the self-similarity property, i.e. they have the same magnifications at all scales and in all directions (scale-invariant or isotropic

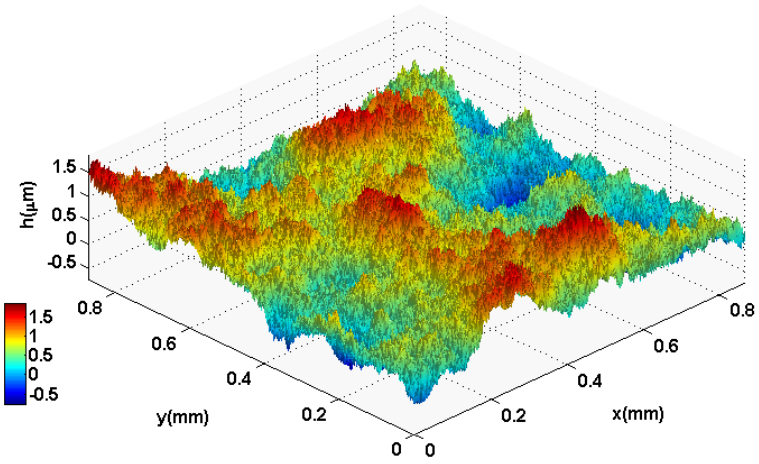

Figure 1.4: Simulation example of a Brownian sheet on $[0,1]^2$

fractal), or they exhibit the self-affinity property which states that some rough surfaces are composed of structures of unequal scaling magnifications in different directions and thus define anisotropic fractal surfaces [ZVL98, Cos00]. In both cases, there is two intrinsic parameters being used to describe the geometry of the isotropic/anisotropic fractal surfaces, namely fractal dimensions D and the exponent of roughness H [ZVL98]. One of the basic assumptions in the geometry of fractal is that the surface does not follow the regular law of Euclidean geometry. The surface can be described and represented with a non-integer parameter $D \in [1,2]$ for two-dimensional profiles, and $D \in [2,3]$ for the three-dimensional profiles (or surfaces). Numerous methods have been proposed to represent the topography of rough surfaces, mainly one is the Fractional Brownian motion [MN68] (see a simulation example in Fig. 1.4, which states that a surface of a fractional Brownian motion will satisfy that the greatest differences between any two points located at a distance d in the parameter space will follow an exponent law d^H with $H = 1/2$. Nevertheless, many engineered surfaces have not the self-similarity property, and the surface microstructures geometry, such as the contour, area or volume of hills and valleys, are not scale-invariant, except over a range of scales. One can see the arguments in [JSWB07b, Whi02] on the log-log plot of the volume-scale or area-scale. Furthermore, Fractal dimension lacks straightforward physical meanings and has not been directly linked with the functional behaviour of engineering surfaces [SSD+93].

1.4.3 Numerical models

Numerical models by image processing techniques [MRS10, AWC02, Wu00, HT92] are commonly used to represent the topography of rough surfaces, which enable analyzing the mechanical contact properties from the represented roughness maps. A rough surface with identified statistical amplitude parameters S_a, S_q,

S_{sk}, S_{ku} and autocorrelation function can be represented and simulated numerically using the Johnson translator method [Joh49]. These models do not require any assumption of surface isotropy/anisotropy, hills/valleys shape, or the distribution type of the surface heights. In fact, the geometry of the hills and valleys, and the surface texture properties have significant physical interpretation on engineered surfaces.

1.4.4 Random field models

Random field models are well established to model the microgeometry of the hills and valleys of a surface, in many applications related to mechanical contact of rough surfaces, using either the Gaussian or non-Gaussian random fields [Nay73, GW66, Rei11, AF81, Sch06, AA09]. Gaussian surfaces have been referred to as the dependent random heights having a joint Gaussian distribution function which is uniquely characterized by its autocorrelation function. The model of the covariance function, or the autocorrelation function, defines the spatial features of the Gaussian hills and valleys and the texture properties of the surface (see Appendix B for examples). In some applications associated with wear processes, some statistical parameters derived from the third and fourth order moments, S_{sk} and S_{ku}, of the height's joint distribution become significant characteristics. Thus, the Gaussian model can not approximate such worn surfaces. One of the interesting examples proposed in the literature [AA09] for modelling worn surfaces is the skew-Gaussian random field. The skew-Gaussian random field generalises the Gaussian one by including the skewness concept to the normal distribution function (see Fig.1.5 as example), so that the marginal probability density function, $p(h)$, at each height h on the surface can be defined as:

$$p(h) = 2\phi(h)\Phi(\delta h/\sqrt{1-\delta^2}), \quad (h \in \mathbb{R}) \tag{1.4}$$

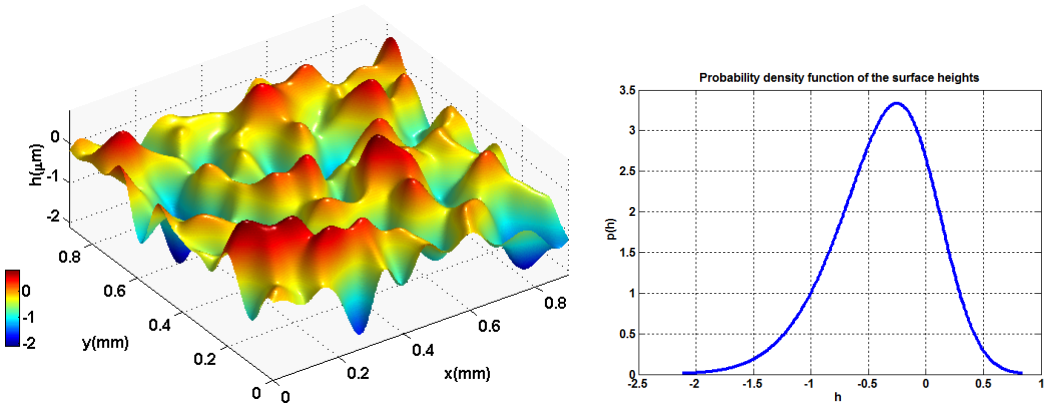

(a) (b)

Figure 1.5: (a) Simulation example of a negatively skewed, isotropic, Gaussian random surface on $[0.1]^2$. (b) The probability density function of the surface heights with skewness index $\delta = -0.5$.

where $\phi(.), \Phi(.)$, are the Gaussian density and the Gaussian cumulative distribution functions, respectively, and $\delta \in (-1, 1)$ is a parameter that indicates the skewness of the distribution function such that:

$$S_{sk} = \frac{4-\pi}{2} \frac{(\delta\sqrt{2/\pi})^3}{(1-2\delta^2/\pi)^{3/2}} \tag{1.5}$$

Nevertheless, the influence of the kurtosis is negligible in the skew-Gaussian random fields, which requires looking beyond the Gaussian surfaces and use the non-Gaussian random fields such as the ones introduced and defined, in this thesis, in chapters 4 and 5.
Similarly to fractal surfaces [2], the random field, being defined as a model of a rough surface, and the geometric properties of its excursions above some levels are related with the mechanical contact model. For example, in plastic contact problems between a rough surface and a hard, smooth, and flat one [GW66, Nay73], it was shown that the joint distribution function model of the finite contact hills, and their mean area could describe and determine the normal pressure/hardness ratio.

1.5 Conclusion

Following the arguments discussed about the model-based methods for characterizing the surface roughness topography, the random field models arise to be one of the powerful approaches in this application field, more precisely, the combination of random fields and the geometry of the level sets. The models seen in this bibliographic chapter can all be considered as stochastic models that deal with random and rough surfaces, and the research developments are not limited to only these approaches, but also to combinations between them. A combination between fractal and wavelet approaches enabled define a multi-scale fractal surfaces [PS02, PS03], whereas a combination between wavelet and random fields enables define a scale-space random fields [ATW11, SJLG03]. In all cases, choosing one approach over another strongly depends on the area of application to be addressed.

The next chapters in this thesis will focus on the basic theoretical topics of the random fields and their geometry, in order to export the main results required for the application.

2. Fractal surface is also a random process. We distinguish between fractal models and random fields since we need to study the geometry of the excursion sets and to estimate the number of hill and valleys. The first ones are non-differentiable erratic models, so that the number of hills/valleys inside an excursion set will tend to infinite [Adl81]

Part II

RANDOM FIELDS THEORY AND THEIR GEOMETRY

Chapter 2

Random Fields Theory

Contents

2.1 Random fields 19
2.1.1 Definition 19
2.2 Stationarity, Isotropy, and Anisotropy 20
2.2.1 Stationarity 20
2.2.2 Isotropy 21
2.2.3 Anisotropy 21
2.2.4 Spectral representation on $\mathbb{R}^N$ 21
2.3 Gaussian random fields 22
2.3.1 Definition 22
2.3.2 Spectral moments of Gaussian random fields 23
2.4 Non-Gaussian random fields 24
2.5 Conclusion 25

2.1 Random fields

This chapter reviews some basics of the random fields given in the literature, [AT03, Abr97, Yag87a, Yag87b, Van83, Adl81]. We are interested in stationary Gaussian and non-Gaussian random fields which are basically related to the Gaussian one and defined on the $N-$dimensional Euclidean space.

2.1.1 Definition

Let $(\Omega, \mathcal{F}, \mathcal{P})$ be a probability space, and a topological space $S \subset \mathbb{R}^N$. Then, an $N-$dimensional random field is defined as a measurable mapping $Y : \Omega \to (\mathbb{R}^S)^d$, $d \geq 1$, and denoted by $Y(\boldsymbol{x}, \omega)$, $\boldsymbol{x} \in S$, $\omega \in \Omega$. When $d = 1$, then f is called a real-valued $N-$dimensional random field, and if $d > 1$, the measurable mappings from Ω to $(\mathbb{R}^S)^d$ are called $\mathbb{R}^d-$valued $N-$dimensional random fields.
The notation is usually restrained in the literature so:

$$Y_{\boldsymbol{x}} \equiv Y(\boldsymbol{x}) \equiv Y(\boldsymbol{x}, \omega)$$

In general, a random field $Y(\boldsymbol{x})$, $\boldsymbol{x} \in S$ is uniquely determined by its finite-dimensional $(fi - di)$ distributions. Given an arbitrary collection of random variables $Y(\boldsymbol{x}_1), ..., Y(\boldsymbol{x}_n)$ for any $\boldsymbol{x}_1, ..., \boldsymbol{x}_n \in S$ and any $n \geq 1$, then, the $(fi - di)$

distributions of such collection is defined by:

$$F_{\boldsymbol{x}_1,...,\boldsymbol{x}_n}(y_1,...,y_n) = P\left\{Y(\boldsymbol{x}_1) \leq y_1,...,Y(\boldsymbol{x}_n) \leq y_n\right\} \tag{2.1}$$

Thus, a random field $Y(\boldsymbol{x})$, $\boldsymbol{x} \in S$ can also be defined as a collection of random variables, together with a collection of their $(fi-di)$ distributions, or joint distribution functions, of the form $F_{\boldsymbol{x}_1,...,\boldsymbol{x}_n}$.

2.2 Stationarity, Isotropy, and Anisotropy

To understand the structure of the random fields, some important properties such as the stationarity, isotropy and anisotropy should be introduced. On the other hand, when dealing with stationary random fields a general and simple way to generate these random fields arises using the spectral representation, and hence, the spectral moments of random fields become the interesting result of the spectral representation theory.

2.2.1 Stationarity

Let consider S the parameter space in $\mathbb{R}^N$, such that $\boldsymbol{x}$, $\boldsymbol{s} \in S$ implies that $\boldsymbol{x}+\boldsymbol{s} \in S$.

Definition 2.2.1 (Stationarity in strict sense)**.** *A random field $Y(x)$, $x \in S$ is said stationary* in strict sense *over S, if all its $fi-di$ distributions are invariant under arbitrary translations. That is, for any $n \geq 1$ and any set of points $\boldsymbol{s}, \boldsymbol{x}_1, ..., \boldsymbol{x}_n \in S$*

$$F_{\boldsymbol{x}_1+\boldsymbol{s},...,\boldsymbol{x}_n+\boldsymbol{s}}(y_1,...,y_n) = F_{\boldsymbol{x}_1,...,\boldsymbol{x}_n}(y_1,...,y_n) \tag{2.2}$$

An immediate definition follows the strict stationarity is the weak stationarity or stationarity in wide sense. Let $\mathbb{E}[Y(\boldsymbol{x})] = \mu(\boldsymbol{x})$ and $C(\boldsymbol{x},\boldsymbol{s}) = Cov(Y(\boldsymbol{x}), Y(\boldsymbol{s}))$ be the mean and covariance functions of a random field $Y(\boldsymbol{x})$, respectively, such that $\mathbb{E}[\|Y(\boldsymbol{x})\|^2] < \infty$ for all $\boldsymbol{x} \in S$.

Definition 2.2.2 (Stationarity in wide sense)**.** *A random field $Y(\boldsymbol{x})$, $\boldsymbol{x} \in S$ is said stationary* in wide sense*, or "weakly" stationary over S if*

$$\mu(\boldsymbol{x}) = \mu \quad \textit{and} \quad C(\boldsymbol{x},\boldsymbol{s}) = C(\boldsymbol{x}-\boldsymbol{s}) \tag{2.3}$$

This means that the mean function is constant and that the covariance function only depends on the difference vector $\boldsymbol{x}-\boldsymbol{s}$. The corresponding covariance function is called a stationary covariance function. Notice that, the strictly stationary implies the stationarity in wide sense, but the opposite is not always true, except for the Gaussian random fields, where strict stationarity and weak stationarity are both equivalent. Stationary random fields are also called homogeneous random fields, [Yag87a, Van83, Adl81].

2.2.2 Isotropy

A special class of stationary or homogeneous random fields on $\mathbb{R}^N$ are the isotropic random fields. These random fields are translation and rotation invariant. Let consider S is a metric space equipped by the Euclidean distance (or the Euclidean norm) such that:

$$dist(\boldsymbol{x}, \boldsymbol{s}) = \|\boldsymbol{x} - \boldsymbol{s}\| = \left(\sum_{i=1}^{N} (x_i - s_i)^2 \right)^{\frac{1}{2}} \tag{2.4}$$

Definition 2.2.3. *A stationary random field is said isotropic if the covariance function depends only on the Euclidean norm of the difference vector $\boldsymbol{x} - \boldsymbol{s}$ such that:*

$$C(\boldsymbol{x}, \boldsymbol{s}) = C(\|\boldsymbol{x} - \boldsymbol{s}\|) \tag{2.5}$$

A covariance or correlation function implies the last definition is called an isotropic function. As can be seen, the covariance function depends only on the distance between $\boldsymbol{x}$ and $\boldsymbol{s}$.

2.2.3 Anisotropy

The anisotropic covariance functions are defined by replacing the Euclidean norm of the metric space S by the general norm [1] of the form:

$$dist(\boldsymbol{x}, \boldsymbol{s}) = \|\boldsymbol{x} - \boldsymbol{s}\|_{\boldsymbol{D}} = \sqrt{(\boldsymbol{x} - \boldsymbol{s})^t \boldsymbol{D} (\boldsymbol{x} - \boldsymbol{s})} \tag{2.6}$$

where t stands for the transpose, and the $N \times N$ matrix $\boldsymbol{D}$ is non-negative definite (i.e. $\boldsymbol{x}^t \boldsymbol{D} \boldsymbol{x} \geq 0$ for all $x \in \mathbb{R}^N$).

Definition 2.2.4. *A stationary covariance, or correlation, function on $\mathbb{R}^N$ is said anisotropic function if it depends on the general non-Euclidean norm such that:*

$$C(\boldsymbol{x}, \boldsymbol{s}) = C(\|\boldsymbol{x} - \boldsymbol{s}\|_{\boldsymbol{D}}) \tag{2.7}$$

The covariance functions defined by the general norm are called ellipsoidal covariance functions. A stationary random field with anisotropic covariance function is said anisotropic random field *"in the wide sense"*.

2.2.4 Spectral representation on $\mathbb{R}^N$

The basic result that arises in the theory of stationary random fields is the spectral representation theorem [Boc33], which states that a continuous real function $C : \mathbb{R}^N \to \mathcal{C}$ is non-negative definite, and so called a covariance function, if and only if it can be represented in the form:

$$C(\boldsymbol{x}) = \int_{\mathbb{R}^N} e^{i<\boldsymbol{x}, \boldsymbol{\lambda}>} d^N F(\boldsymbol{\lambda}) \tag{2.8}$$

1. The general non-Euclidean norm is equivalent to the Mahalanobis norm

where $F(\boldsymbol{\lambda}) : \mathbb{R}^N \to [0, \sigma^2]$ is a $N-$dimensional distribution function, also called spectral distribution function of C, and $\sigma^2 = C(0) = \int_{\mathbb{R}^N} d^N F(\boldsymbol{\lambda})$.
If F is continuous, then the spectral density function is defined as:

$$f(\boldsymbol{\lambda}) = \frac{\partial^N F(\boldsymbol{\lambda})}{\partial\lambda_1 ... \partial\lambda_N} \tag{2.9}$$

Based on the spectral representation theorem, [Adl81] proved that a complex-valued [2] *"weakly"* stationary, or homogeneous, random field, $Y(\boldsymbol{x})$, can be represented such that:

$$Y(\boldsymbol{x}) = \int_{\mathbb{R}^N} e^{i<\boldsymbol{x},\boldsymbol{\lambda}>} d^N Z(\boldsymbol{\lambda}) \tag{2.10}$$

and it has the covariance function $C(\boldsymbol{x} - \boldsymbol{s}) = \mathbb{E}[Y(\boldsymbol{x})\overline{Y(\boldsymbol{s})}]$, which is represented as:

$$C(\boldsymbol{x}, \boldsymbol{s}) = \int_{\mathbb{R}^N} e^{i<(\boldsymbol{x}-\boldsymbol{s}),\boldsymbol{\lambda}>} d^N F(\boldsymbol{\lambda}) \tag{2.11}$$

where $Z(\boldsymbol{\lambda})$ is the $N-$dimensional complex spectral distribution function of the complex noise field Z. Note that if Z is a Gaussian noise, then Y is a Gaussian random field.
When Y is a real-valued random field, then the covariance function is a symmetric function about its origin and it can be written as:

$$C(\boldsymbol{x}, \boldsymbol{s}) = \int_{\mathbb{R}\times\mathbb{R}^{N-1}} cos(\langle(\boldsymbol{x} - \boldsymbol{s}), \boldsymbol{\lambda}\rangle) d^N F(\boldsymbol{\lambda}) \tag{2.12}$$

and the spectral representation of the real-valued random field Y is then:

$$\begin{aligned} Y(\boldsymbol{x}) = &\int_{\mathbb{R}\times\mathbb{R}^{N-1}} cos(\langle\boldsymbol{x}, \boldsymbol{\lambda}\rangle) d^N Z_1(\boldsymbol{\lambda}) \\ &+ \int_{\mathbb{R}\times\mathbb{R}^{N-1}} sin(\langle\boldsymbol{x}, \boldsymbol{\lambda}\rangle) d^N Z_2(\boldsymbol{\lambda}) \end{aligned} \tag{2.13}$$

where Z_1 and Z_2 are real-valued and independent spectral noises.

2.3 Gaussian random fields

2.3.1 Definition

This section introduces brief details about the Gaussian random fields as an important class of random fields, and they are the main blocks of this thesis. Gaussian random fields on $\mathbb{R}^N$ are defined by their $(fi - di)$ distributions, $F_{\boldsymbol{x}_1,...,\boldsymbol{x}_n}$, which form a multivariate normal distribution for any arbitrary choice of n and any collection $(\boldsymbol{x}_1, ..., \boldsymbol{x}_n)$.

2. A complex-valued random field, Y, is of the form $Y(\boldsymbol{x}) = Y_R(\boldsymbol{x}) + iY_I(\boldsymbol{x})$, where Y_R and Y_I are real-valued random fields on $\mathbb{R}^N$

Let $\boldsymbol{Y} = (Y_1, ..., Y_n)^t$ be a $\mathbb{R}^n-$valued random vector with Gaussian random variable components for any choice n. Then, the multivariate normal probability density function, or *the joint normal probability density function*, denoted p_Y, is defined as:

$$p_Y(\boldsymbol{y}) = \frac{1}{(2\pi)^{\frac{n}{2}}|\Sigma|^{\frac{1}{2}}} e^{-\frac{1}{2}(\boldsymbol{y}-\boldsymbol{\mu})^t \boldsymbol{\Sigma}^{-1}(\boldsymbol{y}-\boldsymbol{\mu})} \tag{2.14}$$

where $\boldsymbol{y}^t = (y_1, ..., y_n)$, $\boldsymbol{\mu} = \mathbb{E}(\boldsymbol{Y})$ is the n vector mean, and $\boldsymbol{\Sigma}$ is a $n \times n$ non-negative (or semi-positive) definite covariance matrix with elements $\boldsymbol{\Sigma}_{ij} = \mathbb{E}[(Y(\boldsymbol{x}_i) - \mu_i)(Y(\boldsymbol{x}_j) - \mu_j)]$, and determinant $|\boldsymbol{\Sigma}| = \det(\boldsymbol{\Sigma})$.

The Gaussian random fields are completely specified by their mean vector and covariance matrix, (see Appendix B for some simulation examples).

2.3.2 Spectral moments of Gaussian random fields

Given the spectral representation theorem, one of the very useful and important topics, that can be derived from the spectral density and the covariance function of the $\mathbb{R}$-valued Gaussian random field Y, is what's called the spectral moments, denoted by $\lambda_{i_1,...,i_N}$ [3]. They are defined [Adl81]as:

$$\lambda_{i_1,...,i_N} = \int_{\mathbb{R}^N} \lambda_1^{i_1} ... \lambda_N^{i_N} d^N F(\boldsymbol{\lambda}) \tag{2.15}$$

for all $i_1, ..., i_N$ with $i_k \geq 0$, and $\boldsymbol{\lambda} \in \mathbb{R}^N$.
Considering that the Gaussian random field is stationary, then its covariance function and its spectral distribution are symmetric, (i.e., $C(\boldsymbol{x}) = C(-\boldsymbol{x})$ and $F(\boldsymbol{\lambda}) = F(-\boldsymbol{\lambda})$), consequently, the odd-order spectral moments will be zero. A special interest about stationary Gaussian random fields concerns the second-order spectral moment, denoted λ_{ij} with $(i, j = 1, ..., N)$, which depends on the second-order derivatives of the covariance function $C(\boldsymbol{x})$ near its origin [4] and it can be written as:

$$\lambda_{ij} = \left.\frac{\partial^2 C(\boldsymbol{x}, \boldsymbol{s})}{\partial x_i \partial s_j}\right|_{\boldsymbol{x}=\boldsymbol{s}} = -C_{ij}(0) \tag{2.16}$$

for $i, j = 1, ..., N$. The $N \times N$ matrix of these second-order moments is denoted by Λ. On the other hand, the first-order derivatives of the $\mathbb{R}$-valued Gaussian random field Y are dependent, and they have the partial derivative $\partial^2 C(\boldsymbol{x})/\partial \boldsymbol{x}^t \boldsymbol{x}$ as covariance function [Adl81, AT03]. Thus, the matrix $\boldsymbol{\Lambda}$, is also defined as the variance$-$covariance matrix of the partial derivatives of Y, and it is written as:

$$\Lambda = \mathbb{E}\left(\frac{\partial Y(\boldsymbol{x})}{\partial \boldsymbol{x}} \frac{\partial Y(\boldsymbol{s})}{\partial \boldsymbol{s}}\right) \tag{2.17}$$

3. The third and fourth order spectral moments have specific names called, skewness and kurtosis, respectively.

4. Generally, for stationary Gaussian random fields the $2k$th-order spectral moments are derived from the $2k$th partial derivatives of the covariance function at the origin [Adl81].

Under the isotropy condition of random fields, the second-order spectral moment matrix $\Lambda = \lambda I_N$, where I_N is the $N \times N$ identity matrix, and λ is the second spectral moment [5], where λ is independent of the indices $i = 1, ..., N$ in this case.

2.4 Non-Gaussian random fields

Beyond the Gaussian random fields, some non-Gaussian random fields arise, widely, for modelling and analysing many natural phenomena. This section will focus on introducing a class of Non-Gaussian random fields which are mainly based on the Gaussian one, and also namely *Gaussian-related random fields*. One example of these random fields is called the t random field and it will be within the focus of this thesis.
Let consider $\boldsymbol{Z}$ be a centered $\mathbb{R}^k-$valued Gaussian random field defined on some parameter space S, such that $\boldsymbol{Z} : S \to \mathbb{R}^k$, and all its k components $Z_0, ..., Z_{k-1}$ are independent, and identically distributed (i.i.d.), with constant variance [6]. Then, a transformation function denoted F, where $F : \mathbb{R}^k \to \mathbb{R}$ can define a Non-Gaussian, *or Gaussian-related*, random field, $Y(\boldsymbol{x})$, at any fixed $\boldsymbol{x} \in \mathbb{R}^N$ such that:

$$Y(\boldsymbol{x}) = F(\boldsymbol{Z}(\boldsymbol{x})) = F(Z_0(\boldsymbol{x}), ..., Z_{k-1}(\boldsymbol{x})) \tag{2.18}$$

The parameter k is called the degree of freedom of the Non-Gaussian random field.

Example 2.4.1. *A t random field, with k degrees of freedom [7], is defined taken F such that*

$$F(\boldsymbol{Z}) = \frac{Z_0\sqrt{k}}{(\sum_{i=1}^{k} Z_i^2)^{\frac{1}{2}}} \tag{2.19}$$

which has a marginal density function, for $y \in \mathbb{R}$, given as:

$$t(y) = \frac{\Gamma((k+1)/2)}{\Gamma(k/2)(\pi k)^{1/2}} \left(1 + \frac{y^2}{k}\right)^{-(k+1)/2} \tag{2.20}$$

where $\Gamma(.)$ is the Gamma function.

One can find other interesting examples in [Adl81, Wor94, Cao97, CW99].

5. In the literature, the second spectral moment of isotropic random fields is denoted by λ_2 to refer to their order. In this thesis, we will use the notation λ to refer to these moments in the case of isotropic random fields.

6. The assumption that a random field, Y, has a constant variance yields that Y and its first-order derivative, *if differentiable*, are uncorrelated.

7. In the next chapters of this thesis, we will denote the degree of freedom of the t field by ν.

2.5 Conclusion

This chapter has reviewed some basics about the random fields and their properties required for further developments in this thesis. Starting from the definition of the random fields, and the covariance function. We focused on stationary random fields, that can be generated immediately using the spectral representation theorem, and showed that the structural properties of *"weakly"* stationary random fields can be determined from the covariance function, such as isotropy and anisotropy. More attention has been focused on the Gaussian and a class of Non-Gaussian random fields called *Gaussian-related random fields*. The former, if centred, is completely determined by its covariance function, and the latter is defined using a transformation function of a centred vector valued Gaussian random field of independent and identically distributed components.

In the next chapter we introduce the geometric properties of the excursion sets of random fields, derived from the integral geometry.

Chapter 3

Geometry of random fields

Contents

3.1 Excursion sets 27
3.2 Regularity conditions 28
3.3 Expectations 29
3.3.1 Case of isotropy 29
3.3.2 Non-isotropic random fields on smooth manifolds 30
3.3.3 Stationary random fields over rectangles on $\mathbb{R}^N$ 31
3.4 Mean intrinsic volumes of excursion sets 32
3.5 Conclusion 33

3.1 Excursion sets

Let $Y(\boldsymbol{x})$, $\boldsymbol{x} \in \mathbb{R}^N$, be a stationary real-valued random field. An excursion set (see Example 3.1.1), denoted by $E_h(Y, S)$, of Y inside a compact subset $S \subset \mathbb{R}^N$ above a level h, is defined as:

$$E_h(Y, S) = \{\boldsymbol{x} \in S : Y(\boldsymbol{x} \geq h)\} \tag{3.1}$$

Example 3.1.1. *In this example, figure 3.1 illustrates a two-dimensional excursion set obtained from a homogeneous Gaussian random field above the levels $h = -1$, and $h = 2.5$:*

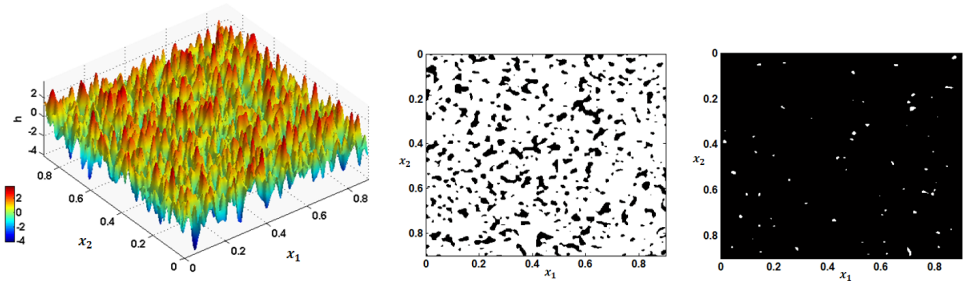

(a) (b) (c)

Figure 3.1: (a). A simulation example of a two-dimensional Gaussian random field on a unit rectangle. (b). and (c). The excursion sets above the levels $h = -1$, and 2.5, respectively.

Another notation can be found in the literature for the excursion sets which is expressed as $Y^{-1}([h,\infty))$, [Adl81].
The geometric properties of the excursion sets of random fields were pioneered by [Adl81, Wor94] and recently investigated in [Cao97, AT07, Tay08], for Gaussian and Gaussian-related random fields. For $N-$dimensional excursion set there is $N+1$ numerical quantifiers, known under several names such as Minkowski functionals (MFs), intrinsic volumes, and Lipschitz-Killing curvatures (LKCs), which describe the geometry and the topology of these sets. As example, in two-dimensions, they measure the area, the boundary length, and the Euler-Poincaré characteristic which counts the number of connected components minus the number of holes. In three dimensions, they measure the volume, the surface area, the mean curvature length, and the Euler-Poincaré characteristic which counts this time the number of connected components minus the number of handles plus the number of holes. The basic approaches to develop the geometry of these sets could be derived from integral geometry [San76] and differential topology [MC69].
These geometric quantifiers are of special interest since they provide a complete description of the geometric structure of the excursion sets. Furthermore, [Adl81, Has78] showed that when the excursion set is obtained at a very high level, the expected Euler-Poincaré characteristic converges with probability one to the number of the local maxima of the random field, since the excursion sets will consist of only connected component with no more holes, (see Fig. 3.1(c)).

In order to tackle this subject, there is certain regularity conditions that a random field, and the subset S should satisfy, as will be seen in the next section.

3.2 Regularity conditions

The excursion sets, in this thesis, are restricted to be defined on a bounded rectangle in $\mathbb{R}^N$ of the form $S=\prod_{i=1}^{N}[0,L_i]$, $0<L_i<\infty$, with $(N-1)-$dimensional boundary, ∂S.
Let $Y = Y(\boldsymbol{x})$ be as considered in the previous section 3.1, and let $\dot{Y}_j(\boldsymbol{x}) = \partial Y(\boldsymbol{x})/\partial x_j$ and $\ddot{Y}_{kj}(\boldsymbol{x}) = \partial^2 Y(\boldsymbol{x})/\partial x_k \partial x_k$, for $j,k = 1,...,N$. Then, the regularity conditions that $Y(\boldsymbol{x})$ should hold are:

(i) for any $\varepsilon > 0$:

$$P\left(max\left\{\omega_j(\tau),\omega_{jk}(\tau)\right\} > \varepsilon\right) = o(\tau^N) \quad \text{as } \tau \downarrow 0 \tag{3.2}$$

where ω_j and ω_{jk} are the moduli of continuity of $\dot{Y}_j$ and $\ddot{Y}_{kj}$, respectively, inside S and they are defined, for all $\boldsymbol{x},\boldsymbol{s} \in S$, $j,k = 1,...,N$, as:

$$\omega_j(\tau) = \sup_{\|\boldsymbol{x}-\boldsymbol{s}\|<\tau} |\dot{Y}_j(\boldsymbol{x}) - \dot{Y}_j(\boldsymbol{s})|, \quad \omega_{jk}(\tau) = \sup_{\|\boldsymbol{x}-\boldsymbol{s}\|<\tau} |\ddot{Y}_{jk}(\boldsymbol{x}) - \ddot{Y}_{jk}(\boldsymbol{s})| \tag{3.3}$$

(ii) $\ddot{\boldsymbol{Y}}$ has finite variances conditional on $(Y,\dot{\boldsymbol{Y}})$, where $\ddot{\boldsymbol{Y}}$ is the $N\times N$ Hessian matrix of Y, and $\dot{\boldsymbol{Y}}$ is the $N-$vector gradient of Y.

(iii) the density of $(Y, \dot{\boldsymbol{Y}})$ is bounded above, uniformly for all $\boldsymbol{x} \in S$.

(iv) the marginal densities of $\dot{\boldsymbol{Y}}$ are continuous at 0, uniformly for all $\boldsymbol{x} \in S$.

Once a stationary random field, Y, satisfies the previous regularity conditions, the following results, due to [Adl81, Wor95] and reported in [Cao97, AT07], about the expected Euler-Poincaré characteristic and the expected number of the local maxima of Y can be represented.

3.3 The expected Euler-Poincaré characteristic and the expected number of local maxima of random fields

Let $M_h^+(Y, S)$ be the number of the local maxima above a level h of a stationary random field $Y(\boldsymbol{x})$ on S. Then, under the first three regularity conditions reported in section 3.2, the expectation of $M_h^+(Y, S)$, [Adl81], is:

$$\mathbb{E}(M_h^+(Y,S)) = vol(S) \int_h^\infty \mathbb{E}[-\det(\ddot{\boldsymbol{Y}}^-)|Y = y, \boldsymbol{Y} = \boldsymbol{0}]p_N(y, \boldsymbol{0})dy \tag{3.4}$$

where $vol(S)$ is the Lebesgue measure, or *the $N-$dimensional volume*, of S, and $p_N(y, \boldsymbol{0})$ is the joint density of $(Y, \dot{\boldsymbol{Y}})$ at $(y, \boldsymbol{0})$, where $\dot{\boldsymbol{Y}} \in \mathbb{R}^N$, at any fixed $\boldsymbol{x} \in S$. Under the regularity conditions given in section 3.2, then based on Morse's theorem [MC69], *(one of the important results of differential topology)*, [Wor95] proved that the expected Euler-Poincaré characteristic for stationary random fields is represented as:

$$\begin{aligned}\mathbb{E}[\chi(E_h(Y,S))] =& vol(S)\mathbb{E}[(Y \geq h)\det(-\ddot{\boldsymbol{Y}})|\dot{\boldsymbol{Y}} = \boldsymbol{0}]p_{\dot{\boldsymbol{Y}}}(\boldsymbol{0}) \\ &+ \int_{\partial S} \mathbb{E}[(Y \geq h)(\dot{Y}_\perp < 0)\det(-\ddot{\boldsymbol{Y}}_\top - \dot{Y}_\perp c)|\dot{\boldsymbol{Y}}_\top = \boldsymbol{0}]p_{\dot{\boldsymbol{Y}}_\top}(\boldsymbol{0})\end{aligned} \tag{3.5}$$

where $p_{\dot{\boldsymbol{Y}}}$, $p_{\dot{\boldsymbol{Y}}_\top}$ are the probability density functions of $\dot{\boldsymbol{Y}}$ and $\dot{\boldsymbol{Y}}_\top$, respectively. At any point $x \in \partial S$, $\dot{Y}_\perp$ is the gradient of Y in the direction of the inside normal to ∂S, $\dot{\boldsymbol{Y}}_\top$ is the gradient $(N-1)-$vector in the tangent plane to ∂S, $\ddot{\boldsymbol{Y}}_\top$ is the $(N-1) \times (N-1)$ Hessian matrix in the tangent plane to ∂S, and c is the $(N-1) \times (N-1)$ inside curvature matrix of ∂S.
The first term of (3.5) can be written as $vol(S)\rho_N(h)$, where $\rho_N(h)$ is the density of Euler-Poincaré characteristic of the excursion set E_h, per unit volume:

$$\rho_N(h) = \mathbb{E}[(Y \geq h)\det(-\ddot{\boldsymbol{Y}})|\dot{\boldsymbol{Y}} = \boldsymbol{0}]p_{\dot{\boldsymbol{Y}}}(\boldsymbol{0}) \tag{3.6}$$

3.3.1 Case of isotropy

In the case Y is an isotropic random field, Worsley [Wor95] gave a simplification of the expectations for both $\rho_j(h)$ and $\mathbb{E}[\chi(E_h(Y, S))]$.
Let $\dot{\boldsymbol{Y}}_{|j}$ be the vector gradient of the first j components of $\dot{\boldsymbol{Y}}$, and $\ddot{\boldsymbol{Y}}_j$ is the $j \times j$

matrix of the first j rows and columns of $\ddot{\boldsymbol{Y}}$, then the $j-$dimensional EC density [1] is defined, for $j > 0$, as:

$$\rho_j(h) = \mathbb{E}[\dot{Y_j^+}\det(-\ddot{\boldsymbol{Y}}_{|j-1})|\dot{\boldsymbol{Y}}_{|j-1} = \boldsymbol{0}, Y = h]p_{|j-1}(\boldsymbol{0}, h) \tag{3.7}$$

where $\dot{Y}_j^+ = max(0, \dot{Y}_j)$, and $p_{|j-1}(\boldsymbol{0}, h)$ is the joint probability density function of $\dot{\boldsymbol{Y}}_{|j-1}$ and Y. For $j = 0$, $\rho_0(h) = \mathbb{P}[Y \geq h]$.
Thus, under isotropy, and the regularity conditions given in section 3.2, the expected Euler-Poincaré characteristic is:

$$\mathbb{E}[\chi(E_h(Y, S))] = vol(S)\rho_N(h) + \sum_{j=0}^{N-1}\left(\frac{1}{\omega_{N-j}}\int_{\partial S}\mathrm{detr}_{N-1-j}(\boldsymbol{c})dx\right)\rho_j(h) \tag{3.8}$$

where $\boldsymbol{c}$ is the $(N-1)\times(N-1)$ inside curvature matrix of ∂S at a point $x \in \partial S$, $\mathrm{detr}_j(\boldsymbol{c})$, $(j = 0, .., N-1)$, is the sum of the determinants of all $j \times j$ principal minors of $\boldsymbol{c}$, and $\omega_j = 2\pi^{j/2}/\Gamma(j/2)$ is the surface area of unit $(j-1)-$sphere in $\mathbb{R}^j$. The term $\frac{1}{\omega_{N-j}}\int_{\partial S}\mathrm{detr}_{N-1-j}(\boldsymbol{c})dx$ is the $j-$dimensional curvature measure of S. Together with Lebesgue measure of S, $vol(S)$, they are the $(N+1)$ intrinsic volumes, or equivalently Minkowski functionals of S, denoted by $\mathcal{M}_j(S)$, $(j = 0, .., N)$.
Consequently, $\mathbb{E}[\chi(E_h(Y, S))]$, for isotropic random fields, can finally be expressed in terms of $j-$dimensional Minkowski functionals of S as:

$$\mathbb{E}[\chi(E_h(Y, S))] = \sum_{j=0}^{N}\mathcal{M}_j(S)\rho_j(h) \tag{3.9}$$

3.3.2 Non-isotropic random fields on smooth manifolds

The last expectation in equation (3.9), has been extended [TA03, Tay08] to deal with non-isotropic random fields on smooth manifolds with piece-wise smooth boundaries. It was shown that if a random field is defined as a function of i.i.d. non-isotropic Gaussian random fields, then it is only necessary to replace Minkowski functionals $\mathcal{M}_j(S)$ by Lipschitz-Killing curvatures (LKCs) of S, denoted by $\mathcal{L}_j(S)$, such that:

$$\mathbb{E}[\chi(E_h(Y, S))] = \sum_{j=0}^{N}\mathcal{L}_j(S)\rho_j(h) \tag{3.10}$$

Thus, the non-isotropy property is transferred from the EC densities to LKC, and one can find the EC densities using the formulae in equation (3.9).
The LKCs of S measure the intrinsic volume of S in the Riemannian metric defined by the variogram [2]. For $N-$dimensional and $(N-1)-$dimensional LKC, they have

1. $\rho_j(h)$ is the density of Euler-Poincaré characteristic in any $j-$dimensional Euclidean subspace of $\mathbb{R}^N$, [Wor95]

2. The variogram of a real-valued function Z between any two points $x, s \in \mathbb{R}^N$ is defined as:

$$Var(Z(\boldsymbol{x}) - Z(\boldsymbol{s})) \tag{3.11}$$

a very simple expression. Suppose Y is a random field defined from a transformation function of i.i.d. non-isotropic Gaussian random fields, Z_k, $(k = 1, ..., \nu)$, with constant variance σ^2. Then:

$$\mathcal{L}_N(S) = \sigma^{-N} \int_S [\det(\boldsymbol{\Lambda}(\boldsymbol{x}))]^{1/2} \, \boldsymbol{dx} \tag{3.12}$$

and

$$\mathcal{L}_{N-1}(S) = \frac{1}{2\sigma^{(N-1)}} \int_{\partial S} [\det(\boldsymbol{\Lambda}_{\partial S}(\boldsymbol{x}))]^{1/2} \, \mathcal{H}_{N-1}(\boldsymbol{dx}) \tag{3.13}$$

where $\boldsymbol{\Lambda}(\boldsymbol{x}) = Var(\dot{\boldsymbol{Z}}_{\boldsymbol{k}}(\boldsymbol{x}))$ is the $N \times N$ matrix of second order spectral moments, or *the variance-covariance matrix*, of the gradient $N-$vector $\dot{\boldsymbol{Z}}_{\boldsymbol{k}}(\boldsymbol{x})$, and similarly $\boldsymbol{\Lambda}_{\partial S}(\boldsymbol{x}) = Var(\dot{\boldsymbol{Z}}_{\boldsymbol{k}\top}(\boldsymbol{x}))$ is the $(N-1) \times (N-1)$ variance-covariance matrix of the gradient $(N-1)-$vector of $\dot{\boldsymbol{Z}}_{\boldsymbol{k}}(\boldsymbol{x})$ tangential to the boundary ∂S, and $\mathcal{H}_{N-1}$ is the $(N-1)-$dimensional Hausdorff measure [HS02] on ∂S, for any selected k.
The lower dimensional LKCs have not simple formulae, except for $\mathcal{L}_0 = \chi(S)$. One can find the explicit expressions of the LKCs in [TA03]. Note that in the isotropic case the equations (3.9) and (3.10) are equivalent, and if the random field, Y, is stationary then they are:

$$\mathcal{L}_j(S) = \mathcal{M}_j(\Lambda^{1/2} S) \tag{3.14}$$

3.3.3 Stationary random fields over rectangles on $\mathbb{R}^N$

Let $S = \prod_{i=1}^{N} [0, L_i]$ be a rectangle on $\mathbb{R}^N$, and suppose J be a face of $k-$dimensions in S, $(J \in \partial_k S)$, where $\partial_k S$ is the collection of faces of dimension k in S. The set $\partial_N S$ contains the entire S, $\partial_0 S$ includes 2^N vertices of the rectangle S, and $\partial_k S$ has $2^{N-k}\binom{N}{k}$ faces of $k-$dimensions (see Fig. 9.3 as example). Then,

$$\begin{aligned} J = \{x \in \mathbb{R}^N : x_i = \varepsilon_i L_i, \text{if } i \notin \sigma(J), 0 \leq x_i \leq L_i, \\ \text{if } i \in \sigma(J)\} \end{aligned} \tag{3.15}$$

where $\sigma(J) \subseteq \{1, ..., N\}$, and $\varepsilon(J) = \{\varepsilon_i, i \notin \sigma(J)\}$ is a sequence of $N - k$ zeros and ones. Then, the Lipschitz-Killing curvatures of S are given by

$$\mathcal{L}_j(S) = \sum_{J \in \mathcal{O}_j} |\det(\boldsymbol{\Lambda}_J)|^{1/2} vol_j(J) \tag{3.16}$$

where $\boldsymbol{\Lambda}_{\boldsymbol{J}}$ is the $k \times k$ matrix of the second order spectral moments associated with the $k-$dimensional face J. Thus, the expected Euler-Poincaré characteristic can be given by:

$$\mathbb{E}[\chi(E_h(Y, S))] = \sum_{j=0}^{N} \left(\sum_{J \in \mathcal{O}_j} |\det(\boldsymbol{\Lambda}_J)|^{1/2} vol_j(J) \right) \rho_j(h) \tag{3.17}$$

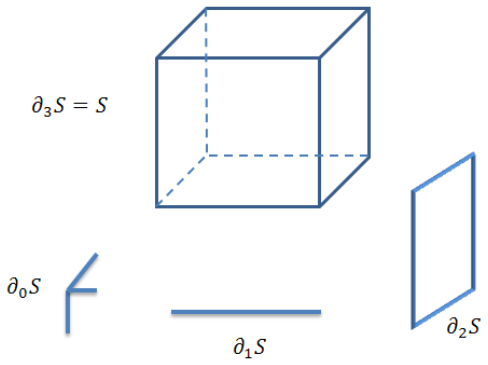

Figure 3.2: Example of a rectangle in $\mathbb{R}^3$, and its $k-$dimensional faces, $k = 0, ..., 3$.

3.4 Mean intrinsic volumes of excursion sets

Besides the expected Euler-Poincaré characteristic of the excursion sets, another geometric quantifiers appeared in its explicit formula, known as Lipschitz-Killing curvatures or Minkowski functionals of the metric space S, can also be defined over these excursion sets. In this case, the aim is to find the mean intrinsic volumes, or *mean Lipschitz-Killing curvatures*, of the excursion sets that describe their geometric structures, such as their size, boundary length, and etc.
Let Y be a real-valued stationary random field defined by a smooth transformation of i.i.d. non-isotropic stationary Gaussian random fields, then the following expression, proved by [AT03] and reported in [AT07, Adl08, AT11], gives the mean intrinsic volumes of the excursion sets of Y:

$$\mathbb{E}[\mathcal{L}_j(E_h(Y,S))] = \sum_{k=0}^{N-j} \begin{bmatrix} j+k \\ k \end{bmatrix} \mathcal{L}_{j+k}(S)\rho_k(h) \tag{3.18}$$

where $\begin{bmatrix} j+k \\ k \end{bmatrix}$ is the flag coefficient [3], $\rho_j(h)$ are the EC densities for Y, and $\mathcal{L}_j(S)$ are the LKCs of S with respect to the Riemannian metric induced on S by Y.
Note that, when $j = 0$, then $\mathbb{E}[\mathcal{L}_0(E_h(Y,S))] = \mathbb{E}[\chi(E_h(Y,S))]$ is the expected Euler-poincaré characteristic of E_h, given in the previous section.
The last expression in equation (3.18) has been proved for isotropic Gaussian random fields as the result of Crofton's formula and Hadwiger's formula. Then, it was extended to the non-isotropic Gaussian random fields and the class of non-Gaussian random fields defined in chapter 2.

3. The flag coefficient is defined as

$$\begin{bmatrix} n \\ k \end{bmatrix} = \frac{n!}{k!(n-k)!}\frac{\omega_n}{\omega_k\omega_{n-k}}, \tag{3.19}$$

where $\omega_k = \frac{\pi^{k/2}}{\Gamma\left(\frac{k}{2}+1\right)}$ is the volume of the unit ball in $\mathbb{R}^k$

Suppose a regular (convex) set $E \subset \mathbb{R}^N$, then Crofton's formula [San76, Bla36] states that under the affine Grassmanian [4], Graff(N,k), of $k-$dimensional linear subspaces of $\mathbb{R}^k$, $(k = 0, ..., N)$,

$$\int_{Graff(N,N-k)} \mathcal{L}_j(E \cap V) d\mu^N_{N-k}(V) = \left[\begin{array}{c} k+j \\ j \end{array} \right] \mathcal{L}_{k+j}(E) \tag{3.21}$$

where μ^N_k is a Haar measure, and $V \in Graff(N,k)$. The special case is when $j = 0$, then Crofton's formula becomes the known Hadwiger's formulae [Had57] so that

$$\mathcal{L}_k(E) = \int_{Graff(N,N-k)} \mathcal{L}_0(E \cap V) d\mu^N_{N-k}(V) \tag{3.22}$$

Hadwiger's formula shows that Lipschitz-Killing curvatures of the set E can be obtained from the Euler-Poincaré characteristic of the cross-sections, of various dimensions, of the set E.
For an isotropic Gaussian random field Y, one need to find the expectations of Lipschitz-Killing curvatures of the excursion set $E_h(Y,S)$. Thus, [AT03] showed that $\mathbb{E}[\mathcal{L}_j(E_h(Y,S))]$ can be obtained immediately from Hadwiger's formula. Replacing the set E by the excursion sets $E_h(Y,S)$ of Y, we have

$$\begin{aligned} \mathbb{E}[\mathcal{L}_k(E_h(Y,S))] &= \int_{Graff(N,N-k)} \mathbb{E}[\mathcal{L}_0(E_h(Y,S) \cap V)] d\mu^N_{N-k}(V) \\ &= \sum_{j=0}^{N-k} \rho_j(h) \int_{Graff(N,N-k)} \mathcal{L}_j(S \cap V) d\mu^N_{N-k}(V) \\ &= \sum_{j=0}^{N-k} \left[\begin{array}{c} k+j \\ j \end{array} \right] \mathcal{L}_{j+k}(S) \rho_j(h) \end{aligned} \tag{3.23}$$

Further details and proofs of the expression in (3.18) for the non-isotropic Gaussian and the non-Gaussian random fields can be found in [AT03, AT07, Adl08, AT11].

3.5 Conclusion

This chapter highlights the basic results in both integral geometry and differential topology that enables estimating the geometric structure of the random excursion sets. At the first stage, the expected number of the local maxima of a regular random field, and the expected Euler-Poincaré characteristic of its excursion sets

4. The Grassmanian of $k-$dimensional linear subspaces of $\mathbb{R}^k$, $(k = 0, ..., N)$ is a compact homogeneous space with respect to the rotation group [SW08]. The affine Grassmanian $G_r(N,k)$ is locally compact homogeneous space with respect to the motion group and carries a locally finite motion invariant measures, denoted by μ_k, and normalized so that

$$\mu^N_k\left(G_r(N,k)\right) = \left[\begin{array}{c} N \\ k \end{array} \right] \tag{3.20}$$

.

are reviewed. The expected Euler-Poincaré characteristic of the excursion sets obtained at high threshold becomes very close to the number of the local maxima, and for higher thresholds it tends to that number with probability one, since the excursion set will include only the number of the connected components, whereas the holes will disappear. In the second stage, a general formulae of the geometric structure of the excursion sets known as the mean intrinsic volumes, or mean Lipschitz-Killing curvatures are expressed by Hadwiger's formulae, which states that one can characterise the geometry of a given set using Euler-Poincaré characteristic of its lower dimensional cross-sections. For the random fields, the mean intrinsic volumes including the expected Euler-Poincaré characteristic are expressed in terms of the intrinsic volumes of the metric space, and the EC densities which depend on the random field model. In the next part, we will give the expectations of the EC densities of some interesting non-Gaussian random fields, that were not evaluated in the literature, in order to estimate their local maxima (or minima) and to estimate the LKCs of their excursion sets. The interest of these geometric descriptors is derived in the application part.

Part III

THEORETICAL DEVELOPMENTS

Chapter 4

Linear mixture random fields

Contents

4.1 Introduction . . . 37
4.2 Linear mixed Gaussian−t distribution . . . 37
4.2.1 Univariate distribution . . . 37
4.2.2 Mixed Gaussian−t multivariate distribution . . . 38
4.3 Mixed Gaussian−t random field, GT^{ν}_{β} . . . 38
4.3.1 Definition . . . 38
4.3.2 Representation of derivatives . . . 39
4.4 The EC densities of the GT^{ν}_{β} excursion sets . . . 40
4.5 The extreme values of the Gaussian−t random field . . . 43
4.6 The expected intrinsic volumes of the GT^{ν}_{β} excursion sets over rectangles of $\mathbb{R}^2$ . . . 44
4.7 Simulation Results . . . 44
4.8 Conclusion . . . 46

4.1 Introduction

This chapter defines a class of mixed random fields that results from the linear sum of Gaussian and non-Gaussian random fields, exclusively, student's t random fields, or so called $t-$fields, defined on a non-empty compact subsets of the two-dimensional euclidean space $\mathbb{R}^2$. We are interested in studying the behaviour of the mixed Gaussian-t random fields using their geometric and topological characteristics, namely intrinsic volumes (Lipschitz-Killing curvatures LKCs), or equivalently Minkowski functionals with respect to normalization. We gave the explicit formulae of these functionals for the two-dimensional excursion sets, [AP12, AP13a], in order to model the topography of real surfaces, (see the application part). Then, we studied the behaviour of the Gaussian-t random field near its extremal points using the expected Euler-Poincaré characteristic on simulation examples.

4.2 Linear mixed Gaussian−t distribution

4.2.1 Univariate distribution

Definition 4.2.1. *Let $G \sim Normal(0,1)$ be a random variable of standard normal distribution and $T \sim t_\nu$ be a student's t random variable with ν degrees of free-*

dom independent of G. A random variable Y is said to have a mixed Gaussian−t distribution if it is expressed as:

$$Y = \mu_Y + \sigma_Y(G + \beta T^\nu), \tag{4.1}$$

where ν_Y, σ_Y^2 are the mean and the variance of Y, respectively, and $\beta \in \mathbb{R}^+ \setminus \{0\}$. A random variable Y that has a mixed Gaussian−t distribution will be denoted by $(Y \sim GT_\beta^\nu)$.

The probability density function of Y, denoted by $p_Y(y)$, is then the convolution between the G and T^ν probability density functions, and it is written by:

$$p_Y(y) = \frac{\Gamma\left(\frac{\nu+1}{2}\right)}{2\pi\beta\sigma_Y\Gamma\left(\frac{\nu}{2}\right)\left(\frac{\nu}{2}\right)^{1/2}} \int_{-\infty}^{\infty} \left(1 + \frac{(y-\mu_Y-u)^2}{\beta^2\sigma_Y^2\nu}\right)^{-\frac{\nu+1}{2}} e^{-u^2/2\sigma_Y^2} du, \tag{4.2}$$

4.2.2 Mixed Gaussian−t multivariate distribution

Let $\mathbf{Y} = (Y_1, ..., Y_d)^t, (d > 1)$ be $\mathbb{R}^d$-valued random variable on $\mathbb{R}^d$, where each vector component Y_i is represented as:

$$Y_i = G_i + \beta_i T_i^\nu, \ \ (i = 1, ..., d) \tag{4.3}$$

Then, $\mathbf{Y}$ has a mixed Gaussian−t multivariate distribution with ν degrees of freedom, and its probability density function is given by:

$$p_{\mathbf{Y}}(\mathbf{y}) = \phi(\mathbf{y}; \Sigma_G) * t_d(\mathbf{y}; \boldsymbol{\beta}, \nu, \Sigma), \ \ \mathbf{y} \in \mathbb{R}^d \tag{4.4}$$

where $\phi(\mathbf{y}; \Sigma)$ is the multivariate normal probability density function (pdf) of the d−dimensional normal vector $\mathbf{G}$ with the $(d \times d)$ covariance matrix Σ_G, and $t_d(.; \boldsymbol{\beta}, \nu, \Sigma)$ is the d−dimensional pdf of the t variate with ν degrees of freedom, $(d \times d)$ covariance matrix Σ, and scale vector $\boldsymbol{\beta} = (\beta_1, ..., \beta_d)^t$.

4.3 Mixed Gaussian−t random field, GT_β^ν

Let $\{Y(\boldsymbol{x}) : \boldsymbol{x} \in S\}$, be a stationary random field on a non-empty compact subset $S \subset \mathbb{R}^N$, then $Y(\boldsymbol{x})$ belongs to the mixed Gaussian-t random fields if it is defined as follows:

4.3.1 Definition

Let $Z_0(\boldsymbol{x}), Z_1(\boldsymbol{x}), ..., Z_\nu(\boldsymbol{x})$, $x \in S$, be centered, homogeneous, independent, and identically distributed (i.i.d.) Gaussian random fields, with unit variance, and with $\mathrm{Var}(\partial Z_i/\partial \boldsymbol{x}) = \boldsymbol{\Lambda}$, $(i = 0, ..., \nu)$. Let $G(\boldsymbol{x})$ be a stationary centered real-valued

Gaussian random field, independent of all Z_i, $(i = 0, ..., \nu)$, with unit variance, and $\mathrm{Var}(\partial G/\partial \boldsymbol{x}) = \boldsymbol{\Lambda}_G$. Then, for a real value $\beta > 0$, the sum given by:

$$Y(\boldsymbol{x}) = G(\boldsymbol{x}) + \frac{\beta Z_0(\boldsymbol{x})}{\left[\sum_{k=1}^{\nu} Z_k^2(\boldsymbol{x})/\nu\right]^{1/2}}, \tag{4.5}$$

defines a stationary GT^{ν}_{β} real-valued random field with ν degrees of freedom, at any fixed point $\boldsymbol{x} \in S$. The marginal distribution of $Y(\boldsymbol{x})$ at any fixed $\boldsymbol{x}$ is the GT^{ν}_{β} probability density function, given in equation (4.2), with ν degrees of freedom. Notice that the second term in the right hand of the equation (4.5) is the t−field with ν degrees of freedom, and with the scale factor β. It is restricted to the condition $\nu > N$, in order to ensure that the t−field is well defined with almost no zeros in the denominator, [Wor94]. Thus, the definition of $Y(\boldsymbol{x})$ well be restricted to $\nu > N$.

4.3.2 Representation of derivatives

Following Lemmas A.0.1 and A.0.3, in the appendix part, in the next Lemma, the first and second derivatives of the mixed Gaussian−t random field $Y(\boldsymbol{x})$ can be directly expressed in terms of independent random variables.

Lemma 4.3.1. *The first and second derivatives $\dot{\boldsymbol{Y}}$, and $\ddot{\boldsymbol{Y}}$ of the mixed Gaussian−t random field, $Y = Y(\boldsymbol{x})$, can be expressed in terms of independent random variables at any fixed point $\boldsymbol{x} \in S$ as follows:*

$$(i)\quad \dot{\boldsymbol{Y}} = \boldsymbol{z_1} + \beta\nu^{1/2}\left(1 + \frac{(Y-G)^2}{\beta^2\nu}\right) W^{-1/2}\boldsymbol{z_2}$$

$$(ii)\quad \ddot{\boldsymbol{Y}} = -G\boldsymbol{\Lambda}_G + \boldsymbol{V} + \beta\nu^{1/2}\left(1 + \frac{(Y-G)^2}{\beta^2\nu}\right) W^{-1}\{-\beta^{-1}\nu^{-1/2}(Y-G)(\boldsymbol{Q} - 2\boldsymbol{z_2}\boldsymbol{z_2^t}) - \boldsymbol{z_2}\boldsymbol{z_3^t} - \boldsymbol{z_3}\boldsymbol{z_2^t} + W^{1/2}\boldsymbol{H}\}$$

where $G \sim Normal_1(0,1)$, $W \sim \chi^2_{\nu+1}$, $\boldsymbol{z_1} \sim Normal_N(0, \boldsymbol{\Lambda}_G)$, $\boldsymbol{z_2}, \boldsymbol{z_3} \sim Normal_N(0, \boldsymbol{\Lambda})$, $\boldsymbol{Q} \sim Wishart_N(\boldsymbol{\Lambda}, \nu - 1)$, $\boldsymbol{V} \sim Normal_{N\times N}(0, \boldsymbol{M(\Lambda_G)})$, and $\boldsymbol{H} \sim Normal_{N\times N}(0, \boldsymbol{M(\Lambda)})$, all independently.

In the next section, we will focus on calculating the EC densities of the two-dimensional excursion sets of the Gaussian−t random field, $Y(\boldsymbol{x})$. Toward this aim, $Y(\boldsymbol{x})$ should be considered suitably regular in order to use the derivatives in Lemma 4.3.1. It is trivial that $Y(\boldsymbol{x})$ satisfies the regularity conditions discussed in chapter 3 (section 3.2), since both Gaussian and t−field do, as proved by [Adl81] and [Wor94], respectively. Notice that if $\boldsymbol{\Lambda}_G = \boldsymbol{\Lambda}$, then one can use the coordinate transformation $\tilde{\boldsymbol{x}} = \boldsymbol{\Lambda}^{1/2}\boldsymbol{x}$ to simplify the calculations. In our case, we will keep the coordinates and we will assume that the variance-covariance matrix $\boldsymbol{\Lambda}_G$ and $\boldsymbol{\Lambda}$ are not equal, for generality.

4.4 The EC densities of the GT^{ν}_{β} excursion sets

In the following theorem we derive the first three EC densities of the two-dimensional mixed Gaussian$-t$ random field, $Y(\boldsymbol{x})$, $\boldsymbol{x} \in S$, where $S \subset \mathbb{R}^N$, $N = 2$. To prove this theorem, we shall use some Lemmas and theorems given in [Adl81, Wor94, CW99].

Theorem 4.4.1. *The $j-$th dimensional EC density, $\rho_j(.)$, $j = 0, 1, 2$ for an isotropic GT^{ν}_{β} random field, $Y(\boldsymbol{x})$, $\boldsymbol{x} \in \mathbb{R}^2$, with ν degrees of freedom, $\nu > 2$, and $\beta > 0$, can be expressed at a given level h as follows:*

$$
\begin{aligned}
(i)\quad \rho_0(h) &= \frac{\Gamma\left(\frac{\nu+1}{2}\right)}{(2\pi)\beta\Gamma\left(\frac{\nu}{2}\right)\left(\frac{\nu}{2}\right)^{1/2}} \int_h^{\infty}\int_{-\infty}^{\infty} \left(1+\frac{(y-u)^2}{\beta^2\nu}\right)^{-\frac{\nu+1}{2}} e^{-u^2/2} du dy \\
(ii)\quad \rho_1(h) &= \frac{\lambda^{1/2}}{(2\pi)^{3/2}} \int_{-\infty}^{\infty} \left(1+\frac{(h-u)^2}{\beta^2\nu}\right)^{-\frac{\nu-1}{2}} e^{-u^2/2} du \\
&\quad + \frac{\lambda_G^{1/2}\Gamma\left(\frac{\nu+1}{2}\right)}{(2\pi)^{3/2}\beta\sqrt{\nu}\Gamma\left(\frac{\nu}{2}\right)} \int_{-\infty}^{\infty} \left(1+\frac{(h-u)^2}{\beta^2\nu}\right)^{-\frac{\nu+1}{2}} e^{-u^2/2} du \\
(iii)\quad \rho_2(h) &= \frac{2^{\frac{1}{2}}\lambda\Gamma\left(\frac{\nu+1}{2}\right)}{(2\pi)^2\Gamma\left(\frac{\nu}{2}\right)} \int_{-\infty}^{\infty} \frac{(h-u)}{\beta\sqrt{\nu}} \left(1+\frac{(h-u)^2}{\beta^2\nu}\right)^{-\frac{\nu-1}{2}} e^{-u^2/2} du \\
&\quad + \frac{\lambda_G\Gamma\left(\frac{\nu+1}{2}\right)}{(2\pi)^2\Gamma\left(\frac{\nu}{2}\right)\beta\sqrt{\nu/2}} \int_{-\infty}^{\infty} u \left(1+\frac{(h-u)^2}{\beta^2\nu}\right)^{-\frac{\nu+1}{2}} e^{-u^2/2} du
\end{aligned}
$$

where $\boldsymbol{\Lambda}_G = \lambda_G \boldsymbol{I}_2$, and $\boldsymbol{\Lambda} = \lambda \boldsymbol{I}_2$.

Proof. In this proof the general formula of the EC density given in chapter 3 will be used. Furthermore, the expectations will be evaluated by conditioning on the Gaussian component, $G = u$, on $Y = h$ and on W, where W is independent of both Y and G, as follows:

$$
\rho_j(h) = (-1)^{j-1} \int_{-\infty}^{\infty} \mathbb{E}_W \Big[\mathbb{E}\left(\dot{Y}_j^{+} \det(\ddot{\boldsymbol{Y}}_{|j-1}) | \dot{Y}_1 = 0, ..., \dot{Y}_{j-1} = 0, Y = h, G = u, W \right) p_{\tilde{\dot{\boldsymbol{Y}}}}(\boldsymbol{0}; h, G, W) \Big] p_Y(h; G = u) \phi(u) du
$$

where the term $\ddot{\boldsymbol{Y}}_{|j-1}$ represents the sub-matrix of the first $(j-1)\times(j-1)$ elements of the Hessian matrix $\ddot{\boldsymbol{Y}}$ with respect to $x_1, ..., x_{j-1}$, and $\dot{Y}_j$ refers to the $j-$th component of the gradient $\dot{\boldsymbol{Y}}$ with respect to x_j. $p_{\tilde{\dot{\boldsymbol{Y}}}}(\boldsymbol{0}; h, G)$ is the joint probability density of the first $(j-1)$ component of $\dot{\boldsymbol{Y}}$, denoted $\tilde{\dot{\boldsymbol{Y}}}$, at zero conditional on $Y = h$, W, and G. Whereas $p_Y(h; G = u)$ is the probability density function of $Y = h$ conditional on $G = u$, and $\phi(u)$ is the normal probability density function.

Conditional on $G = u$, Y is a $t-$field with ν degrees of freedom, scale factor β, and with mean value $G = u$. Thus, its marginal distribution is the known t probability density function:

$$p_Y(h; G = u) = \frac{\Gamma\left(\frac{\nu+1}{2}\right)}{\beta\sqrt{\pi\nu}\Gamma\left(\frac{\nu}{2}\right)}\left(1 + \frac{(h-u)^2}{\beta^2\nu}\right)^{-\frac{\nu+1}{2}} \tag{4.6}$$

Let $\boldsymbol{D} = \boldsymbol{\Lambda}_G + \beta^2\nu(1 + (h-u)^2/\beta^2\nu)^2 W^{-1}\boldsymbol{\Lambda}$, the probability density function of $\tilde{\dot{\boldsymbol{Y}}}$ at zero conditioning on $Y = h$, $G = u$, and W is:

$$p_{\tilde{\dot{\boldsymbol{Y}}}}(\boldsymbol{0}; Y = h, G = u, W) = (2\pi)^{-\frac{j-1}{2}}\det(\tilde{\boldsymbol{D}})^{-\frac{1}{2}} \tag{4.7}$$

where $\tilde{\boldsymbol{D}}$ is the $(j-1)\times(j-1)$ sub-matrix of $\boldsymbol{D}$.
Furthermore, $\ddot{\boldsymbol{Y}}_{|j-1}$ and $\dot{Y}_j$ are independent, so one can write:

$$\begin{aligned}&\mathbb{E}\left[(\dot{Y}_j^+)\det(\ddot{\boldsymbol{Y}}_{|j-1})|\tilde{\dot{\boldsymbol{Y}}} = \boldsymbol{0}, Y = h, G = u, W\right] = \\ &\mathbb{E}\left[(\dot{Y}_j^+)|\tilde{\dot{\boldsymbol{Y}}} = \boldsymbol{0}, Y = h, G = u, W\right] \times \mathbb{E}\left[\det(\ddot{\boldsymbol{Y}}_{|j-1})|\tilde{\dot{\boldsymbol{Y}}} = \boldsymbol{0}, Y = h, G = u, W\right]\end{aligned} \tag{4.8}$$

Conditioning on $\tilde{\dot{\boldsymbol{Y}}} = \boldsymbol{0}$, i.e., $(\dot{Y}_1 = 0, ..., \dot{Y}_{j-1} = 0)$, then the first $(j-1)$ components of z_1 and z_2 will be zeros since $\boldsymbol{z_1}$ and $\boldsymbol{z_2}$ are independent. Hence, one can write by also conditioning on $Y = h$, $G = u$, and W:

$$\mathbb{E}\left[(\dot{Y}_j^+)|\tilde{\dot{\boldsymbol{Y}}} = \boldsymbol{0}, Y = h, G = u, W\right] = (2\pi)^{-\frac{1}{2}}\left(\lambda_{G_j} + \beta^2\nu\left(1 + \frac{(h-u)^2}{\beta^2\nu}\right)^2 W^{-1}\lambda_j\right)^{\frac{1}{2}} \tag{4.9}$$

where λ_{G_j}, λ_j are the $j-$th elements of the matrix $\boldsymbol{\Lambda}_G, \boldsymbol{\Lambda}$, respectively, and due to isotropy one can write $\lambda_{G_j} = \lambda_G$ and $\lambda = \lambda_j$.
and

$$\mathbb{E}\left[(\ddot{Y}_{|j-1})|\tilde{\dot{\boldsymbol{Y}}} = \boldsymbol{0}, Y = h, G = u, W\right] = \mathbb{E}\left[\det\left(\boldsymbol{A} + a\tilde{\boldsymbol{Q}} + b\tilde{\boldsymbol{H}}\right)\right] \tag{4.10}$$

where $a = -(h-u)(1 + (h-u)^2/\beta^2\nu)W^{-1}$, $b = \beta\nu^{1/2}(1 + (h-u)^2/\beta^2\nu)W^{-1/2}$, $\boldsymbol{A} = (-u\tilde{\boldsymbol{\Lambda}}_G + \tilde{\boldsymbol{V}})$, $\tilde{\boldsymbol{\Lambda}}_G, \tilde{\boldsymbol{\Lambda}}$ are the $(j-1)\times(j-1)$ matrix of the first $(j-1)$ rows and columns of $\boldsymbol{\Lambda}_G$ and $\boldsymbol{\Lambda}$, respectively, $\tilde{\boldsymbol{V}} \sim Normal_{(j-1)\times(j-1)}(0, \boldsymbol{M(\tilde{\Lambda}_G)})$, $\tilde{\boldsymbol{H}} \sim Normal_{(j-1)\times(j-1)}(0, \boldsymbol{M(\tilde{\Lambda})})$, and $\tilde{\boldsymbol{Q}} \sim Wishartl_{j-1}(\tilde{\boldsymbol{\Lambda}}, \nu-1)$.

Let consider $\boldsymbol{B}$ a $(j-1)\times(j-1)$ orthogonal matrix which diagonalises $\tilde{\Lambda}$, such that $\boldsymbol{B^t}\tilde{\boldsymbol{\Lambda}}\boldsymbol{B} = \boldsymbol{I}_{j-1}$, then:

$$\begin{aligned}\mathbb{E}\left[\det(\ddot{\boldsymbol{Y}}_{|j-1})|\tilde{\dot{\boldsymbol{Y}}} = \boldsymbol{0}, Y = h, G = u, W\right] &= \det(\tilde{\boldsymbol{\Lambda}})\mathbb{E}[\det(\boldsymbol{B^t}(\tilde{\boldsymbol{A}} + a\tilde{\boldsymbol{Q}} + b\tilde{\boldsymbol{H}})\boldsymbol{B})] \\ &= \det(\tilde{\boldsymbol{\Lambda}})\mathbb{E}[\det(\boldsymbol{A^\star} + a\boldsymbol{Q^\star} + b\boldsymbol{H^\star})]\end{aligned}$$

where $\boldsymbol{A^\star} = \boldsymbol{B^t}\tilde{\boldsymbol{A}}\boldsymbol{B}$, $\boldsymbol{Q^\star} = \boldsymbol{B^t}\tilde{\boldsymbol{Q}}\boldsymbol{B} \sim Wishart_{j-1}(\boldsymbol{I}_{j-1}, \nu - 1)$, and $\boldsymbol{H^\star} = \boldsymbol{B^t}\tilde{\boldsymbol{H}}\boldsymbol{B} \sim Normal_{(j-1)\times(j-1)}(0, \boldsymbol{M(I)})$.

Using Lemma A.0.6 in Appendix A, we obtain:

$$\begin{aligned}&\mathbb{E}\left[\det(\ddot{\boldsymbol{Y}}_{|j-1})|\tilde{\dot{\boldsymbol{Y}}} = \boldsymbol{0}, Y = h, G = u, W\right] = \det(\tilde{\boldsymbol{\Lambda}})\\ &\sum_{n=0}^{\lfloor\frac{j-1}{2}\rfloor}\sum_{k=0}^{j-1-2n}\binom{\nu-1}{k}\frac{(-1)^n(2n+k)!}{2^n n!}b^{2n}\mathbb{E}(\mathrm{detr}_{j-1-2n-k}(\boldsymbol{A^\star}))\end{aligned} \tag{4.11}$$

where $\mathrm{detr}_l(\boldsymbol{A^\star})$, $(l = j-1-2n-k)$, is the sum of the determinants of all $l \times l$ principal minors of $\boldsymbol{A^\star}$. Let $\boldsymbol{C} = \boldsymbol{B^t}\tilde{\Lambda}_G\boldsymbol{B}$, such that $\boldsymbol{A^\star} = -u\boldsymbol{C} + \boldsymbol{K}$, where $\boldsymbol{K} \sim Normal_{(j-1)\times(j-1)}(0, \boldsymbol{M(C)})$, and let $\boldsymbol{L}$ be an orthogonal matrix such that $\boldsymbol{L^t C L} = \boldsymbol{I}_{j-1}$, then:

$$\mathbb{E}(\mathrm{detr}_l(\boldsymbol{A^\star})) = \binom{j-1}{l}\det(\boldsymbol{C}_{|l})\mathbb{E}(\det(-u\boldsymbol{I_l} + \boldsymbol{K^\star}_{|l})) \tag{4.12}$$

where $\boldsymbol{K^\star} \sim Normal_{(j-1)\times(j-1)}(0, \boldsymbol{M(I)})$, and the notation $|l$ represents the submatrix composed of the $l \times l$ components.
Since, the distribution of any $l \times l$ principal minor of $\boldsymbol{K^\star}$ is $Normal_{l\times l}(0, \boldsymbol{M(I)})$, then using Lemma A.0.4, and using the fact that the determinant $\det(\boldsymbol{B}) = \det(\tilde{\boldsymbol{\Lambda}})^{-1/2}$ we have:

$$\mathbb{E}(\mathrm{detr}_l(\boldsymbol{A^\star})) = \det(\tilde{\Lambda}_{|l}^{-1})\det(\tilde{\Lambda}_{G_{|l}})\binom{j-1}{l}\sum_{m=0}^{\lfloor\frac{l}{2}\rfloor}\frac{(-1)^{l-m}(2m)!}{2^m m!}u^{l-2m} \tag{4.13}$$

Putting equations (4.13) and (4.11) together yields:

$$\begin{aligned}&\mathbb{E}\left[\det(\ddot{\boldsymbol{Y}}_{|j-1})|\tilde{\dot{\boldsymbol{Y}}} = \boldsymbol{0}, Y = h, G = u, W\right] = \det(\tilde{\boldsymbol{\Lambda}})\times\\ &\sum_{n=0}^{\lfloor\frac{j-1}{2}\rfloor}\sum_{k=0}^{j-1-2n}\binom{j-1}{j-1-2n-k}\binom{\nu-1}{k}\beta^{2n}\nu^n(h-u)^k\left(1+\frac{(h-u)^2}{\beta^2\nu}\right)^{2n+k}W^{-(n+k)}\\ &\times\det(\tilde{\boldsymbol{\Lambda}}_{|j-1-2n-k}^{-1})\det(\tilde{\boldsymbol{\Lambda}}_{G_{|j-1-2n-k}})\sum_{m=0}^{\lfloor\frac{j-1-2n-k}{2}\rfloor}\frac{(-1)^{j-1-n-m}(2n+k)!(2m)!}{2^{n+m}n!m!}u^{j-2n-k-2m-1}\end{aligned} \tag{4.14}$$

Hence:

$$\mathbb{E}\left[(\dot{Y}_j^+)\det(\ddot{\boldsymbol{Y}}_{|j-1})|\tilde{\dot{\boldsymbol{Y}}}=\boldsymbol{0},Y=h,G=u,W\right]p_{\tilde{\dot{\boldsymbol{Y}}}}(\boldsymbol{0};h,u,W)=$$
$$(2\pi)^{-\frac{j}{2}}\lambda_G^{j-1}\left(\lambda_G+\lambda\beta^2\nu(1+(h-u)^2/\beta^2\nu)^2W^{-1}\right)^{-\frac{j}{2}+1}$$
$$\sum_{n=0}^{\lfloor\frac{j-1}{2}\rfloor}\sum_{k=0}^{j-1-2n}\binom{\nu-1}{k}\binom{j-1}{j-1-2n-k}\beta^{2n}\nu^n(h-u)^k\left(1+\frac{(h-u)^2}{\beta^2\nu}\right)^{2n+k}\left(\frac{\lambda_G}{\lambda}\right)^{-(2n+k)}$$
$$\times\sum_{m=0}^{\lfloor\frac{j-1-2n-k}{2}\rfloor}\frac{(-1)^{j-1-n-m}(2n+k)!(2m)!}{2^{n+m}n!m!}W^{-(n+k)}u^{j-2n-k-2m-1} \tag{4.15}$$

where $\tilde{\boldsymbol{\Lambda}}_G=\lambda_G\boldsymbol{I}_{j-1}$, $\tilde{\boldsymbol{\Lambda}}=\lambda\boldsymbol{I}_{j-1}$ due to isotropy.
Since $W\sim\chi^2_{\nu+1}$, and the moment $\mathbb{E}(W^k)$ are given by:

$$\mathbb{E}[W^k]=2^k\frac{\Gamma((\nu+1)/2+k)}{\Gamma((\nu+1)/2)} \tag{4.16}$$

Then by applying the expectation over W, and multiplying by the probability density function of Y conditioning on G, then integrating over the probability density function of G, we obtain the results for $\rho_2(h)$ and $\rho_1(h)$.
Finally, for $j=0$, $\rho_0(h)=\mathbb{P}[Y\geqslant h]$ which given the result in (i) of theorem 4.4.1. □

4.5 The extreme values of the Gaussian$-t$ random field

Corollary 4.5.1. *The expected Euler-Poincaré characteristic of the two-dimensional excursion set, $E_h(Y,S)$, at high levels h, $(h\to\infty)$, where it does not touch the boundaries of S, is:*

$$\mathbb{E}[\chi(E_h(Y,S))]=Area(S)\frac{2^{\frac{1}{2}}\lambda\Gamma\left(\frac{\nu+1}{2}\right)}{(2\pi)^2\Gamma\left(\frac{\nu}{2}\right)}\int_{-\infty}^{\infty}\frac{(h-u)}{\beta\sqrt{\nu}}\left(1+\frac{(h-u)^2}{\beta^2\nu}\right)^{-\frac{\nu-1}{2}}e^{-u^2/2}du$$
$$+Area(S)\frac{\lambda_G\Gamma\left(\frac{\nu+1}{2}\right)}{(2\pi)^2\Gamma\left(\frac{\nu}{2}\right)\beta\sqrt{\nu/2}}\int_{-\infty}^{\infty}u\left(1+\frac{(h-u)^2}{\beta^2\nu}\right)^{-\frac{\nu+1}{2}}e^{-u^2/2}du \tag{4.17}$$

Corollary 4.5.2. *Let $Y_{max}=sup\{Y(\boldsymbol{x}):\boldsymbol{x}\in S\}$. Then, for $\nu>2$, and $h\to\infty$*

$$\mathbb{P}(Y_{max}\geq h)\to Area(S)\frac{2^{\frac{1}{2}}\lambda\beta^{\nu-2}\nu^{\frac{\nu-2}{2}}\Gamma\left(\frac{\nu+1}{2}\right)}{(2\pi)^{\frac{3}{2}}\Gamma\left(\frac{\nu}{2}\right)}h^{-(\nu-2)},\quad if\,\beta>0$$
$$\mathbb{P}(Y_{max}\geq h)\to Area(S)\frac{\lambda_G}{(2\pi)^{\frac{3}{2}}}\times he^{-\frac{h^2}{2}},\quad if\,\beta\to 0 \tag{4.18}$$

Proof. From [Has78] and [Adl81], we have

$$\mathbb{P}(Y_{max} \geq h) = \mathbb{P}(M_h^+(Y,S)) \approx \mathbb{E}[\chi(E_h(Y,S))] \tag{4.19}$$

when $h \to \infty$. Where $M_h^+(Y,S)$ denotes the number of the local maxima of $Y(x)$ above h inside S. Then, the first result can be obtained immediately from equation (4.17). Whereas, the second result is obtained from replacing $(h-u)/\beta$, equation (4.17), by a variable y, then, letting $\beta \to 0$ when $h \to \infty$. □

4.6 The expected intrinsic volumes of the GT_β^ν excursion sets over rectangles of $\mathbb{R}^2$

Let $S = [0,a]^2$, where a is the one side length of S, then for an isotropic stationary centered real-valued Gaussian$-t$ random field, $Y(\boldsymbol{x})$, the expected intrinsic volumes, which are in this case Minkwoski functionals, of its excursion set, $E_h(Y,[0,a]^2)$, at a given level h, using the general formula in equation (3.18), chapter 3 are:

1. $\mathbb{E}(Ar(h)) = \rho_0(h)$: the mean area function of $E_h(Y,[0,a]^2)$
2. $\mathbb{E}(Cr(h)) = 2a\rho_1(h) + \rho_0(h)$: half the mean contour length of $E_h(Y,[0,a]^2)$
3. $\mathbb{E}(\chi(h)) = a^2\rho_2(h) + 2a\rho_1(h) + \rho_0(h)$: the mean Euler-Poincaré characteristic of $E_h(Y,[0,a]^2)$

where $\mathcal{L}_0([0,a]^2) = 1$, $\mathcal{L}_1([0,a]^2) = 2a$, and $\mathcal{L}_2([0,a]^2) = a^2$.

4.7 Simulation Results

In order to represent the previous formulae in theorem 4.4.1, simulation results are illustrated in this section. A set of 100 two-dimensional realizations of the GT_β^ν random fields are generated on a rectangle $[0,1]^2$ with a resolution $n = 512 \times 512$ pixels. Each random realization is supposed to be a linear mixture of a two-dimensional homogeneous Gaussian random field with covariance matrix $\boldsymbol{\Sigma}_G = \sigma_G^2 \boldsymbol{I}_2$, such that $\sigma_G = 11$ pixels, and a two-dimensional $t-$field with 5 degrees of freedom, and with scale factor $\beta = 0.2$, at each pixel, (see one representative result in Fig. 4.1). The 100 realizations of the t random fields in the aforementioned example are generated each one using 6 (i.i.d) homogeneous Gaussian random fields with covariance matrix $\boldsymbol{\Sigma} = \sigma^2 \boldsymbol{I}_2$, such that $\sigma = 3$ pixels. Then, the mean Minkowski functionals, including the expected Euler-Poincaré characteristic, are estimated from the 100 simulations and they are compared to the mean ones given analytically, (see Fig. 4.2). The results show a good approximation between the simulated and the theoretical Minkowski functionals.

Now, we will focus on illustrating the influence of the scale factor β on the expected Euler-Poincaré characteristic at the high thresholds, where it estimates

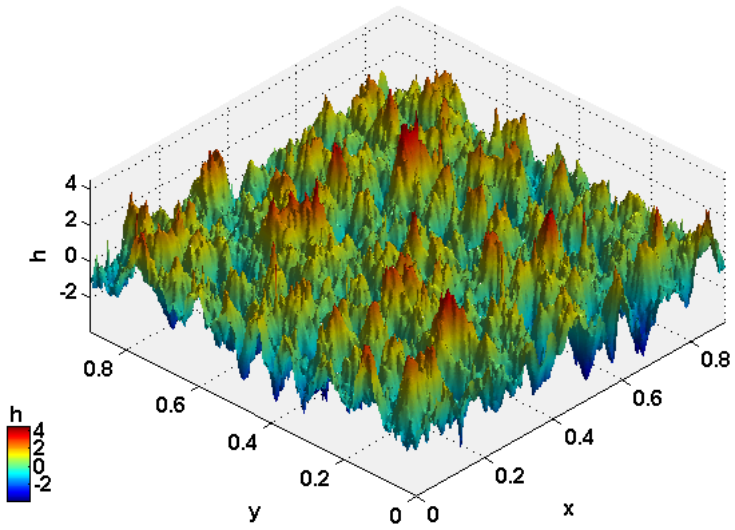

Figure 4.1: An exemplary illustration of a two-dimensional GT^{ν}_{β} random field generated from the linear mixture of a Gaussian RF and a student's t one with 5 degrees of freedom and with $\beta = 0.2$.

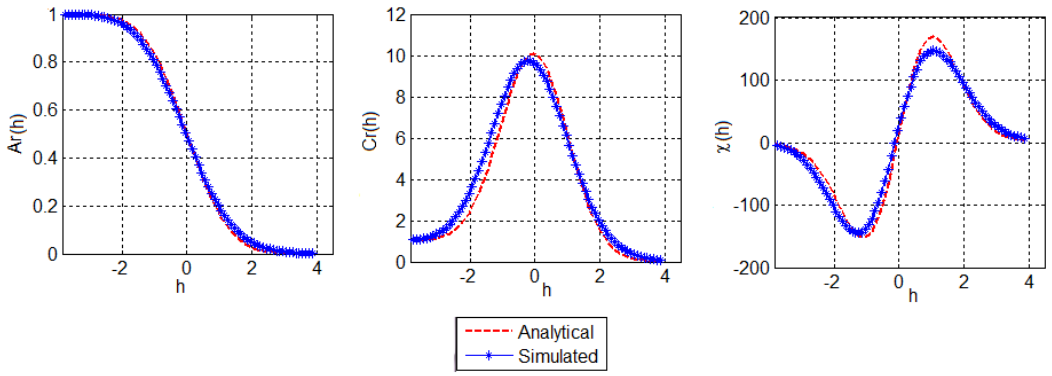

Figure 4.2: Fitting the analytical and the simulated mean Minkowski functionals of 100 realizations of the $GT^{5}_{0.2}$ RFs.

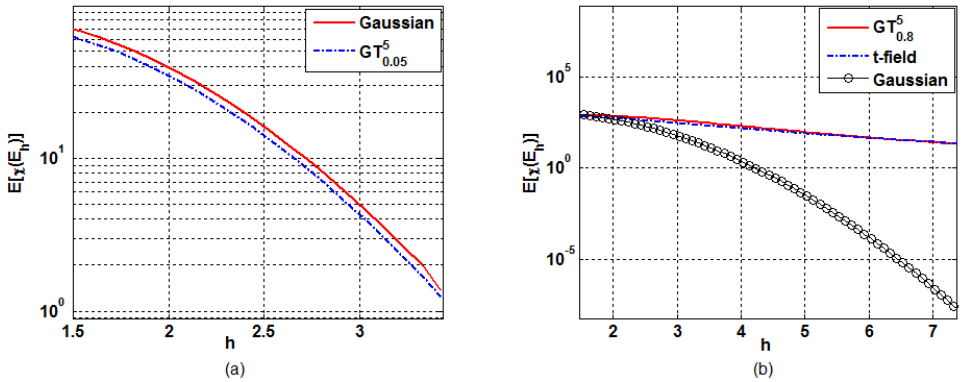

Figure 4.3: Comparing the expected Euler-Poincaré characteristic, $\mathbb{E}[\chi(E_h)]$, of the GT^{ν}_{β} excursion sets to the Gaussian one for $\beta = 0.05$, $\beta = 0.8$, respectively, and $\nu = 5$ degrees of freedom. In the second example (right plot), the $\mathbb{E}[\chi(E_h)]$ for the $GT^{5}_{0.8}$ is also compared to the theoretical one for the $t-$field of 5 degrees of freedom.

the extrema of Y, for $0 < \beta < 1$. Toward this aim, two simulation examples are generated using the same parameters with different values of β, $(\beta = 0.05, 0.8)$. The analytical upper tail probability of Y, $\mathbb{P}[Y_{max} \geq h]$, in both examples is compared to the one, $\mathbb{P}[G_{max} \geq h]$, of the Gaussian random field, (see Fig. 4.3), given analytically by [Adl81]:

$$\mathbb{P}[G_{max} \geq h] \approx \mathbb{E}[\chi(E_h(G,h))] = Area(S)\lambda_G h e^{-h^2/2}/(2\pi)^{3/2}$$

In the second example, we also compared the upper tail probability of Y to the one of a $t-$field, [Wor94], with same degrees of freedom and $\beta = 0.8$.
Fig. 4.3 shows that $\beta = 0.05$ the number of the local maxima of the GT^{ν}_{β} random field, Y, approximates the one of the Gaussian random field. Whereas, for $\beta = 0.8$, the number of the extreme values of Y are close to the one of $t-$field. However, the size of the isolated clusters will change,(see Fig.**??**) as example. Several simulation examples are done for different values of β in the interval $[0, 1]$. The results show that when $\beta < 0.1$, the number of the maxima of Y is always close to the number of the Gaussian maxima, whereas when $\beta \geq 0.5$ they approximate the number of the $t-$field maxima.

4.8 Conclusion

A stationary Gaussian$-t$ random field is defined, in this chapter, from the linear mixture of independent Gaussian and scaled t random fields. The expected EC densities are given analytically for the two-dimensional excursion sets. The EC densities are used to estimate the intrinsic volumes including the Euler-Poincaré characteristics of the isotropic, centred Gaussian$-t$ random fields defined on two-dimensional rectangles of the Euclidean space. Simulation examples are investigated

in order to illustrate the analytical expectations with the numerical one computed from the simulation examples. Furthermore, the simulations are used to illustrate the influence of the scale factor β of the $t-$field on the behaviour of the Gaussian$-t$ random field near the global maxima, and demonstrated what expected theoretically. The results showed that the expected number of the maximas of the GT_{β}^{ν} random field approximates the number of the maximas of the $t-$field. However, when $\beta \to 0$, the GT_{β}^{ν} behaves differently and the number of its extreme values converges to the number of the ones of Gaussian random fields. The motivation of this chapter could be seen in the application part (see Part IV).

Chapter 5

Skew$-t$ random fields

Contents

5.1 Introduction 49
5.2 Representation of skew$-t$ distribution 49
5.2.1 Univariate skew$-t$ distribution 50
5.2.2 Multivariate skew$-t$ distribution 50
5.3 Skew student's t random field 51
5.3.1 Definition 51
5.3.2 Representation of derivatives 52
5.4 The EC densities of the skew$-t$ excursion sets 54
5.5 The extreme values of the skew$-t$ random field 57
5.6 Simulation results on two-dimensional rectangles 58
5.7 Conclusion 59

5.1 Introduction

In this chapter, we present a class of skew random fields, namely skew student's t (or skew$-t$) random fields. The new theoretical results given in this chapter, published in [AP13b, AP13c], are concerned about the geometric quantifiers of the excursion sets of the skew$-t$ random fields, i.e.; the mean intrinsic volumes (Lipschitz-Killing curvatures) and the EC densities in both $\mathbb{R}^2$ and $\mathbb{R}^3$. The definition of the skew$-t$ random field is based on the stochastic representation of its multivariate distribution given by [AC03].

5.2 Representation of skew$-t$ distribution

Before tackling the skew$-t$ random fields, and the geometry of there excursion sets, this section reviews the skew$-t$ distribution, since it will be used later in this chapter. The skew$-t$ distribution arises as an extension of the student's t distribution family, and it has been defined in the literature by different ways, [AC03, Gen04, Jon08, BLCG10], each associated with skewing the symmetric t distribution in order to make it more useful for empirical stochastic modelling. We will focus, in this thesis, on the nicest type of the skew$-t$ family that is based on the skew-normal distribution, related to [AC99, AC03] and also cited in [Jon08, LLBG10, BLCG10, CLP12].

5.2.1 Univariate skew$-t$ distribution

A real-valued random variable Y is said to have a univariate skew$-t$ distribution, of type [AC03], with ν degrees of freedom, and skewness parameter $\alpha \in \mathbb{R}$ if its probability density function is given by:

$$f_Y(y;\alpha,\nu) = \frac{2}{\sigma_Y} t_1(h;\nu) T_1\left(\alpha h \sqrt{\frac{\nu+1}{\nu+h^2}}; \nu+1\right), \quad h = (y-\mu_Y)/\sigma_Y, \quad y \in \mathbb{R} \tag{5.1}$$

where $\mu_Y \in \mathbb{R}$ is the mean of Y, $\sigma_Y > 0$ is the standard deviation of Y, $t_1(.;\nu)$ is the standard student's t distribution with ν degrees of freedom, and T_1 is the student's t cumulative distribution function with $\nu+1$ degrees of freedom at $\alpha h\sqrt{\frac{\nu+1}{\nu+h^2}}$ The real parameter α conflates its skewing role with alternation of the weight of one of the two density tails. For $\alpha > 0$ (resp. $\alpha < 0$) the probability density function has a positive (resp. negative) skewness, so the right (resp. left) tail will be longer. When $\alpha = 0$ the skew$-t$ probability density is the known student's t distribution.

The stochastic representation of Y that has the probability density function defined in (5.1), is given by:

$$Y = \mu_Y + \sigma_Y V^{-1/2}\left(\delta|Z| + \sqrt{1-\delta^2}G\right) \tag{5.2}$$

where $\nu V \sim \chi^2_\nu$, $z, G \sim Normal(0,1)$ are all independent random variables, and $\delta = \alpha/\sqrt{1+\alpha^2}$ [AC99]. So, Y in Eq. (5.2) will be written such that $Y \sim St_{(\nu;\alpha)}$.

5.2.2 Multivariate skew$-t$ distribution

An $\mathbb{R}^d$-valued random variable [1] $\mathbf{Y} = (Y_1, ..., Y_d)^t$ is said to have a multivariate skew$-t$ distribution with ν degrees of freedom, and skewness $\boldsymbol{\alpha} \in \mathbb{R}^d$ if, for a mean vector $\boldsymbol{\mu_Y} \in \mathbb{R}^d$ and a non-negative definite $d \times d$ covariance matrix Σ, the probability density function of $\mathbf{Y}$ can be expressed as follows:

$$f_{\mathbf{Y}}(\mathbf{y}) = 2t_d(\mathbf{y};\nu) T_1\left(\boldsymbol{\alpha}^t(\mathbf{y}-\boldsymbol{\mu_Y})\left(\frac{\nu+d}{\nu+\mathbf{h}^t\mathbf{h}}\right)^{1/2}; \nu+d\right), \quad \mathbf{y} \in \mathbb{R}^d \tag{5.3}$$

where $\mathbf{h} = \Sigma^{-1/2}(\boldsymbol{y} - \boldsymbol{\mu_Y})$, $t_p(.;\nu)$ is the pdf of the d-dimensional t variate with ν degrees of freedom, and $T_1(.;\nu+d)$ is the scalar t cumulative distribution with $\nu+d$ degrees of freedom.

Example 5.2.1. *For $d = 2$, (see Fig. 5.1), $\boldsymbol{Y} = (Y_1, Y_2)^t$. Setting $\boldsymbol{\mu_Y} = 0$, the pdf of the bivariate skew$-t$ random variable $\boldsymbol{Y}$ is:*

$$f_{\boldsymbol{Y}}(y_1, y_2) = 2t_2(y_1, y_2;\nu) T_1\left(q(\alpha_1 y_1 + \alpha_2 y_2); \nu+2\right) \tag{5.4}$$

where $q = \sqrt{(\nu+2)/(\nu + \boldsymbol{y}^t\boldsymbol{\Sigma}^{-1}\boldsymbol{y})}$, and $\boldsymbol{\Sigma} = \begin{bmatrix} \sigma_1^2 & \sigma_1\sigma_2 \\ \sigma_2\sigma_1 & \sigma_2^2 \end{bmatrix}$

1. The vectors in all chapters are represented as row vectors and the notation Y^t indicates the vector transpose of Y

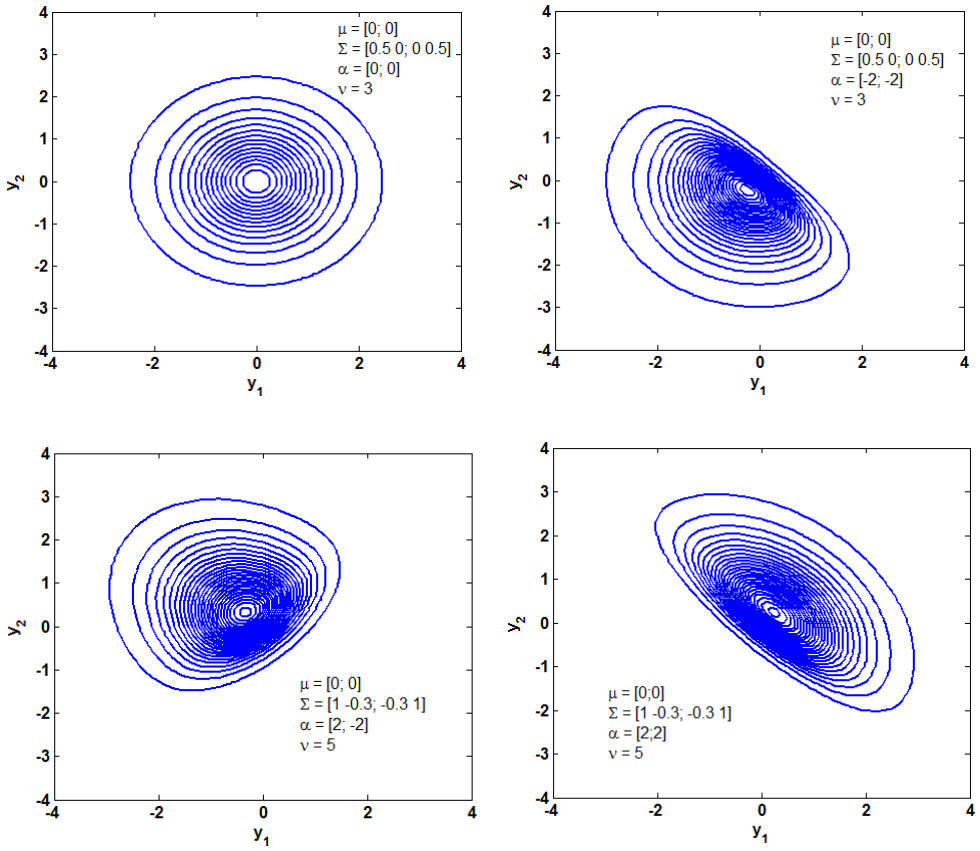

Figure 5.1: Three illustrations of the contour plot of the bivariate skew$-t$ pdf. (a) $\alpha = 0$, $\mathbf{\Sigma} = 0.5I_2$, $\nu = 3$, the skew$-t$ bivariate pdf is equivalent to the symmetric bivariate t pdf. (b) $\alpha = (-2; -2)$, $\Sigma = 0.5I_2$, $\nu = 3$. (c) $\alpha = (2; -2)$, $\Sigma = (1, -0.3; -0.3, 1)$, $\nu = 5$. (d) $\alpha = (2; 2)$, $\Sigma = (1, -0.3; -0.3, 1)$, $\nu = 5$

5.3 Skew student's t random field

Let $\{Y = Y(\boldsymbol{x}) : \boldsymbol{x} \in S\}$ be a real-valued smooth random field defined on a non-empty compact subset $S \subset \mathbb{R}^N$. Let $\dot{\boldsymbol{Y}} = \partial Y(\boldsymbol{x})/\partial \boldsymbol{x}$ and $\ddot{\boldsymbol{Y}} = \partial^2 Y(\boldsymbol{x})/\partial \boldsymbol{x}\partial \boldsymbol{x}^t$ be the gradient $N-$vector and the $N \times N$ Hessian matrix of Y, respectively. This section will concern about the stochastic representation of Y and its derivatives on $\mathbb{R}^N$ assuming that Y is a real-valued skew$-t$ random field.

5.3.1 Definition

Let $G_0(\boldsymbol{x}), ..., G_\nu(\boldsymbol{x})$, $\boldsymbol{x} \in S$, be a i.i.d, homogeneous, real-valued Gaussian random fields with zero mean, unit variance, and with second order-spectral moment matrix $\Lambda = \mathrm{Var}(\partial G_i/\partial \boldsymbol{x})$, $i = 0, ..., \nu$. Let Z be a $Normal(0, 1)$ random variable independent of all G_i, $i = 0, .., \nu$. Then, for a real $\delta \in (-1, 1)$, a skew$-t$ random

field is defined at any fixed point $\boldsymbol{x}$ as follows:

$$Y(\boldsymbol{x}) = \frac{\delta|Z| + \sqrt{1-\delta^2}G_0(\boldsymbol{x})}{\left(\sum_{k=1}^{\nu} G_k^2(\boldsymbol{x})/\nu\right)^{1/2}} \tag{5.5}$$

Notice that the marginal distribution of Y, at any fixed x, is the skew$-t$ distribution with ν degrees of freedom and skewness $\alpha = \delta/\sqrt{1-\delta^2}$.
Again recalling that the $t-$field is well defined when $\nu \geq N$, [Wor94]. Thus, the definition of the skew$-t$ field will be also restricted to the condition $\nu \geq N$ in order to avoid that the numerator and denominator both take the value zero inside a compact set S.

5.3.2 Representation of derivatives

In the following lemma, we extended the representation of the $t-$field derivatives given by [Wor94] to represent $\dot{\boldsymbol{Y}}$ and $\ddot{\boldsymbol{Y}}$ of the skew$-t$ random field Y.

Lemma 5.3.1. *The first and second derivatives of $Y = Y(x)$, at any fixed point $x \in \mathbb{R}^N$, can be expressed in terms of independent random variables, where the equality $\overset{D}{=}$ is equality in law, such that:*

(i) $\dot{\boldsymbol{Y}} \overset{D}{=} \nu^{\frac{1}{2}}(1-\delta^2)^{\frac{1}{2}}\left(1 + Y^2/\nu\left(1-\delta^2\right)\right) W^{-\frac{1}{2}}\boldsymbol{z}$

(ii) $\ddot{\boldsymbol{Y}} \overset{D}{=} \nu^{\frac{1}{2}}(1-\delta^2)^{\frac{1}{2}}\left(1 + Y^2/\nu\left(1-\delta^2\right)\right) W^{-1}\Big\{-\nu^{-1/2}\left(1-\delta^2\right)^{-1/2} Y(\boldsymbol{P} - 2\boldsymbol{z}_1\boldsymbol{z}_1^t)$
$-\boldsymbol{z}_2\boldsymbol{z}_1^t - \boldsymbol{z}_1\boldsymbol{z}_2^t + \alpha|Z|\left(1 + Y^2/\nu\left(1-\delta^2\right)\right)^{-1/2} W^{1/2}\boldsymbol{\Lambda} + W^{1/2}\boldsymbol{H}\Big\}$

where $\delta = \alpha/\sqrt{1+\alpha^2}$, $Z \sim Normal_1(0,1)$, $Y \sim St_{(\nu;\alpha)}$, $\boldsymbol{z}, \boldsymbol{z}_1, \boldsymbol{z}_2 \sim Normal_N(0, \boldsymbol{\Lambda})$, $\boldsymbol{P} \sim Wishart_N(\boldsymbol{\Lambda}, \nu - 1)$, $W \sim \chi^2_{\nu+1}(\alpha^2)$, $\boldsymbol{H} \sim Normal_{N\times N}(0, \boldsymbol{M}(\boldsymbol{\Lambda}))$, are all independent.

Proof. First, let define $V = V(\boldsymbol{x})$ such that $V = \sum_{k=1}^{\nu} G_k^2$, then, the marginal distribution for V, at any fixed point $x \in S$, is the χ^2_ν distribution with ν degrees of freedom. We shall use the notation $F = \nu^{-1/2}\left(1-\delta^2\right)^{-1/2} Y$ to simplify the algebraic operations. So, $F = V^{-1/2}(\alpha|Z| + G)$, where V is a χ^2 field with ν degrees of freedom, G is a Gaussian random field, and $Z \sim Normal_1(0,1)$ is a normal random variable, all are independent.

Let consider $W = V + (\alpha|Z| + G)^2$. Then, conditional on Z, W has a non-central $\chi^2_{\nu+1}$ marginal distribution with $\nu+1$ degrees of freedom and with non-centrality parameter $(\alpha^2 Z^2)$. Since Z is a standard normal random variable with unit variance, then, the unconditional distribution of W is the $\chi^2_{\nu+1}$ distribution with non-centrality parameter α^2, i.e.; $W \sim \chi^2_{\nu+1}(\alpha^2)$.

The first derivative of F is given by:

$$\dot{\boldsymbol{F}} = -\frac{1}{2}\left(\alpha|Z| + G\right) V^{-3/2}\dot{\boldsymbol{V}} + V^{-1/2}\dot{\boldsymbol{G}} \tag{5.6}$$

where Z is independent of $\boldsymbol{x} \in S$. Recalling the representation of the first and second χ^2 derivatives derived in [Wor94], and the derivatives for the Gaussian random field derived in [Adl81], (see Appendix A). The last equation can be written such that:

$$\dot{\boldsymbol{F}} = V^{-1}\left[V^{1/2}\boldsymbol{z}_2 - (\alpha|Z| + G)\,\boldsymbol{z}_1\right] \tag{5.7}$$

where $\boldsymbol{z}_1, \boldsymbol{z}_2 \sim Normal_N(0, \boldsymbol{\Lambda})$ and are independent.
Let suppose $\boldsymbol{z}$ such that

$$\boldsymbol{z} = W^{-1/2}\left[V^{1/2}\boldsymbol{z}_2 - (\alpha|Z| + G)\,\boldsymbol{z}_1\right] \tag{5.8}$$

then, $\boldsymbol{z} \sim Normal_N(0, \boldsymbol{\Lambda})$. On the other hand, we have:

$$V = \frac{W}{1+F^2}; \quad \text{and} \quad G = \frac{WF^2}{1+F^2} - \alpha|Z| \tag{5.9}$$

Replacing F by Y, and putting equations (5.8), (5.9) in (5.7) ends the proof of (i).

For the second derivative $\ddot{\boldsymbol{F}}$ we have:

$$\begin{aligned}\frac{\boldsymbol{\partial^2 F}}{\boldsymbol{\partial x \partial x}^t} = &\frac{3}{4}(\alpha|Z| + G)V^{-5/2}\frac{\boldsymbol{\partial V}}{\boldsymbol{\partial x}}\frac{\boldsymbol{\partial V}}{\boldsymbol{\partial x}^t} - \frac{1}{2}V^{-3/2}\left[\frac{\boldsymbol{\partial V}}{\boldsymbol{\partial x}}\frac{\boldsymbol{\partial G}}{\boldsymbol{\partial x}^t} + \frac{\boldsymbol{\partial G}}{\boldsymbol{\partial x}}\frac{\boldsymbol{\partial V}}{\boldsymbol{\partial x}^t}\right] \\ &- \frac{1}{2}(\alpha|Z| + G)V^{-3/2}\frac{\boldsymbol{\partial^2 V}}{\boldsymbol{\partial x \partial x}^t} + V^{-1/2}\frac{\boldsymbol{\partial^2 G}}{\boldsymbol{\partial x \partial x}^t}\end{aligned}$$

By replacing the second derivative of the χ^2 field, V, and the Gaussian field, G, (see Appendix A), we have:

$$\begin{aligned}\frac{\boldsymbol{\partial^2 F}}{\boldsymbol{\partial x \partial x}^t} = V^{-1}\Big(&-F(\boldsymbol{P} - 2\boldsymbol{z}_1\boldsymbol{z}_1^t) - \boldsymbol{z}_1\boldsymbol{z}_2^t - \boldsymbol{z}_2\boldsymbol{z}_1^t + \alpha|Z|V^{1/2}\boldsymbol{\Lambda} + \Big[V^{1/2}\boldsymbol{H}_2 - \\ &(\alpha|Z| + G)\boldsymbol{H}_1\Big]\Big)\end{aligned} \tag{5.10}$$

where $\boldsymbol{H}_1, \boldsymbol{H}_2 \sim Normal_{N\times N}(0, \boldsymbol{M(\Lambda)})$, and $\boldsymbol{P} \sim Wishart_N(\boldsymbol{\Lambda}, \nu - 1)$.

Notice that $\boldsymbol{H}_1$ and $\boldsymbol{H}_2$ are independent, so letting $\boldsymbol{H}$ be such that:

$$\boldsymbol{H} = W^{-1/2}\left[V^{1/2}\boldsymbol{H}_1 - (\alpha|Z| + G)\boldsymbol{H}_2\right] \tag{5.11}$$

yields $\boldsymbol{H} \sim Normal_{N\times N}(0, \boldsymbol{M(\Lambda)})$. Putting (5.9) and (5.11) in (5.10) gives the result in (ii), and end the proof of the lemma. □

In the following section, we will assume that the variance-covariance matrix $\boldsymbol{\Lambda} = \boldsymbol{I}_N$ for simplicity, and we will use the derivatives given in 5.3.1 to calculate the EC densities for the isotropic skew$-t$ random fields. The extension to the general case including $\boldsymbol{\Lambda}$, for the stationary skew$-t$ random fields, can then be done by changing the coordinates of the set S such that $\tilde{\boldsymbol{x}} = \boldsymbol{\Lambda}^{1/2}\boldsymbol{x}$. In order to find

the mean Lipschitz-Killing curvatures for the skew$-t$ random fields, we have to assume some regularity conditions on $Y(\boldsymbol{x})$. Since $Y(\boldsymbol{x})$ is based on components of Gaussian random fields by definition, then, it is sufficient that each component satisfies the conditions of theorem to consider Y is suitably regular. This was proved by [Wor94] for F and student's t random fields. Thus, the proof also directly holds for the skew$-t$ random fields following the same arguments given by [Wor94].

5.4 The EC densities of the skew$-t$ excursion sets

Under the assumption that the skew$-t$ random field satisfies the regularity conditions presented by Theorem in chapter 3, the following theorem gives the $j-$th EC densities $\rho_j(h)$ of the skew$-t$ random field, $Y(\boldsymbol{x})$, $\boldsymbol{x} \in S$, where S is a non-empty compact subset of $\mathbb{R}^N$, $(N \leq 3)$.

Theorem 5.4.1. *For $\nu \geq N$, $(N > 1)$, the $j-$th dimensional EC density, $\rho_j(.)$, $(0 < j \leq N)$, of the skew$-t$ random field Y, on $S \subset \mathbb{R}^N$, for a given threshold h is expressed as:*

$$\begin{aligned}\rho_j(h) = (-1)^{j-1}(2\pi)^{-\frac{j+2}{2}}2^{\frac{j+2}{2}}\left(1+\frac{h^2}{\nu}\right)^{-\frac{\nu+1}{2}} T_1\left(\alpha h\sqrt{\frac{\nu+1}{\nu+h^2}};\nu+1\right)\\ \sum_{n=0}^{\lfloor\frac{j-1}{2}\rfloor}\sum_{k=0}^{j-1-2n}\binom{\nu-1}{k}\frac{(-1)^{k+n}(2n+k)!\Gamma\left(\frac{j-2n-k}{2}\right)\Gamma\left(\frac{\nu-k}{2}\right)}{2^{2n+k}n!\Gamma\left(\frac{\nu+1}{2}\right)}\nu^{-\frac{k}{2}}\delta^{j-2n-k-1}\\ (1-\delta^2)^{-\frac{k-2}{2}}h^k\left(1+\frac{h^2}{\nu(1-\delta^2)}\right)^{-\frac{j-2n-k-3}{2}}\end{aligned} \tag{5.12}$$

where $\alpha = \delta/\sqrt{1-\delta^2}$ and $\delta^2 < 1$.

Proof. The theorem extends the results obtained by [Wor94] for the $t-$fields. In this proof, to evaluate the EC densities, we will use Morse theory mentioned in chapter 3, while the expectations will be evaluated by conditioning on Y, W and Z, and then by taking the expectations over W conditional on Z.

Conditional on Z, $W \sim \chi^2_{\nu+1}(\alpha^2 Z^2)$ independent of Y, where $Z \sim Normal_1(0,1)$. So, we $\rho_j(h)$ can be expressed as:

$$\begin{aligned}\rho_j(h) = \frac{(-1)^{j-1}}{(2\pi)^{\frac{1}{2}}}p_Y(h)\\ \int_{-\infty}^{\infty}\mathbb{E}_W\left[\mathbb{E}\left[\dot{Y}^+_{(j)}\det(\ddot{\boldsymbol{Y}}_{|j-1})|\dot{\boldsymbol{Y}}_{|j-1}=0, Y=h, W, Z\right]p_{\dot{\boldsymbol{Y}}_{|j-1}}(\boldsymbol{0};h,W,Z)\right]\\ \times e^{-u^2/2}du\end{aligned} \tag{5.13}$$

where $\dot{\boldsymbol{Y}}_{|j-1} = (\dot{Y}_1, ..., \dot{Y}_{j-1})$, with $j > 0$.
The joint probability density function of the first $(j-1)$ components of $\dot{\boldsymbol{Y}}$ conditional on Y, W, and Z is a Gaussian multivariate density function which has the following expression at zero:

$$p_{\dot{\boldsymbol{Y}}_{|j-1}}(0, ..., 0; h, W, Z) = \left[2\pi\nu(1-\delta^2)\left(1 + \frac{h^2}{\nu(1-\delta^2)}\right)^2 W^{-1}\right]^{-\frac{j-1}{2}} \tag{5.14}$$

The components $\dot{Y}_{(j)}$ and $\ddot{\boldsymbol{Y}}_{|j-1}$ are both independent under the conditional expectations. Thus, the term $\mathbb{E}\left(\dot{Y}^+_{(j)}\det(\ddot{\boldsymbol{Y}}_{|j-1})|\dot{Y}_1 = 0, ..., \dot{Y}_{j-1} = 0, Y = h, W, Z\right)$, in (5.13), can be written as:

$$\begin{aligned}&\mathbb{E}\left(\dot{Y}^+_{(j)}\det(\ddot{\boldsymbol{Y}}_{|j-1})|\dot{Y}_1 = 0, ..., \dot{Y}_{j-1} = 0, Y = h, W, Z\right) = \\ &\mathbb{E}\left(\dot{Y}^+_{(j)}|\dot{\boldsymbol{Y}}_{|j-1} = \boldsymbol{0}, Y = h, W, Z\right)\mathbb{E}\left(\det(\ddot{\boldsymbol{Y}}_{|j-1})|\dot{\boldsymbol{Y}}_{|j-1} = \boldsymbol{0}, Y = h, W, Z\right)\end{aligned} \tag{5.15}$$

Conditioning on $Y = h$, W, and Z, $\dot{\boldsymbol{Y}} = a\boldsymbol{z}$, where $a = \nu^{\frac{1}{2}}(1-\delta^2)^{\frac{1}{2}}(1 + h^2/\nu(1-\delta^2))W^{-1/2}$ and $\boldsymbol{z} \sim Normal_N(0, \boldsymbol{I}_N)$ which yields:

$$\mathbb{E}\left(\dot{\boldsymbol{Y}}^+_{(j)}|\dot{\boldsymbol{Y}}_{|j-1} = \boldsymbol{0}, Y = h, W, Z\right) = a(2\pi)^{-1/2} \tag{5.16}$$

On the other hand, let $A = \nu^{1/2}(1-\delta^2)^{1/2}\alpha|Z|(1 + h^2/\nu(1-\delta^2))^{1/2}W^{-1/2}$, $b = \nu^{1/2}(1-\delta^2)^{1/2}(1 + h^2/\nu(1-\delta^2))W^{-1/2}$, and $c = -h(1 + h^2/\nu(1-\delta^2))W^{-1}$ such that $\ddot{Y}$ can be written as

$$\ddot{\boldsymbol{Y}} = c\left(\boldsymbol{P} + \frac{b}{c}\boldsymbol{H} + \frac{1}{c}A\right) \tag{5.17}$$

Then, using lemmas (A.0.5) and (A.0.6) due to [Wor94], (see appendix A), we get:

$$\begin{aligned}&\mathbb{E}\left(\det(\ddot{\boldsymbol{Y}}_{|j-1})|\dot{\boldsymbol{Y}}_{j-1} = \boldsymbol{0}, Y = h, W, Z\right) = c^{j-1}\mathbb{E}\left[\det{}_{|j-1}\left(\boldsymbol{P} + \frac{b}{c}\boldsymbol{H} + \frac{1}{c}A\right)\right] \\ &= \sum_{n=0}^{\lfloor\frac{j-1}{2}\rfloor}\sum_{k=0}^{j-1-2n}\binom{\nu-1}{k}\frac{(-1)^n(2n+k)!}{2^n n!}b^{2n}c^k A^{j-2n-k-1}\end{aligned} \tag{5.18}$$

Since W is independent of Y, the expectations are computed over W. Notice that conditioning on Z, W is the non-central χ^2 field with $\nu + 1$ degrees of freedom and non-centrality parameter $\alpha^2 Z^2$, which yields to:

$$\mathbb{E}[W^k|Z] \approx 2^k e^{-\frac{\alpha^2 Z^2}{2}}\frac{\Gamma((\nu+1)/2 + k)}{\Gamma((\nu+1)/2)} \tag{5.19}$$

where $Z \sim Normal_1(0,1)$.
which yields to:

$$\mathbb{E}_W\left[\mathbb{E}\left[\dot{\boldsymbol{Y}}^+_{(j)}\det(\ddot{\boldsymbol{Y}}_{|j-1})|\dot{\boldsymbol{Y}}_{|j-1}=0, Y=h, W, Z\right] p_{\dot{\boldsymbol{Y}}_{|j-1}}(0,...,0;h,W,Z)\right] =$$
$$(2\pi)^{-\frac{j}{2}}\nu^{\frac{1}{2}}(1-\delta^2)^{\frac{1}{2}}\sum_{n=0}^{\lfloor\frac{j-1}{2}\rfloor}\sum_{k=0}^{j-2n-1}\binom{\nu-1}{k}\frac{(-1)^{n+k}(2n+k)!\Gamma\left(\frac{\nu-k}{2}\right)}{2^{(2n+k+1)/2}n!\Gamma\left(\frac{\nu+1}{2}\right)}\nu^{-\frac{k}{2}}(1-\delta^2)^{-\frac{k}{2}}$$
$$\left(1+\frac{Y^2}{\nu(1-\delta^2)}\right)^{-\frac{j-2n-k-3}{2}}Y^k\times(\alpha|Z|)^{j-2n-k-1}e^{-\frac{\alpha^2Z^2}{2}} \tag{5.20}$$

Putting the last result in equation (5.13), then integrating over the probability density function of Z, $\phi_Z(.)$, and multiplying by the probability density function of Y:

$$p_Y(h) = 2\frac{\Gamma\left(\frac{\nu+1}{2}\right)}{\sqrt{\nu\pi}\Gamma\left(\frac{\nu}{2}\right)}\left(1+\frac{h^2}{\nu}\right)^{-\frac{\nu+1}{2}}T_1\left(\alpha h\sqrt{\frac{\nu+1}{\nu+h^2}};\nu+1\right), \tag{5.21}$$

gives $\rho_j(h)$, for $j>0$, and ends the proof. □

For $j=0$, $\rho_0(h)=\mathbb{P}[Y\geq h]$, which yields together with theorem 5.4.1 to the following result.

Corollary 5.4.1. *The first four EC densities, $\rho_j(.)$, $j=0,1,2,3$, of the skew−t random field Y, for a given threshold h are:*

(i) $$\rho_0(h) = 2\frac{\Gamma\left(\frac{\nu+1}{2}\right)}{\sqrt{\nu\pi}\Gamma\left(\frac{\nu}{2}\right)}\int_h^\infty\left(1+\frac{y^2}{\nu}\right)^{-\frac{\nu+1}{2}}T_1\left(\alpha y\sqrt{\frac{\nu+1}{y^2+\nu}};\nu+1\right)dy$$

(ii) $$\rho_1(h) = \frac{2}{2\pi}(1-\delta^2)\left(1+\frac{h^2}{\nu(1-\delta^2)}\right)\left(1+\frac{h^2}{\nu}\right)^{-\frac{\nu+1}{2}}T_1\left(\alpha h\sqrt{\frac{\nu+1}{\nu+h^2}};\nu+1\right)$$

(iii) $$\rho_2(h) = \frac{2}{(2\pi)^{3/2}}\frac{(1-\delta^2)^{\frac{1}{2}}\Gamma\left(\frac{\nu+1}{2}\right)}{\left(\frac{\nu}{2}\right)^{\frac{1}{2}}\Gamma\left(\frac{\nu}{2}\right)}h\left(1+\frac{h^2}{\nu(1-\delta^2)}\right)\left(1+\frac{h^2}{\nu}\right)^{-\frac{\nu+1}{2}}$$
$$T_1\left(\alpha h\sqrt{\frac{\nu+1}{\nu+h^2}};\nu+1\right)\left[1-2\delta(1-\delta^2)^{\frac{1}{2}}\frac{\pi^{-\frac{1}{2}}\nu^{\frac{1}{2}}\Gamma\left(\frac{\nu}{2}\right)}{\Gamma\left(\frac{\nu+1}{2}\right)h}\left(1+\frac{h^2}{\nu(1-\delta^2)}\right)^{-\frac{1}{2}}\right]$$

(iv) $$\rho_3(h) = \frac{2}{(2\pi)^2}\left(1+\frac{h^2}{\nu(1-\delta^2)}\right)\left(1+\frac{h^2}{\nu}\right)^{-\frac{\nu+1}{2}}T_1\left(\alpha h\sqrt{\frac{\nu+1}{\nu+h^2}};\nu+1\right)$$
$$\left[\frac{\nu-1}{\nu}h^2-(1-\delta^2)-\frac{\Gamma\left(\frac{\nu+1}{2}\right)}{\pi^{\frac{1}{2}}\nu^{\frac{1}{2}}\Gamma\left(\frac{\nu}{2}\right)}\delta(1-\delta^2)^{\frac{1}{2}}h\left(1+\frac{h^2}{\nu(1-\delta^2)}\right)^{-\frac{1}{2}}+\right.$$
$$\left.\delta^2(1-\delta^2)\left(1+\frac{h^2}{\nu(1-\delta^2)}\right)^{-1}\right]$$

5.5 The extreme values of the skew$-t$ random field

Let $M_h^+(Y,S)$, and $M_h^-(Y,S)$, be the number of the local maxima and the number of the local minima, greater and less than a threshold h, respectively, of a the skew$-t$ random field Y inside S. Then, the following theorem gives the expected number of the local maxima and minima of Y inside S.

Theorem 5.5.1. *Under the regularity conditions, for a stationary skew$-t$ random field, Y, and for $\nu > N$,we have:*

$$(i)\ \mathbb{P}[M_h^+(Y,S)] = \frac{vol_N(S)det(\mathbf{\Lambda})(\nu-1)!\nu^{\frac{\nu-N}{2}}\Gamma\left(\frac{\nu-N+1}{2}\right)}{2^{N-1}(\pi)^{\frac{N+1}{2}}(1-\delta^2)^{\frac{N-1}{2}}(\nu-N)!\Gamma\left(\frac{\nu}{2}\right)}h^{-(\nu-N)}T_1(\alpha\sqrt{\nu+1};\nu+1)$$
$$\times\left\{1+O(h^{-1})\right\}$$
$$(ii)\ \mathbb{P}[M_h^-(Y,S)] = \frac{vol_N(S)det(\mathbf{\Lambda})(-1)^{N-1}(\nu-1)!\nu^{\frac{\nu-N}{2}}\Gamma\left(\frac{\nu-N+1}{2}\right)}{2^{N-1}(\pi)^{\frac{N+1}{2}}(1-\delta^2)^{\frac{N-1}{2}}(\nu-N)!\Gamma\left(\frac{\nu}{2}\right)}h^{-(\nu-N)}$$
$$\times T_1(-\alpha\sqrt{\nu+1};\nu+1)\left\{1+O(h^{-1})\right\}$$

$vol_N(S)det(\mathbf{\Lambda}) = \mathcal{L}_2(S)$ is the $N-$dimensional Lipschitz-Killing curvature of S, and $\alpha = \delta/\sqrt{1-\delta^2}$ is the skewness parameter.

Proof. using the formulae in and conditional on Y, W and Z we can write:

$$\mathbb{P}[M_h^+(Y,S)] = vol_N(S)\det(\mathbf{\Lambda})\frac{1}{\sqrt{2\pi}}\int_h^\infty\int_{-\infty}^\infty \mathbb{E}_W\left[\mathbb{E}\left[-\det(\ddot{\boldsymbol{Y}}^-)|\dot{\boldsymbol{Y}}=\mathbf{0},Y=y,W,Z\right]\right.$$
$$\left.\times p_{\dot{\boldsymbol{Y}}}(\mathbf{0};y,W,Z)\right]e^{-u^2/2}p_Y(y)dudy$$

where $p_{\dot{\boldsymbol{Y}}}(\mathbf{0};y,W,Z)$ is the probability density function of $\dot{\boldsymbol{Y}}$ at $\mathbf{0}$ conditional on $Y=y$, W, and Z, and $p_Y(y)$ is the probability density function of Y.
From Lemma 5.3.1, for $\dot{\boldsymbol{Y}}=\mathbf{0}$ and letting $Y\to\infty$, $\ddot{\boldsymbol{Y}}$ will converge to the following negative definite matrix:

$$\ddot{\boldsymbol{Y}} \to -\left(1+Y^2/\nu\left(1-\delta^2\right)\right)YW^{-1}P(1+O(Y^{-1})) \tag{5.22}$$

Thus, by computing the determinant of $\ddot{\boldsymbol{Y}}^-$, and multiplying by $p_{\dot{\boldsymbol{Y}}}(\mathbf{0};y,W,Z)$, we obtain:

$$\mathbb{E}\left[-\det(\ddot{\boldsymbol{Y}}^-)|\dot{\boldsymbol{Y}}=\mathbf{0},Y=y,W,Z\right]p_{\dot{\boldsymbol{Y}}}(\mathbf{0};y,W,Z) =$$
$$(2\pi\nu(1-\delta^2))^{-\frac{N}{2}}y^NW^{-\frac{N}{2}}\mathbb{E}[\det(P)](1+O(y^{-1}))$$

where $\mathbb{E}[\det(P)] = (\nu-1)!/(\nu-N-1)!$, and $p_{\dot{\boldsymbol{Y}}}(\mathbf{0};y,W,Z) = (2\pi\nu(1-\delta^2)(1+y^2/\nu(1-\delta^2))^2W^{-1})^{-N/2}$.
Computing the expectations over the non-central $\chi^2_{\nu+1}$, denoted by W, conditional on Z, then integrating over Z, we get:

$$\mathbb{E}_W\left[\mathbb{E}\left[-\det(\ddot{\boldsymbol{Y}}^-)|\dot{\boldsymbol{Y}}=\mathbf{0},Y=y,W,Z\right]p_{\dot{\boldsymbol{Y}}}(\mathbf{0};y,W,Z)\right] =$$
$$\frac{(\nu-1)!\Gamma\left(\frac{\nu-N+1}{2}\right)y^N}{2^N(\pi\nu)^{\frac{N}{2}}(1-\delta^2)^{\frac{N-1}{2}}(\nu-N-1)!\Gamma\left(\frac{\nu+1}{2}\right)}$$

Multiplying by the density of Y, yields:

$$\mathbb{E}_W\left[\mathbb{E}\left[-\det(\ddot{\boldsymbol{Y}}^-)|\dot{\boldsymbol{Y}}=\mathbf{0}, Y=y, W, Z\right] p_{\dot{\boldsymbol{Y}}}(\mathbf{0}; y, W, Z)\right] p_Y(y) = \frac{2(\nu-1)!\Gamma\left(\frac{\nu-N+1}{2}\right)\nu^{\frac{\nu-N}{2}} y^{N-\nu-1}}{2^N(\pi)^{\frac{N+1}{2}}(1-\delta^2)^{\frac{N-1}{2}}(\nu-N-1)!\Gamma\left(\frac{\nu}{2}\right)} T_1(\alpha\sqrt{1+\nu}; \nu+1)$$

Then by integrating and over y, we obtain the first result (i).
Notice that $\mathbb{P}[M_h^-(Y,S)] = \mathbb{P}[M_{-h}^+(-Y,S)]$. Thus, by evaluating the expectations of $\mathbb{P}[M_{-h}^+(-Y,S)]$ and following the same previous arguments when letting $h \to \infty$, we give the result in (ii) and ends the proof. □

Corollary 5.5.1. *Let $Y_{max} = sup\{Y(\boldsymbol{x}) : \boldsymbol{x} \in S\}$, and $Y_{min} = inf\{Y(\boldsymbol{x}) : \boldsymbol{x} \in S\}$. Then, for $\nu > N$, when $h \to \infty$:*

$$\begin{aligned}
(i)\ \ \mathbb{P}[Y_{max} \geq h] \to & \frac{vol_N(S) det(\boldsymbol{\Lambda})(\nu-1)!\nu^{\frac{\nu-N}{2}}\Gamma\left(\frac{\nu-N+1}{2}\right)}{2^{N-1}(\pi)^{\frac{N+1}{2}}(1-\delta^2)^{\frac{N}{2}}(\nu-N)!\Gamma\left(\frac{\nu}{2}\right)} h^{-(\nu-N)} \\
& \times T_1(\alpha\sqrt{\nu+1}; \nu+1), \\
(ii)\ \ \mathbb{P}[Y_{min} \leq h] \to & \frac{vol_N(S) det(\boldsymbol{\Lambda})(-1)^{N-1}(\nu-1)!\nu^{\frac{\nu-N}{2}}\Gamma\left(\frac{\nu-N+1}{2}\right)}{2^{N-1}(\pi)^{\frac{N+1}{2}}(1-\delta^2)^{\frac{N}{2}}(\nu-N)!\Gamma\left(\frac{\nu}{2}\right)} h^{-(\nu-N)} \\
& \times T_1(-\alpha\sqrt{\nu+1}; \nu+1)
\end{aligned} \tag{5.23}$$

5.6 Simulation results on two-dimensional rectangles

In this section, simulation examples of the skew$-t$ random fields are illustrated for positive (resp. negative) values of the skewness parameter α.
The analytical expressions of the mean Lipschitz-Killing curvatures, $\mathcal{L}_j[E_h(Y,S)]$, are tested with the ones computed numerically from the simulations for illustration and validation. For this aim, 100 realizations of the skew$-t$ random fields have been generated for two different examples. The simulations are investigated on a rectilinear lattice of 512×512 points in both x and y directions within the unit square $[0,1]^2$. Figures 5.2(a) and 5.3(a) illustrate two exemplars of stationary skew$-t$ random fields. In the first example, 6 (i.i.d) anisotropic Gaussian random fields are generated from the convolution of the Gaussian white noise with a Gaussian covariance kernel of size $\sigma_x = 3$ pixels, and $\sigma_y = 28$ pixels. Then, anisotropic skew$-t$ random field of 5 degrees of freedom and skewness parameter $\alpha = -0.7$ is generated using equation (5.5), (see Fig. 5.2(a)).
In the second example, an isotropic skew$-t$ random field of 5 degrees of freedom and skewness parameter $\alpha = 2$ is generated in this time using isotropic Gaussian covariance kernel of size $\sigma_x = \sigma_y = 3$ pixels, (see Fig. 5.3(a)). The analytical and simulated Lipschitz-Killing curvatures are represented in figures 5.2(b) and 5.3(b),

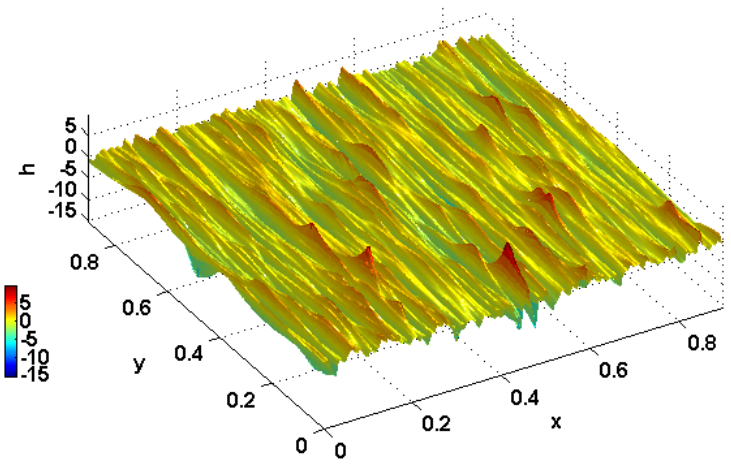

(a)

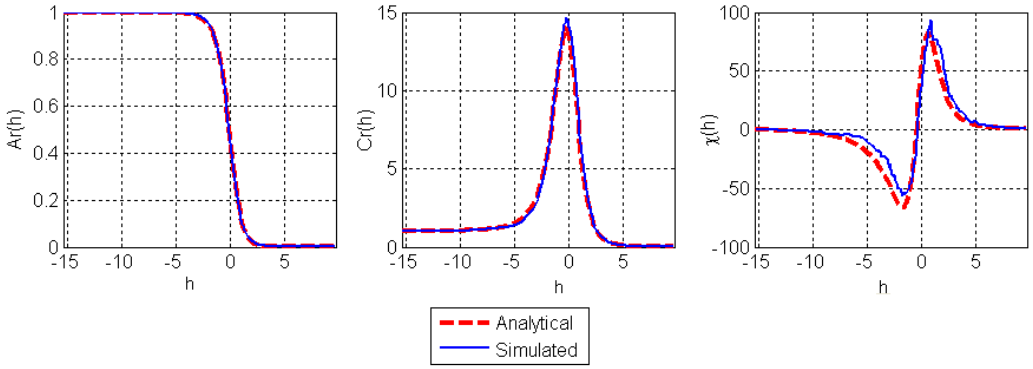

(b)

Figure 5.2: First exemplary simulation. (a) Anisotropic skew $-t$ random field with 5 degrees of freedom and skewness $\alpha = -0.7$ realized on $[0,1]^2$ with resolution 512×512 points. (b) The simulated and the analytical LKCs, Ar, Cr and χ, respectively.

respectively.

The simulation results in both examples show good approximation to the theoretical expectations.

5.7 Conclusion

In this chapter, a skew$-t$ random field is introduced and the expected EC densities are derived analytically on $\mathbb{R}^N$, $(N > 1)$. Furthermore, we give in this chapter the estimated value of the number of the global maxima and minima, which can be derived from the expected Euler-Poincaré characteristic at high thresholds. This chapter is ended with simulation results for validation on two-dimensional excursion sets.

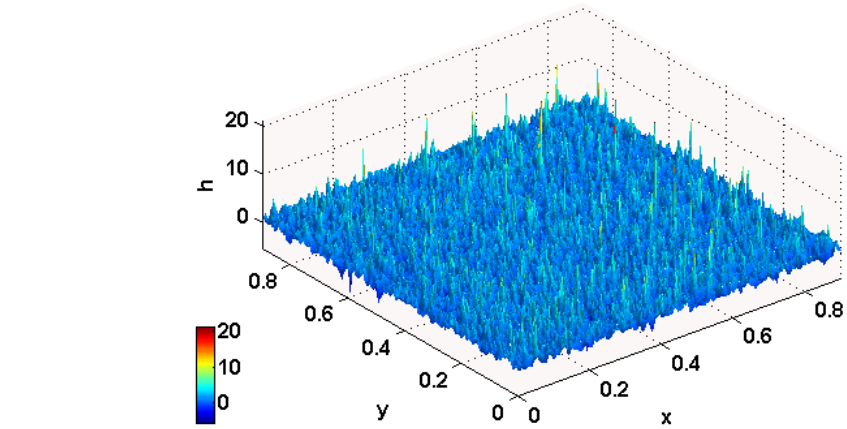

(a)

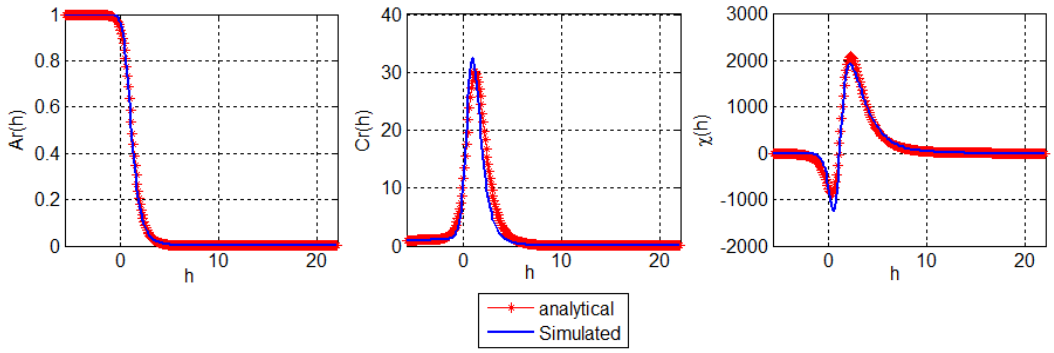

(b)

Figure 5.3: Second simulation example. (a) Isotropic skew $-t$ random field with 5 degrees of freedom and skewness $\alpha = 0.7$ realized on $[0,1]^2$ with resolution 500×500 points. (b) The simulated and the analytical LKCs, Ar, Cr and χ, respectively.

Part IV

APPLICATION: CASE STUDY

Chapter 6

Medical and scientific issue

Contents

6.1 Total hip replacement 63
6.2 Choice of materials 63
6.3 Wear of UHMWPE 64
6.4 Motivations and objectives 65

6.1 Total hip replacement

The total hip replacement is one of the most performed procedures, and is always in increasing. In France, more than 80000 total hip arthroplasty (THA) were performed in 2001. Nowadays, 120000 THA are being performed each year, and about 800000 in Europe. The reason behind these increasing numbers is related to the great success of the THA and hence, the amelioration that can offer to the patients who suffer from the osteoarthritis, necrosis, bone tumour and other related problems.
A total hip arthroplasty is an orthopaedic procedure that involves surgical replacement of the hip joint components with an artificial prosthesis. The prosthetic implant (Fig. 6.1) consists of a femoral stem associated with a femoral head placed on the upper part of the stem, and articulated with an acetabular insert (or cup). A socket (acetabular or metal-back) fixed inside the acetabulum of the pelvis is used as an intermediate component between the cup and the latter [GBFF10, GBF11]. The introduced design of the artificial implant is due to Bousquet [BGG$^+$85], and it is defined by the dual mobility. It involves producing two kinds of articulating surfaces; one is between the head and the acetabular insert, or the cup, and the other is between the cup and the metal-back, increasing by this way the amplitude of the joint movements as possible and allowing for more flexible implant. The acetabular insert drawn in such design is called the dual mobility cup.

6.2 Choice of materials

Various materials are used in total hip implant, for the couple head-cup. They are categorized between three essential groups: metal-on metal, ceramic-on-ceramic, and metal-on-polymer [GBF11]. The materials used in the present work belong to

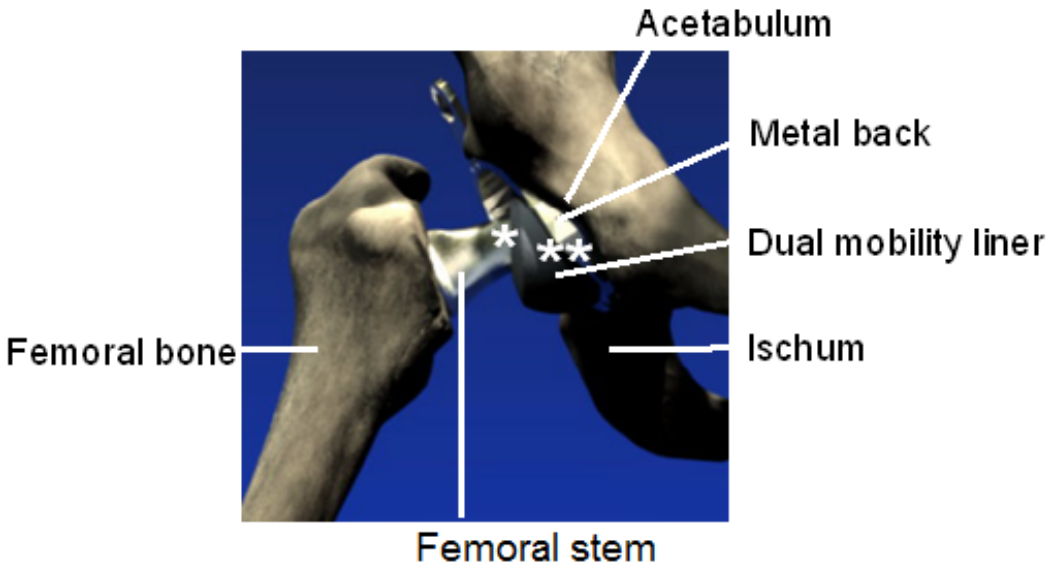

Figure 6.1: An illustration of the total hip implant [GBF11].

the third category. The femoral head has been chosen to be made of stainless steel alloys (SS 316L or SS 316LN), and the cup is composed of a high-molecular-weight polyethylene (UHMWPE). For the femoral stem and the metal-back, they might be made of one of the mostly used metals: stainless steel alloy, titanium alloy, or cobalt-chromium-molybdenum [SJ95]. The couple metal-UHMWPE becomes nowadays one of the most used options for the total hip implant (THI). The reason is due to the low friction coefficient, and the hardness of the UHMWPE component (or bearing surface) which provides an ideal stability and compatibility between the prosthetic articulations [FPDF09, Lew01].

6.3 Wear of UHMWPE

The major problem of the UHMWPE is associated with its resistance to the wear which depends on its chemical structure. The wear particles (debris) reduced from the UHMWPE during its sliding against the femoral head or the metal-back is one of the most intrinsic factors that will accelerate the degradation (loosening) of the UHMWPE, and hence reduces the *in-vivo* life duration of the implant. Furthermore, the generated wear debris will influence the structure of the bone [FPDF09, Lew01], such as changing the osteoclast, and osteoblast activity which might lead to the bone resorption and other non expected effects.
The wear of UHMWPE is related to several factors such as the geometric structure of the acetabular cup, that means its shape, thickness and diameter, the roughness of the articulated surfaces, and the type of the materials of both the femoral head

and the metal-back [WEP+98, GWG+08].

6.4 Motivations and objectives

As mentioned in the previous section, the roughness of the articulating surfaces is one of the reasons, actually a main reason, beyond the wear of the UHMWPE component. We should distinguish between different types of contact conditions for either head-UHMWPE or metal-back-UHMWPE: rough-on-rough, rough-on-smooth, and smooth-on-rough. The wear mechanisms [ASZ+08] of the UHMWPE surface strongly depend on the contact condition of the bearing surface [GWG+08], and it is governed by the roughness of the bearing surface where such types of contacts occur predominantly at the asperity levels [1]. We are interested in the third condition type, smooth (highly polished) metal-back (or femoral head) on rough UHMWPE component.
The aim of this application part is to interpret the wear mechanisms, and to analyze the functional behaviour of the rough UHMWPE surface, during the sliding contact against the smooth metal-back surface, by means of its topographic roughness map. A geometrical stochastic model based on integral geometry and random fields framework is proposed to model the topographic roughness during a long duration wear engineering simulation process. The predominant wear mechanisms of the UHMWPE are then defined and associated to the dynamic changes of the surface hills/valleys at high levels. Thanks to this model one can estimate how much high these levels, and quantify the geometric properties of the level sets that include such hills and valleys to achieve our aim.

Before tackle the model of the surface roughness topography, the next chapter presents the experimental tools used to generate the wear on the UHMWPE component in order to obtain worn surfaces, and the technical instrumentation methods for observing and measuring the roughness topography.

1. Surface asperities are the alternating hills (local height maxima) of rough surfaces observed in the microscopic scale. They are referred to as peaks in a profile (two-dimensions), and summits in a surface map (three-dimensions) [Bhu99]. In this thesis we used the mathematical notation hills to refer to these asperities.

Chapter 7

Experimental developments

Contents

7.1 Wear engineering simulation 67

7.2 Surface roughness topographical measurements 69

7.2.1 Instrumental measurements 69

7.2.2 Removing gross geometry and form errors 70

7.3 Conclusion 72

7.1 Wear engineering simulation

The wear tests are conducted by a one-station hip walking simulator (Fig. 7.1), 858 Mini Bionix® II test system (MTS), in experimental environment corresponds to the dynamic conditions of the the normative reference ISO 14242-1 [ISO02], to emulate the *in-vivo* hip movements. The artificial hip components, socket, cup, and femoral components (head, neck and stem), were positioned (Fig. 7.2 (a)) anatomically. A time-dependent axial loading force (held on Z axis), varies between $300N$ and $3KN$, is applied though the central axis of the socket. Then, internal/external rotation, flexion/extension, and abduction/adduction are applied to the socket so the acetabular cup was initially positioned at 30° in the plane (ZX) (Fig. 7.2 (b)). The load force and the motions were all independently controlled.

The tests were run at a frequency of 1Hz with physiological lubricant (calf serum) being replaced every $500,000$ cycles. The lubricant is controlled to the temperature $37° \pm 2°C$. Flexion/extension motion of $+25°$ and $-18°$, abduction/adduction motion of $+7°$ and $-4°$, and internal/external rotation of $+2°$ and $-10°$ were all applied to the socket with the mechanical contact to emulate those found *in-vivo*. The kinematic and environmental conditions (table 7.1) have been applied with respect to the standard norm of the simulator ISO 14242-1.

All the measurements related to wear rate, and roughness topography of the UHMWPE were realized every one million cycles. The total number of achieved cycles was approximately 20 million cycles.

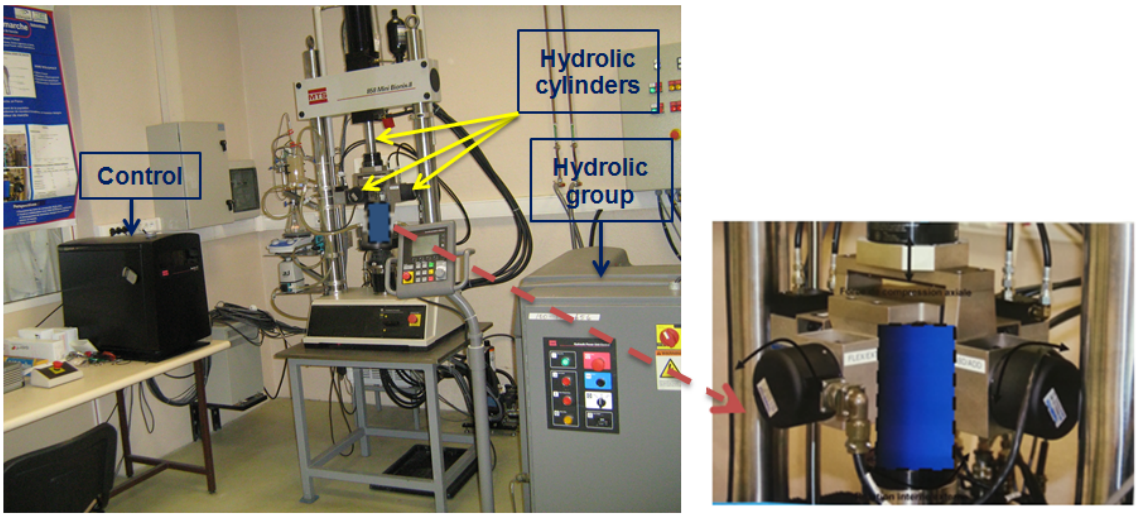

Figure 7.1: (a) General view of the one-station hip walking simulator. (b) Max view of the the hip implant location and the machine axes.

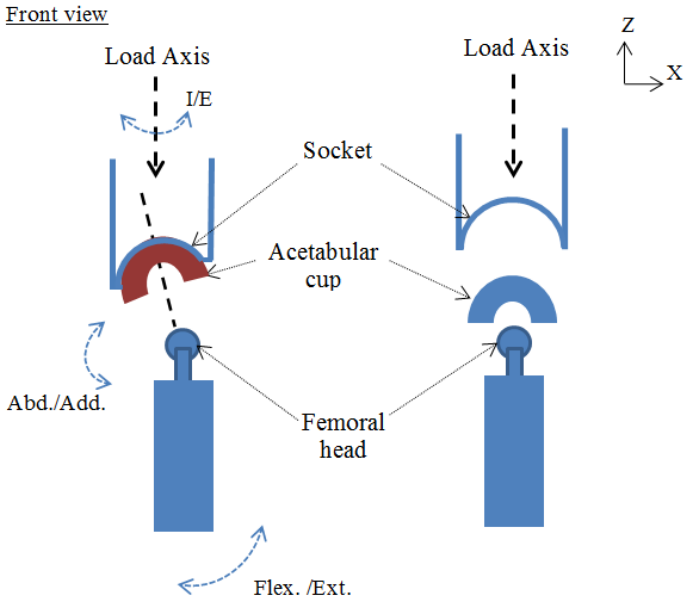

Figure 7.2: Diagram of the artificial hip components with position conditions relative to the load force (front view). Abd./Add. refers to the abduction/adduction motion, Flex./Ext. is the flexion/extension motion and I/E is the internal/external motion.

Table 7.1: Wear test conditions of MTS-858 testing machine:

Parameters	**ISO14242-1**
Normal load force	$3.2KN$
Frequency	$1.0Hz$
Cup inclination	30°
Adduction/Abduction	$+7^{\circ}/-4^{\circ}$
Flexion/Extension	$+25^{\circ}/-18^{\circ}$
Internal/External	$+2^{\circ}/-10^{\circ}$
Test fluid	calf serum
Temperature	37°
Test cycles	1×10^{6}cycles

7.2 Surface roughness topographical measurements

Surface topography is of multiscale nature, ranging from its macroscopic scales to the microscopic or atomic scales. For engineered surface, surface topography can be restricted to below certain length scale, smaller than the physical size scale of the material component. These small-scale variations are of micrometer scales and referred to as surface roughness, which are the focus of the present thesis. This section presents the technical methods used to measure and observe the topographic map of rough engineered surfaces, and the experimental implementations for restoring the roughness topography from the global geometric form of the surface topography.

7.2.1 Instrumental measurements

Surface roughness topography has been firstly obtained using the tactile profilometer [Sch06, JSWB07a, JSWB07b]. A stylus is dragged over the surface and record the vertical deflections as the stylus moves along a line over the surface. This technique provides one-dimensional profile, measured with contacting stylus. Later, two-dimensional profile measurements have been investigated to represent the surface roughness topography. The contact profile techniques are not adequate for measuring a complete 3D height maps [DS95]. They might be damaged, and they would damage the surface being measured with the direct contact, besides to the important limitations related to the measurement's wavelength and measurement's speed. Recently, contact profiler techniques have been replaced by non-contact optical methods [JSWB07b], such as the interferometry, which allowed measuring a full and complete 3D height map at once and the possibility of storing it as a 2D image. The optical techniques are fast, non-contact, and are thus more convenient for measuring the surface topography [Sch06].

The convex UHMWPE surface was measured, at different wear times, using a

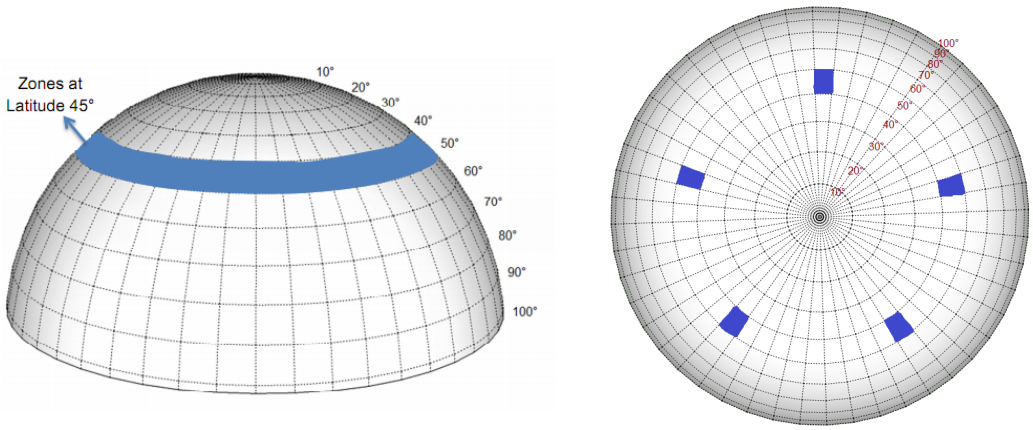

(a) Side view (b) Top view

Figure 7.3: A synthetic $3D-$dimensional simulation of the convex UHMWPE acetabular cup. (a). a side view of the cup. The blue colored zone refers to the latitude 45°. (b) a top view of the cup. The selected samples around the 45° are refereed by blue color.

white light vertical scanning interferometer, (Bruker nanoscope (r), Wyko® NT 9100, ex. Veeco), [NT-, Wya02], which enables producing a fast, non-contact, true three-dimensional area measurements for both smooth and rough surfaces to nanometre precision.
Selected samples (Fig.7.3) of the worn surfaces were suggested from the zones at the latitudes 45° and 100°. The samples were digitized and 3D maps of real heights were represented on a rectilinear lattice of 480×640 points with spatial resolution equals to $\triangle x = 1.8\mu m$, and $\triangle y = 1.8\mu m$ in both X and Y directions, respectively. Fig. 7.4 illustrates four exemplars of these worn surfaces.

7.2.2 Removing gross geometry and form errors

Generally engineering surfaces are composed of three essential components, namely form, waviness, and roughness components [Whi94]. The heights variations of each component are considered of different length scales, or equivalently wavelengths. The form component has a gross geometric shape (e.g.; perfect flat shape, perfect cylindrical shape, spherical shape,...etc). It is composed of spatial components located on the largest scales with wavelength equals to, or greater than, 1/3 the sample length [Whi94], in the measurement space. The waviness and the roughness components define the surface texture [Cor04]. In fact, there is a great ambiguity, in the literature (see chapter 1), about which wavelengths define each the waviness and the roughness components of the topography. Likewise; if they should be separated or assessed together, since they are dependent [Bhu99], and also their wavelength ranges differ according to the manufacturing process [Whi94, Cos00]. In

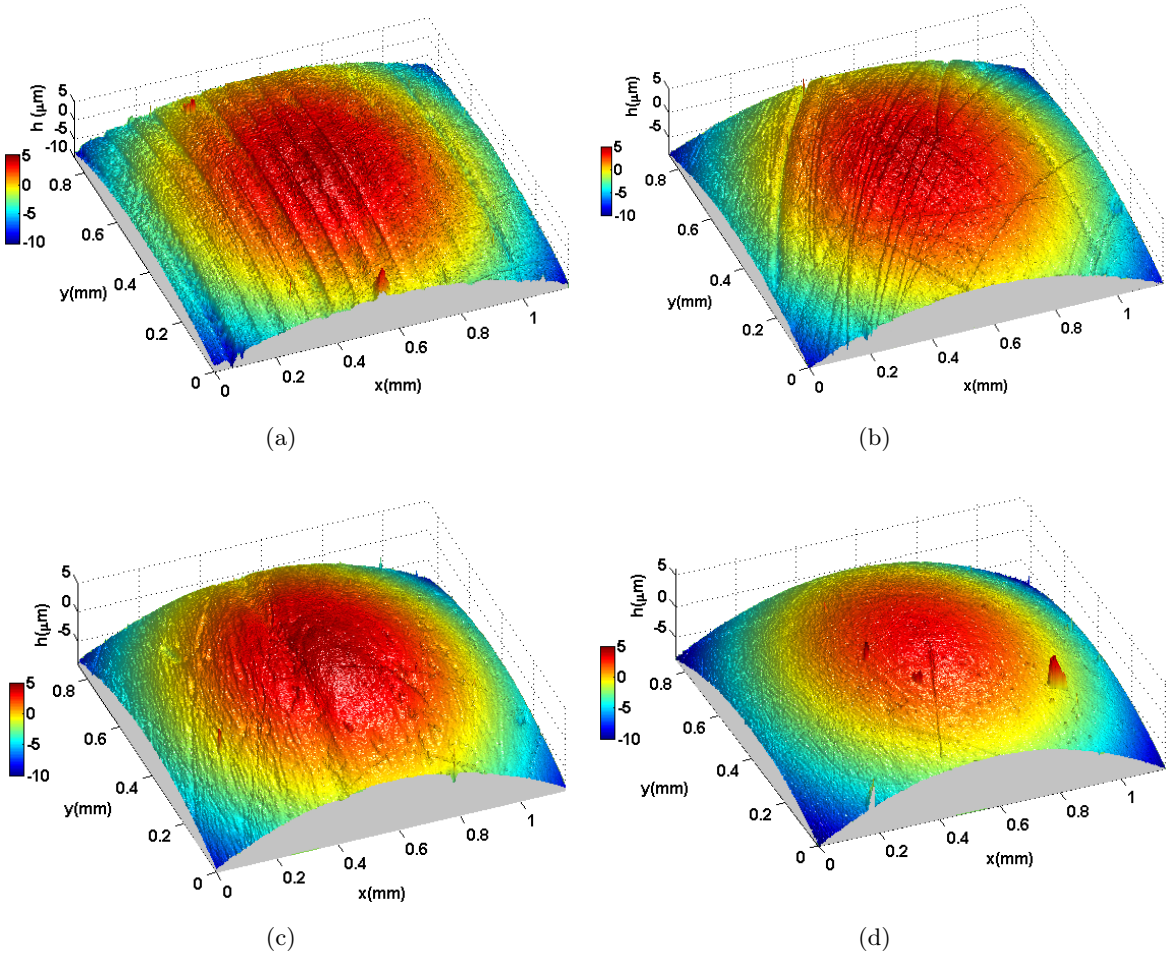

Figure 7.4: Surface topography of four selected samples of the worn UHMWPE surfaces, from the latitude 45°, at different wear time cycles, observed by white light interferometer (NT 9100) with $5.5X$ objective lens, on a maximum measurement space $1.1 \times 0.9mm^2$ with spatial resolution of $\triangle x = 1.8\mu m$, and $\triangle y = 1.8\mu m$ in both X and Y directions. (a) wear time $= 2 \times 10^6$cycles. (b) wear time $= 9 \times 10^6$cycles. (c) wear time $= 11 \times 10^6$cycles.(d) wear time $= 19 \times 10^6$cycles.

our work, the waviness component is included in the surface roughness component, and they are both referred to as surface roughness.
The surface may contain gross deviations resulted from the nominal shape of long wavelength, known as the error of the form. They are not considered as part of the surface texture [Bhu99], and they include the tilt, curvature and the mean heights. This error type should be removed before characterizing or analysing the surface roughness.
These gross geometry effects have been removed using a parabolic fitting algorithm of the form:

$$z(x, y) = -ax^2 - by^2 + c, \ (a > 0, b > 0, c > 0) \tag{7.1}$$

to the three dimensional surface profile. The coefficients are computed using the least-squares fit. Then, the typical form (Fig 7.5) has been subtracted from the surface topography, giving the roughness topography (Fig. 7.6). The roughness is represented by the heights variations relative to a reference plane.

7.3 Conclusion

This chapter highlighted the materials and the technical methods used to generate the *in-vitro* wear on the UHMWPE surface, in conditions similar to those *in-vivo*, using the hip simulator mentioned in section 7.1. Worn UHMWPE surfaces were measured at different wear times using the optical white light interferometer allowing for a complete 3D height maps visualization. The roughness topography has been restored after removing the gross geometry and the form errors. Ones the roughness map is restored, one can characterize and analyse the roughness by different ways depending on the application and the way the roughness is being measured and defined. The observed height maps are basically 2D images, and hence, image analysis methods are widely used for the roughness characterization. Among those methods are the model-based approaches discussed in chapter 1 such as random fields. The next chapter will focus on applying the results obtained from the random fields introduced in Part II of this thesis, to represent the roughness topography of the UHMWPE surface. Furthermore, a statistical analysis method has been performed to estimate the evolution of the hills/valleys affected by the wear process.

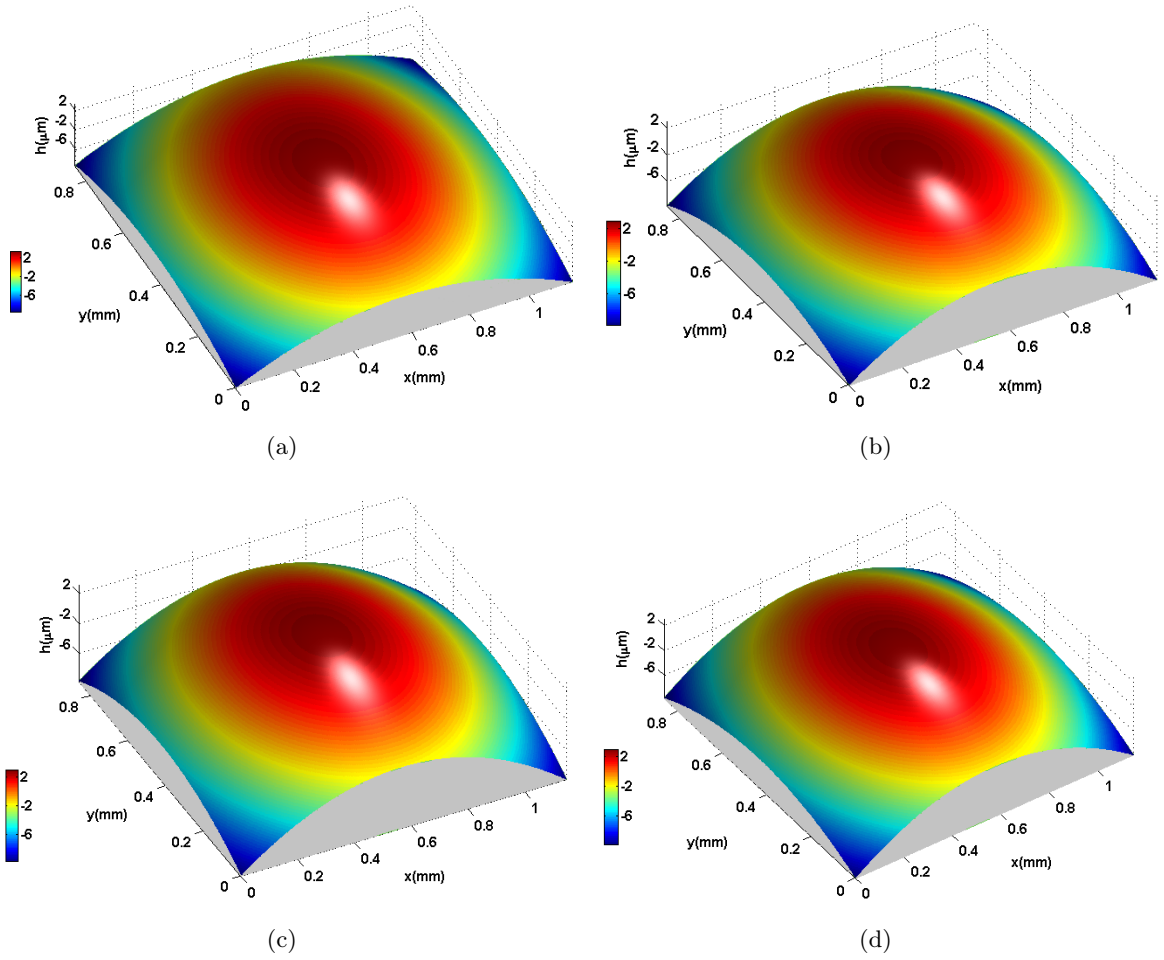

Figure 7.5: Gross geometry of the four selected samples, illustrated in Fig. 7.4, of the worn UHMWPE surfaces at different wear time cycles.(a) wear time $= 2 \times 10^6$ cycles, (b) wear time $= 9 \times 10^6$ cycles. (c) wear time $= 11 \times 10^6$ cycles. (d) wear time $= 19 \times 10^6$cycles.

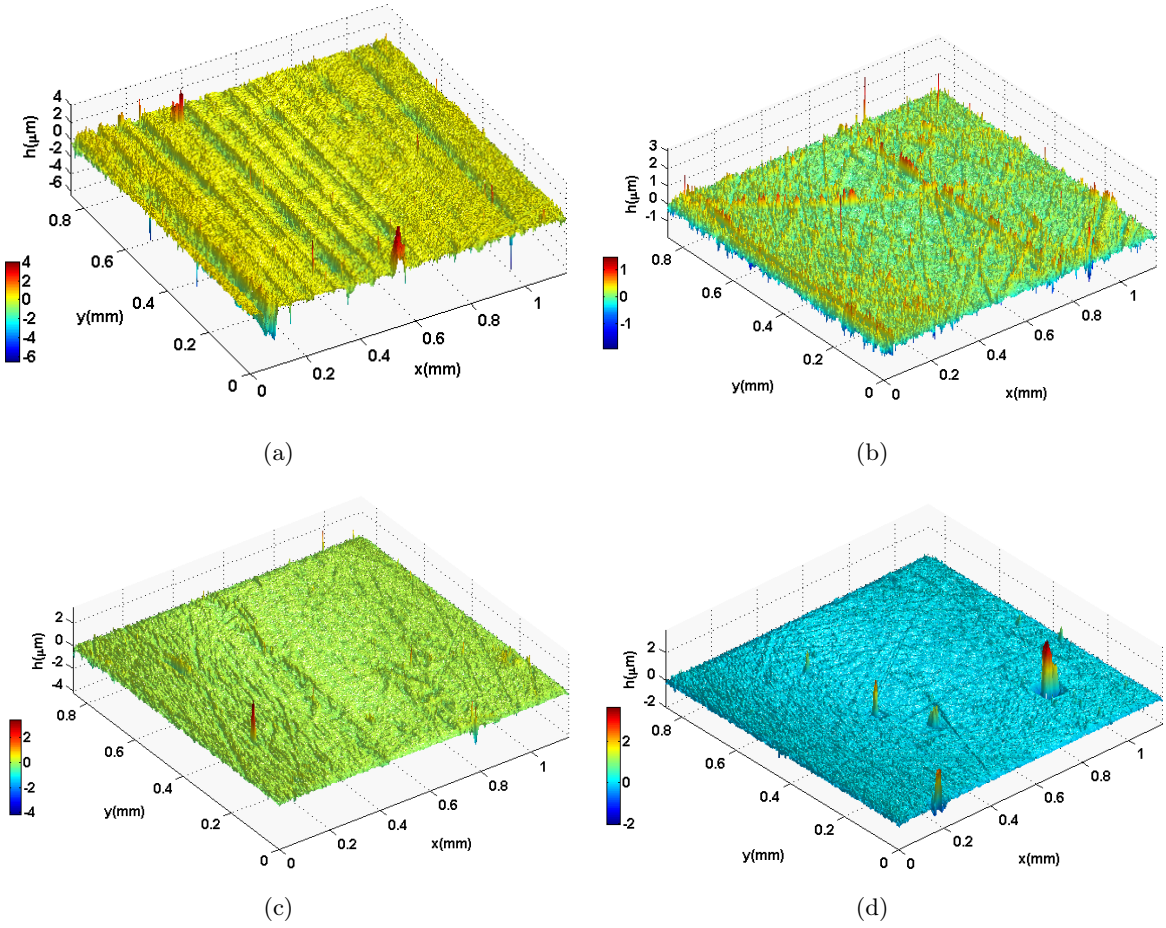

Figure 7.6: Roughness topography restored from the topography of the four selected samples, illustrated in Fig. 7.4, of the worn UHMWPE surfaces at different wear time cycles. (a) wear time $= 2 \times 10^6$cycles. (b) wear time $= 9 \times 10^6$cycles. (c) wear time $= 11 \times 10^6$cycles.(d) wear time $= 19 \times 10^6$cycles.

Chapter 8

Methodological developments

Contents

8.1 Introduction 75
8.2 Modelling the topographic roughness of the UHMWPE surface before wear 76
8.2.1 Parameter's estimation 76
8.2.2 Validation 78
8.3 Modelling the topographic roughness of the worn UHMWPE surfaces 80
8.3.1 Parameter's estimation 81
8.3.2 Validation 83
8.4 Statistical analysis of worn surfaces 83
8.4.1 Estimation of the significant levels from uncertainty heights . 83
8.4.2 Comments 85
8.4.3 Wear analysis induced by the statistical analysis of surface roughness 85
8.5 Results and discussion 89
8.5.1 Worn regions of the UHMWPE surface at the latitude 45° . . 89
8.5.2 Quantitative comparison between worn regions at 45° and 100° latitudes 92
8.6 Conclusion 92

8.1 Introduction

In this chapter, we are interested in studying a practical application associated with the functional behaviour of the UHMWPE surface, throughout a group of selected samples measured and observed by the optical interferometry, after removing the gross geometry and the form errors (see section 7.2). We apply the random field models defined in chapter 4 and chapter 5 to firstly model the topography of the manufactured UHMWPE surface, and then the deformed one during a wear process, respectively. The Euler-Poincaré characteristic is used particularly to predict the significant height levels from the uncertainty ones that might be related to errors of measurements.

We remind that the surface topography is composed of textural features of multi-scale nature, and we focus on the small-scale features defined by the hills and valleys

Table 8.1: roughness parameters

Machined UHMWPE	$S_a(\mu m)$	$S_q(\mu m)$	S_{sk}	S_{ku}
Sample 1	1.46	1.76	0.42	6
Sample 2	1.41	1.73	0.3	6.35
Sample 3	1.44	1.7	0.33	5.29

and located at high levels. These small-scale features are refereed to, in the literature, as roughness component of the rough surfaces. A statistical analysis method is developed to describe the evolution of the hills/valleys (roughness variability) and the functional behaviour of the UHMWPE surface during the wear process, and it has been published in [AGGP13].

8.2 Modelling the topographic roughness of the UHMWPE surface before wear

The topographic roughness of the UHMWPE after a machining process (Fig. 8.3) has been measured, digitized on a rectilinear lattice of 640×480 points, and extracted after removing the gross geometry and the form errors (see chapter 7). The total measurement area is about $A = 1.2 \times 0.86mm^2$ and the spatial resolution in both x and y directions is $1.8\mu m$. The topographic roughness is composed of large-scale structures (low frequency) periodic (anisotropic) and suitably smooth, and small-scale, rotation-invariant (isotropic) ones (high frequency) with extreme and arbitrary roughness. Hence, the microgeometry of the hills and valleys is modelled by the linear mixture Gaussian-t random field introduced in chapter 4.

8.2.1 Parameter's estimation

The RMS roughness S_q [1], skewness S_{sk} and kurtosis S_{ku} parameters (see Tab. 8.1) of the surface heights are estimated, from three arbitrary samples of the UHMWPE surface without smoothing, using equations (1.1), (1.2) and (1.3), respectively. The skewness value shown in Table 8.1 is small and its influence is neglected. Thus, the surface heights distribution is assumed to exhibit a symmetric behaviour. The kurtosis value of the samples demonstrates the existence of hills and valleys at high levels spikier than being Gaussian, and they are modelled by the t random field.

8.2.1.1 Gaussian component

Using the autocorrelation function (Fig. 8.1) and the spectral method, the second order spectral moment matrix Λ_G of the large-scale components, that are modelled by the Gaussian random field, is estimated so that $\lambda_{G_y} = 15mm^{-2}$ and $\lambda_{G_x} = 117mm^{-2}$. Note that the small-scale (high frequency) structures are located in the

1. The rms roughness of the surface is equivalent to its standard deviation σ

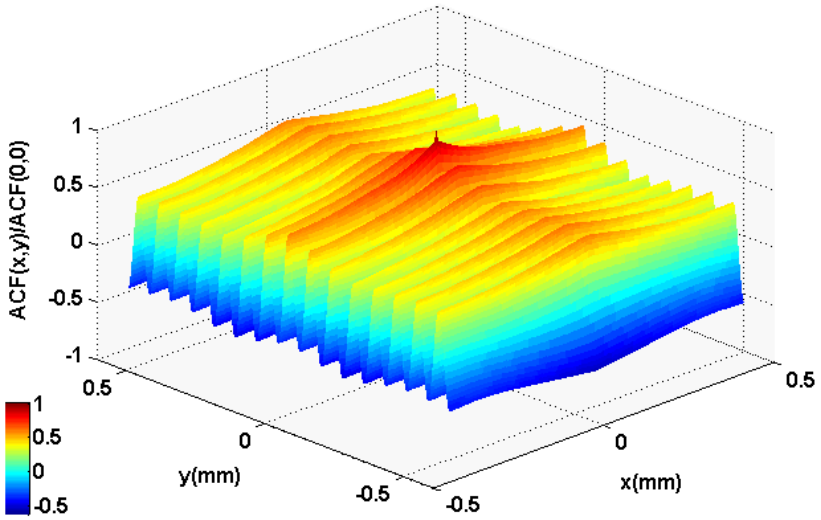

Figure 8.1: The autocorrelation function of a real 3D rough surface observed from the UHMWPE and illustrated in (Fig. 8.3(a))

origin of the autocorrelation function, where the large-scale structures are located at the long distances and they are of periodic nature.

8.2.1.2 t component

Fig. 8.2 shows the log-plot between the empirical Euler-Poincaré characteristic of the surface upcrossings and the expected Euler-Poincaré characteristic χ_G for the Gaussian random field, if the surface assumed as a Gaussian one:

$$\chi_G(h) = A \times \det(\Lambda_G)(h/S_q)exp(-h^2/2S_q^2)/(2\pi)^{3/2} \tag{8.1}$$

where A is the area of the total measurement space.
One can notice the behaviour of the local maxima (hills) above $h/S_q > 3$ compared to the Gaussian and t ones, which insures that the hills at the high thresholds do not come from the Gaussian component but from the t component. This is adequate with the fact that the LKCs detect the high-frequency features of the surface, which are due to the t random field component.
Using this assumption, the parameters of the t random field component were estimated using the non linear least-square fit between the empirical and the expected Euler-Poincaré characteristic χ_T given for the T_β^ν random field:

$$\chi_T(h) = A \times \frac{\lambda\Gamma\left(\frac{\nu+1}{2}\right)}{(2\pi)^{3/2}\left(\frac{\nu}{2}\right)^{1/2}\Gamma\left(\frac{\nu}{2}\right)}\left(\frac{h}{\beta}\right)\left(1+\frac{h^2}{\nu\beta^2}\right)^{-(\nu+1)/2} \tag{8.2}$$

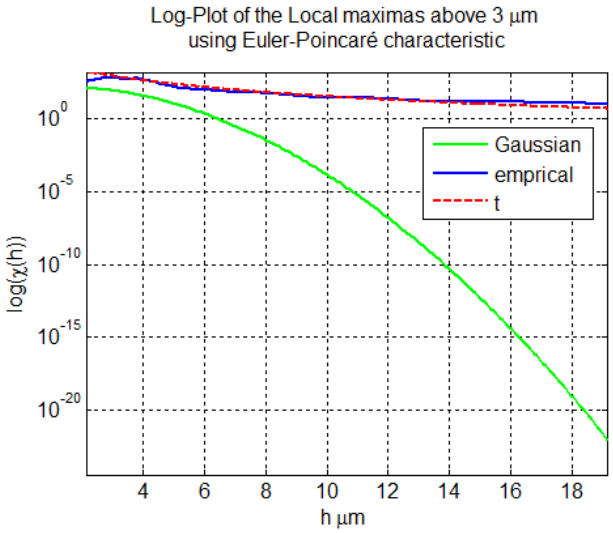

Figure 8.2: Log-Plot of the number of the local maxima using the Euler-Poincaré characteristic at high thresholds for the empirical heights and both Gaussian and t random fields

to get $\lambda = 190mm^{-2}$, for $\nu = 5$, $\beta = 1.4$. The parameters ν and β were estimated from the following equations:

$$\begin{aligned} Sq^2 &= \sigma_G^2 + \sigma_T^2 \cong \frac{\beta^2 \nu}{\nu - 2} \\ S_{ku} &\cong \frac{6}{\nu - 4} \end{aligned} \tag{8.3}$$

where the effects of the of the R.M.S. value of the Gaussian component σ_G^2 is neglected when compared to the σ_T^2.

8.2.2 Validation

For validation, the three LKCs (area function, contour length and Euler-Poincaré characteristic) of the excursion sets of the estimated Gaussian$-t$ random field $GT_{1.4}^5$ were compared with the empirical ones, computed on the surface upcrossing levels (see figure 8.3(b)). The characterizing functions show good approximation between the model and the rough surface.

8.2.2.1 Concluding remarks

Note that the t random field component of the linear mixture Gaussian$-t$ random field is assumed isotropic, whereas the anisotropic features located at larger scales are modelled by Gaussian random field, and they are estimated using the covariance function. The roughness and anisotropy properties are adequate with

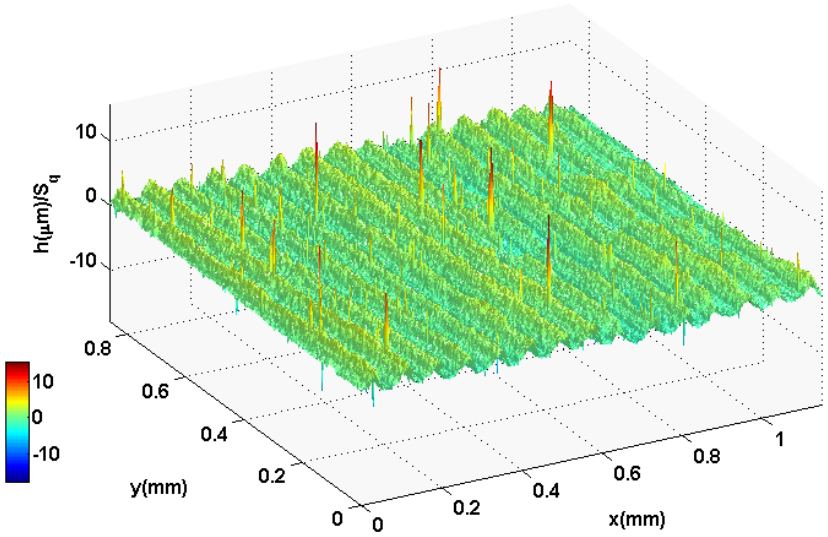

(a)

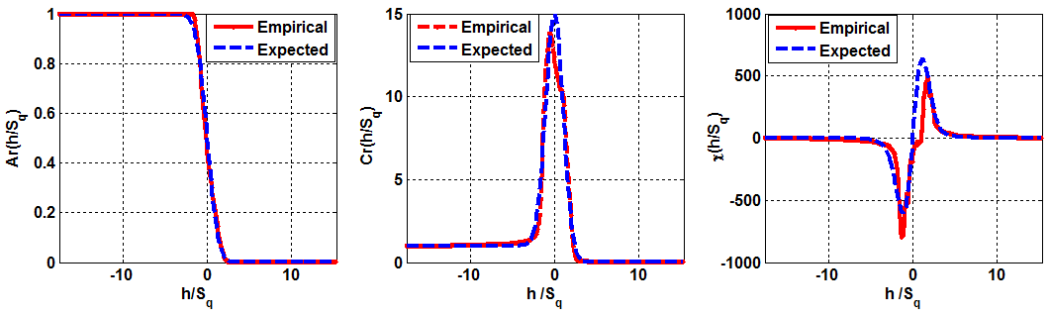

(b)

Figure 8.3: (a) A real sample of 3D rough surface observed from the UHMWPE component without smoothing. (b) Fitting the empirical, (red curve), and the expected, (blue curve), intrinsic volumes (LKCs) between the real surface upcrossings, and the $GT^5_{1.4}$ excursion sets, respectively.

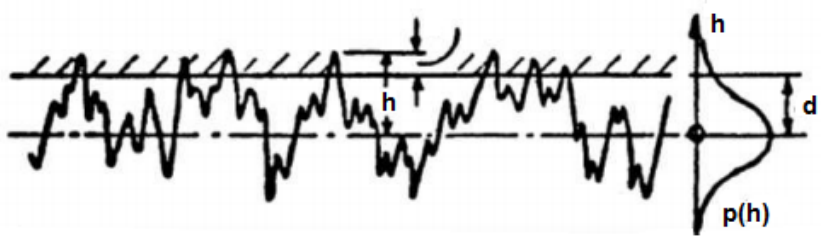

Figure 8.4: A contact deformation model between a randomly rough deformable surface and a smooth, rigid and flat one (h is the height levels, $p(h)$ is the density function, and d is the separation between the roughness reference, mean of $p(h)$, and the rigid flat surface during loading) [ZZ04].

the material properties during the machining process of the UHMWPE component [Kur04] and can be changed from one material to another. Nevertheless, the intrinsic volumes, or the LKCs, for the random field model do not depend on the shape of the covariance function but on the second spectral moment related with the derivations of the covariance function. Which means that the geometric properties of the hills and valleys can be quantified without the need to know the shape or the model of their covariance function.

8.3 Modelling the topographic roughness of the worn UHMWPE surfaces

Another application is considered for modelling the topography of rough and randomly deformable surfaces. This section focuses on the UHMWPE example which undergoes a wear engineering process as explained in chapter 7.

As seen in the previous section, the surface roughness topography is composed of two components, waviness (large-scale components) and roughness (small-scale components refereed by hills and valleys). The geometry of the small-scale hills/valleys and their number are characterized by the LKCs of the surface upcrossing's levels, since these functions tend to concentrate at the high frequencies [Sch06].
During the contact problem and wear process, the hills at the small-scales (finite contact patches) and the holes that correspond to the small-scale valleys (or the pits) are the most important and they have a direct relation with the normal pressure/hardness ratio, and the wear mechanisms [Nay73] (see Fig. 8.4 as example). In this section, we focus on modelling the microgeometry of the small-scale hills and valleys. The Lipschitz-Killing curvatures (LKCs) will be used to quantify these hills and valleys.

A rough surface illustrated in Fig. 8.5 is measured after a wear time $t = 13 \times 10^6$ cycles from the 45° latitude of the convex side of the UHMWPE component. The global roughness parameters S_q, S_{sk} and S_{ku} are estimated overall the roughness topography, such that $S_q = 34.5nm$, $S_{sk} = 4.41$ and $S_{ku} = 111.81$. The quantile-quantile (Q-Q) plot (Fig. 8.6) between the height's distribution and the Gaussian one

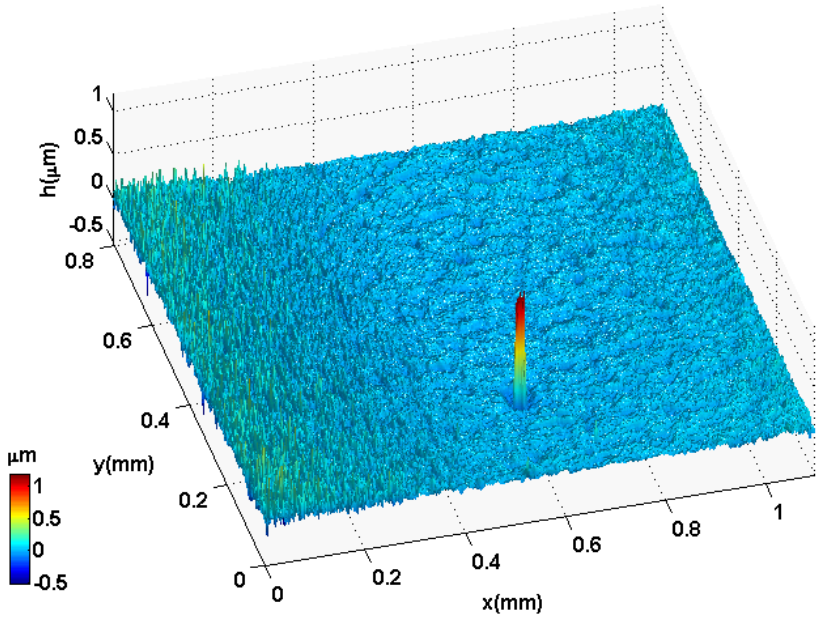

Figure 8.5: A real sample of worn surface observed at 45° latitude of the UHMWPE component at wear time $t = 13 \times 10^6$ cycles.

shows that the joint distribution of the heights tends to have asymmetric behaviour (skewed heights) around its mean and the tails of the distribution are heavier at the positive high thresholds which explains the existence of spiky hills at these heights, and a high kurtosis value. Following the last arguments, the small-scale roughness components are modelled as a skew$-t$ random field (see chapter 5). Notice that when the skewness is zero, then the skew$-t$ model of the hills and valleys becomes the t random field as seen in the previous section.

8.3.1 Parameter's estimation

The autocorrelation function (Fig. 8.7) of the roughness topography depicted in Fig. 8.5 demonstrates the roughness isotropy. The skewness index δ and the degree of freedom ν of the skew$-t$ random field were estimated using their analytical formulae [AC03]:

$$S_{sk} = \mu \left[\frac{\nu(3-\delta^2)}{\nu-3} - \frac{3\nu}{\nu-2} + 2\mu^2 \right] \left[\frac{\nu}{\nu-2} - \mu^2 \right]^{-3/2}$$
$$S_{ku} = \left[\frac{3\nu^2}{(\nu-2)(\nu-4)} - \frac{4\mu^2\nu(3-\delta^2)}{\nu-3} + \frac{6\mu^2\nu}{\nu-2} - 3\mu^4 \right] \left[\frac{\nu}{\nu-2} - \mu^2 \right]^{-2}, \quad (\text{if } \nu > 4) \tag{8.4}$$

where $\mu = \delta(\nu/\pi)^{1/2} \frac{\Gamma\left(\frac{\nu-1}{2}\right)}{\Gamma\left(\frac{\nu}{2}\right)}$, with $(\nu > 1)$.
Then, the spectral moment λ is estimated from fitting the empirical and the expected

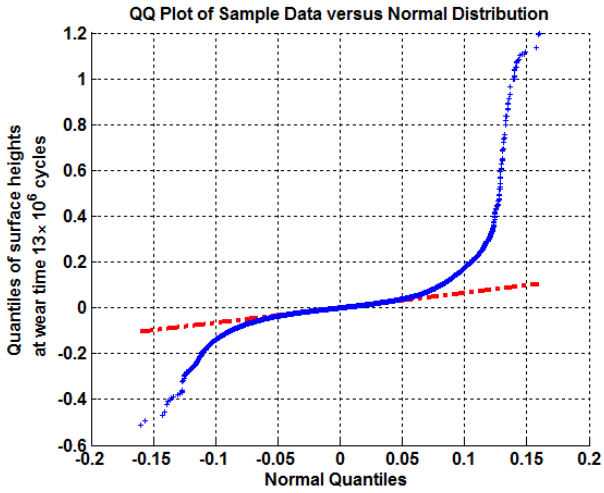

Figure 8.6: Normal Q-Q plot of the surface roughness heights, (blue plot), versus the normal distribution, (red plot), for a worn UHMWPE sample measured at 45° latitude at wear time $t = 13 \times 10^6$ cycles. The random heights are positively skewed with heavy tailed distribution of mean $\mu = 5.37nm$, and standard deviation $\sigma = 34nm$.

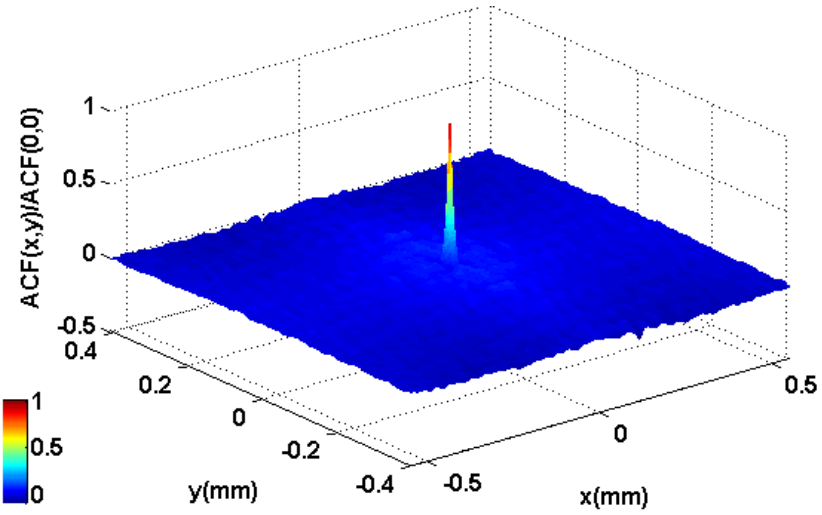

Figure 8.7: The autocorrelation function of the worn rough surface illustrated in (Fig. 8.5)

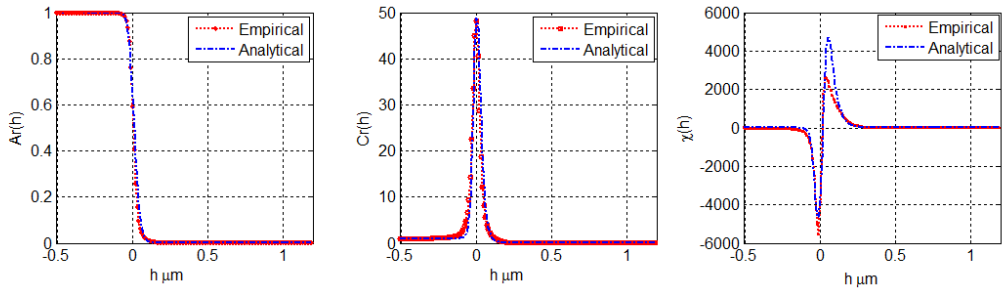

Figure 8.8: Fitting the empirical and the expected LCKs for both real surface and the skew$-t$ random field, with 10 degrees of freedom, $\delta = 0.7$ and $\lambda = 0.114\mu m^{-2}$

Euler-Poincaré characteristic between the surface upcrossing levels (excursion sets) and the skew$-t$ random field, using the non linear least-square method.

8.3.2 Validation

The intrinsic volumes or LKCs of the surface upcrossing levels (excursion sets) are simply the area, contour length and the Euler-Poincaré characteristic of these sets. These characterizing functions are used to test the skew$-t$ random field on the worn surface roughness topography, for validation, by comparing their empirical values with their analytical formulae (see Fig. 5.3(b)), with $\delta = 0.7$, $\nu = 10$ and $\lambda = 0.114\mu m^{-2}$.

8.4 Statistical analysis of worn UHMWPE surfaces during engineering wear process

Under the assumption that the roughness component of the randomly rough deformable surfaces can be modelled by the skew$-t$ random field, a statistical analysis is performed in order to estimate the significant levels including the local maxima and minima (hills and valleys). This analysis is based on the expected Euler-Poincaré characteristic of the skew$-t$ random field. Then, the mean area of these hills and valleys at the significant levels is calculated in order to describe the wear mechanisms on some regions of the UHMWPE. In this work, two regions were considered, as previously discussed in section 7.2, which are located at the longitudes 45° and 100°, and multiple samples were tested from both regions overall the latitudes.

8.4.1 Estimation of the significant levels from uncertainty heights

The local maxima and minima of the surface upcrossing's levels refer to the connected components (isolated regions or disjoint clusters) at these levels, and the expected Euler-Poincaré characteristic at high thresholds, derived in Eq. (5.23) of

the skew$-t$ random field approximates the number of these local maxima or minima. Since the expected Euler-Poincaré characteristic describes the roughness of the surface (small-scale features), it might also be influenced by the measurement errors related to the uncertainty of the measurement instrument device (systematic error). When seeing Fig. 8.5, there are spiky heights located around the contour of the deformed regions, some of them are uncorrelated and they come by chance.
Our interest is to detect the significant levels h including the real hills and valleys that are associated to the mechanical deformation and wear mechanisms. Towards this aim, h should be firstly chosen to control the probability of detecting maxima and minima that are obtained by chance due to the measurement error (uncertainty levels), which are not significant. These maxima and minima are referred to as the extreme values and they are located at very high levels, i.e.; they are concentrated at the tail probability $\mathbb{P}[Y_{max} \geq h]$ or $\mathbb{P}[Y_{min} \leq h]$ of the skew$-t$ random field (see corollary 5.5.1).

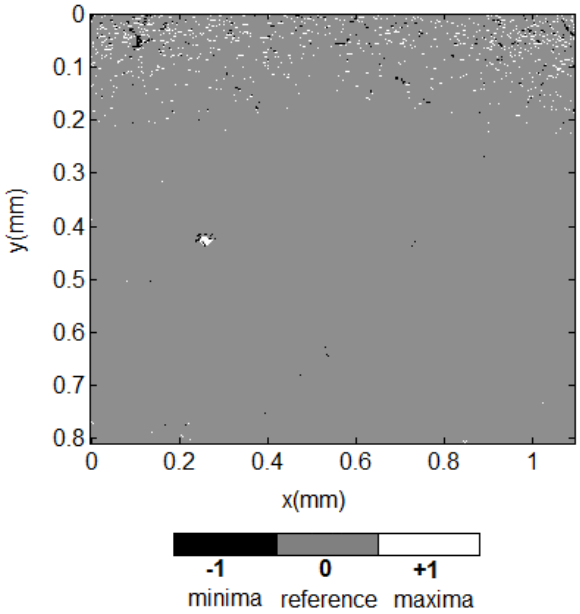

Figure 8.9: Extreme values (maxima and minima) of one sample at wear process time 13×10^6 cycles. The white blobs in the image correspond to the excursion set above the threshold $h_{max} = 0.25\mu m$, as well the dark blobs in the image are the excursion set below the threshold $h_{min} = -0.13\mu m$.

Two thresholds were calculated such that the tail probability is no more than $\varepsilon = 5\%$, which are $h_{max} = 0.25\mu m$ and $h_{min} = -0.13\mu m$. The excursion sets $E_{h_{max}}$ and $E_{h_{min}}$ obtained at h_{max} and h_{min}, respectively, are combined in one single set (see Fig. 8.9), denoted $E_{(h_{max},h_{min})}$, and expressed as:

$$E_{(h_{max},h_{min})} = \begin{cases} +1, & if\, x \in E_{h_{max}} \\ -1, & if\, x \in E_{h_{min}} \end{cases} \tag{8.5}$$

Table 8.2: Roughness parameters of one worn sample topography

Worn UHMWPE	$S_q(nm)$	S_{sk}	S_{ku}
Before threshold	34.5	4.41	111.81
After threshold	21.8	1.17	9.4

This implies that most of the hills and valleys above and below the detected thresholds come by chance and correspond to error of measurement, and the probability of detecting real hills or valleys will be less than 5%. The roughness component after rejecting these levels is illustrated in Fig. 8.10(a). Nevertheless, the model's parameters will change (see Tab. 8.2) but the topographic roughness could always be considered and represented as a skew$-t$ random field as can be seen in the Q-Q plot of the heights distribution (Fig. 8.10(b)), and the fit between the analytical and empirical LKCs (Fig. 8.11).

Let h_{hills} and $h_{valleys}$ be the levels including the real hills and valleys of one sample shown in Fig. 8.10(a). At this time, the local maxima and minima that are concentrated at the tail probability will correspond to the real hills and valleys, and their levels are estimated using the Euler-Poincaré characteristic of the skew$-t$ random field at the high thresholds, such that $h_{hills} = 0.053\mu m$ and $h_{valleys} = -0.025\mu m$ (see Fig. 8.12), where the excursion set $E_{(h_{hills},h_{valleys})}$ at both detected hills h_{hills} and valleys $h_{valleys}$ is expressed using the same argument given in equation (8.5).

8.4.2 Comments

One can notice that the predominant features on the surface at this stage of wear process, $t = 13 \times 10^6$ cycles, are the valleys and pits. Their area is also more important compared to the area of the detected hills. The number and the size of the holes refer to a fatigue wear mechanism due to the loss of the UHMWPE particles after frequent abrasive and adhesive wear mechanisms on the UHMWPE surface [GWG+08]. Furthermore Fig. 8.10(a) shows that the single peak near the global maxima has been removed although it has a significant spatial size. In fact, this maxima is not related to the worn surface but it results from the transfer of the materials of the metal-back surface in contact with the UHMWPE, yielding a maxima height value (anomaly), when measured by the optical devices, due to the maximum reflection of the light from that region.

8.4.3 Wear analysis induced by the statistical analysis of surface roughness

The significant upcrossing levels that include the surface hills and valleys were estimated (Fig. 8.13) over the wear time ($0-19\times10^6$ cycles) for one sample selected from the latitude 45°. To insure that we measure approximately the same location during the wear process, we marked the chosen samples in a safely way that insures not damaging the samples.

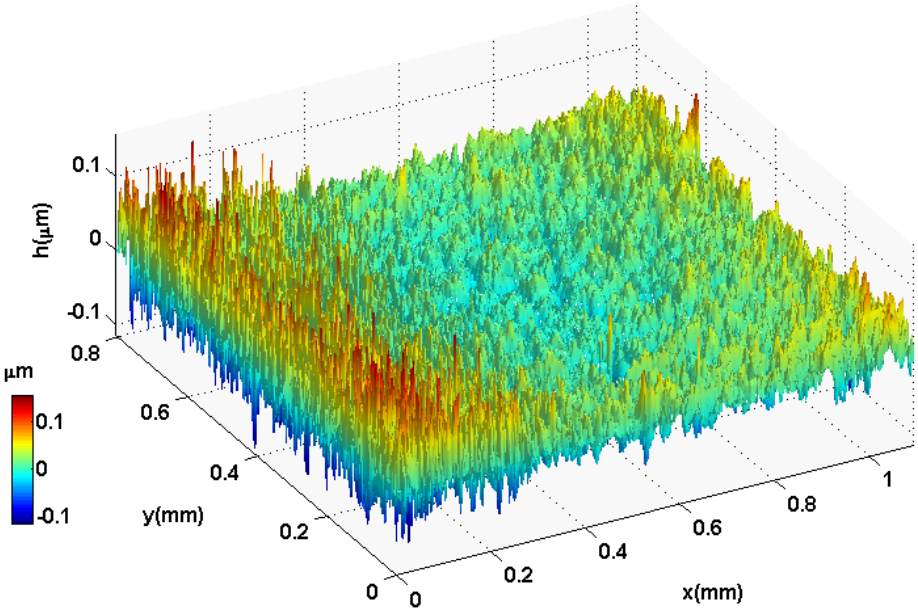

(a)

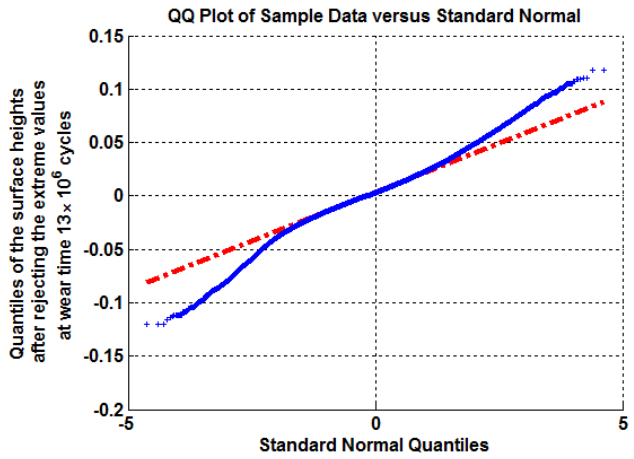

(b)

Figure 8.10: (a) Surface roughness component after rejection of the extreme height levels. (b) The quantile-quantile plot of the heights in (a) versus the normal distribution. The random heights are always positively skewed with skewness value $S_{sk} = 1.17$, and kurtosis value $S_{ku} = 9.4$, and rms value $S_q = 26nm$

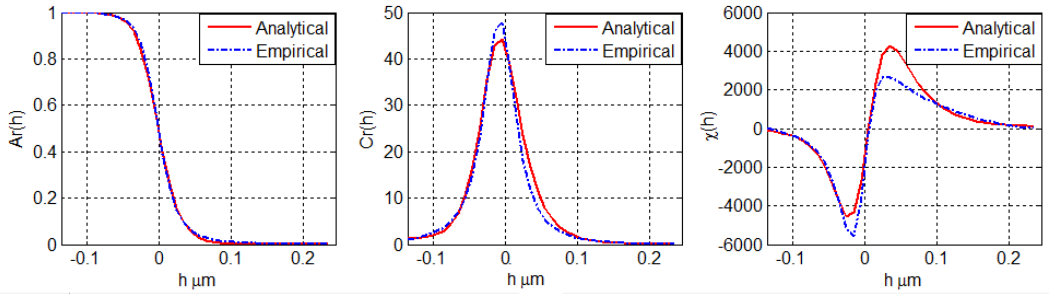

Figure 8.11: Fitting the analytical and empirical LKCs for the real heights illustrated in Fig.(a) restored after threshold, and the skew$-t$ random field with $\nu = 6$ degrees of freedom, skewness index $\delta = 0.5$, and roughness $\lambda = 0.086\mu m^{-2}$.

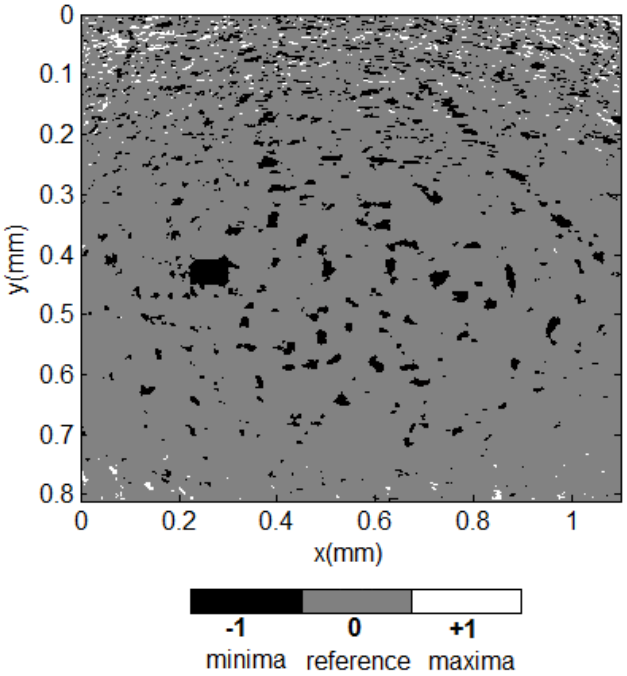

Figure 8.12: Hills and valleys (pits) of one sample at wear process time 13×10^6 cycles. The clusters above the positive threshold h_{hills} are given the value $(+1)$, as well the clusters indicated below the negative threshold $h_{valleys}$ are given the value (-1). The number of the hills $N_{hills} = 508$, the number of pits $N_{valleys} = 1098$

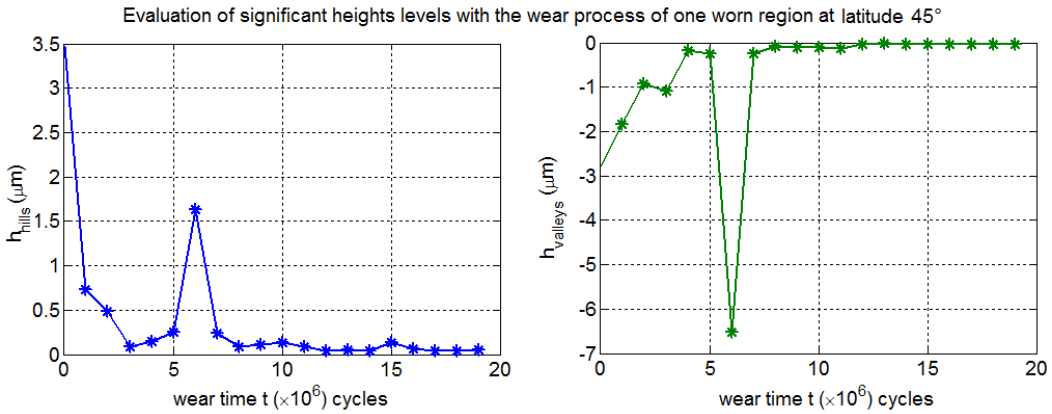

Figure 8.13: Detection of significant upcrossing levels of a sample measured from the UHMPWE at latitude 45° along 19×10^6 cycles of wear time

Fig. 8.13 shows a decrease of the absolute value of these levels during wear time, although some undesired spiky and erratic values were obtained at time 6×10^6 cycles. These results can also refer to a loosening of the UHMWPE materials occurred on the selected sample. Nevertheless, the evolution of these levels can also be used to describe the functional behaviour of the surface if they are weighted by their spatial extent. The spatial extent of the excursion sets $E_{h_{hills}}$, $E_{h_{valleys}}$ was estimated during the wear time by evaluating their mean areas. The functional interpretation of these areas can be explained as follows: The evaluation of the mean area of the hills at level $h_{hills}(t)$ determines the amount of the surface bearing area remaining after a certain depth of material is removed, and the mean area function of the valleys estimated at level $h_{valleys}(t)$ describes the changes of the fluid entrapment or leakage, due to the material's void area changes. Thus, one can computethe difference between the bearing and the void areas multiplied by their detected levels, denoted by $f(t)$, during the wear time in order to express the surface functionality as follows:

$$f(t) = h_{hills}(t) \times Area[E_{h_{hills}(t)}] - |h_{valleys}(t)| \times Area[E_{h_{valleys}(t)}] \tag{8.6}$$

where

$$Area[E_{h_{hills}(t)}] = A \int_{h_{hills}(t)}^{\infty} p(y)dy, \quad Area[E_{h_{valleys}(t)}] = A \int_{\infty}^{h_{valleys}(t)} p(y)dy \tag{8.7}$$

where $A \cong 1mm^2$ is the total area of measurement, and $p(y)$ is the probability density function of the surface heights. The evolution of the function $f(t)$ (see Fig. 8.14) shows significant variability of the surface roughness during the period $0 \times 10^6 - 10 \times 10^6$ cycles, which behaves alternatively and it is correlated with the predominant wear mechanisms being occurred on the UHMWPE surface at this stage of wear time [WEP+98]. Different types of wear mechanisms can be depicted on Fig. 8.14. At the beginning of the wear process until $t = 3 \times 10^6$ cycles, an abrasive

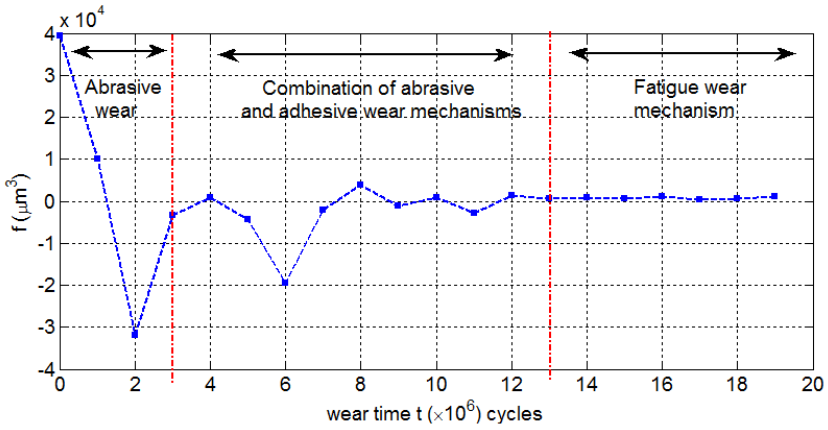

Figure 8.14: Evolution of the difference between the bearing area and the void area at their significant levels with wear time on one sample example of the UHMWPE surface at 45°

wear mechanism, mainly, occurs. The abrasive wear at this stage results from cutting (eroding) the hills of the rough UHMWPE sample, (see Fig. 8.15), due to the direct contact with a smooth, rigid surface (metal-back component). Thereafter, during the time range between $t = 4 \times 10^6$ cycles and $t = 10 \times 10^6$ cycles, the function $f(t)$ behaves alternatively due to the effects of the both abrasion and adhesion wear mechanisms [GWG+08]. The abrasion mechanism at this time is mainly due to the wear particles removed from the surface and deposited in the liquid will abrade randomly the surface during the liquid circulation (see Fig. 8.16 as examples), whereas the adhesive mechanism results from the transfer of some materials between the joined surfaces. From 10×10^6 cycles, the variability of the roughness indicated by the function $f(t)$ becomes negligible where a fatigue mechanism might govern the surface attribute. Nevertheless, the function $f(t)$ can not give a clear physical interpretation of the surface behaviour, and further expansions are required.

8.5 Results and discussion

8.5.1 Worn regions of the UHMWPE surface at the latitude 45°

In order to increase the certainty of the results, and to describe globally the wear mechanism around the most worn regions on the UHMWPE surface, which are located, in this case study, at latitude 45°, five samples were measured and tested at different positions as discussed in 7.2.1.
The significant levels (Fig. 8.17) included the hills and valleys were estimated, following the same arguments in section 8.4, on the five selected samples of the UHMWPE surface at 45° latitude, over the approximative angles $0°, 45°, 90°, 180°, 175°$.

The function $f(t)$ in equation (8.6), that computes the difference between the bearing and the void areas of the surface multiplied by their significant height levels

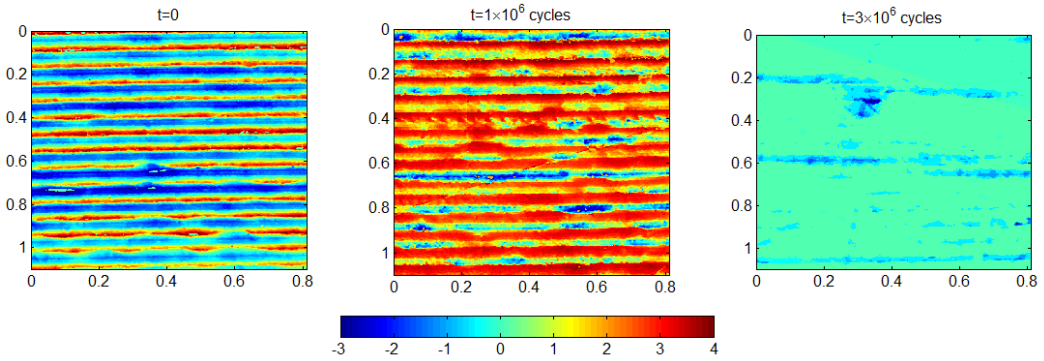

Figure 8.15: 3D height maps of one worn sample of the UHMWPE cup at 45° during wear time, restored after thresholding. The left figure corresponds to the zone at $t = 0$, and the center one is the surface sample at $t = 1 \times 10^6$ wear cycles, while the right surface is measured at $t = 3 \times 10^6$ cycles.

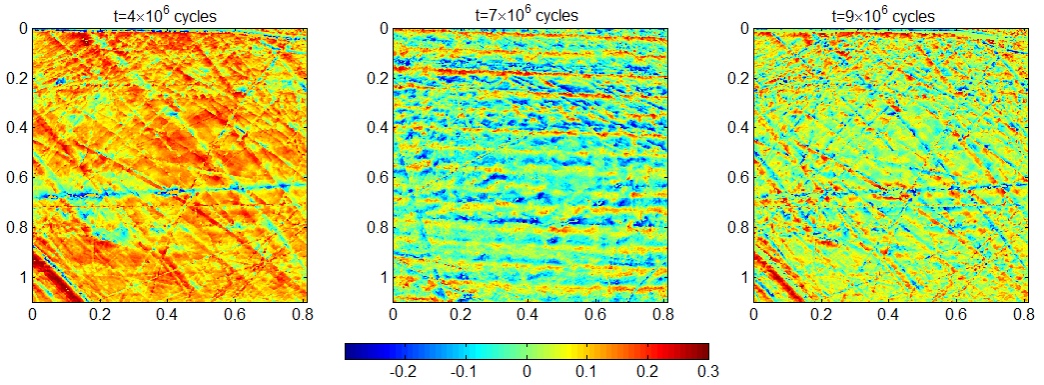

Figure 8.16: 3D height maps of one worn sample of the UHMWPE cup at 45° during wear time, restored after thresholding. The left figure corresponds to the zone at $t = 4 \times 10^6$, and the center one is the surface sample at $t = 7 \times 10^6$ wear cycles, while the right surface is measured at $t = 9 \times 10^6$ cycles.

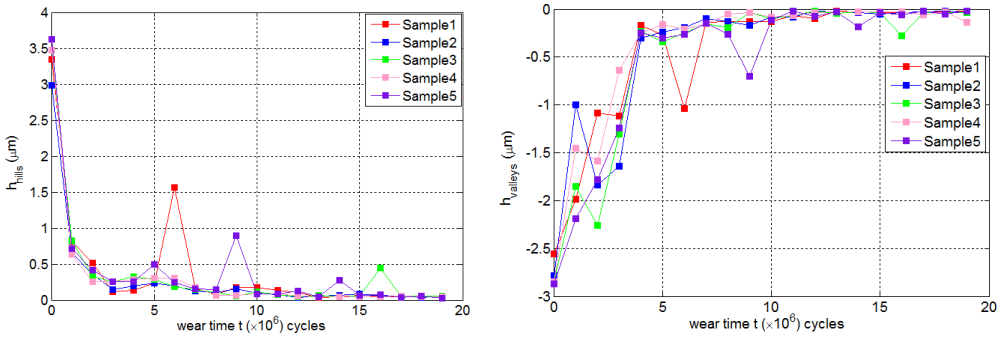

(a) (b)

Figure 8.17: Significant hills and valleys levels versus wear time for 5 UHMWPE samples at latitude 45°. (a) hills levels at h_{hills}. (b) valleys levels at $h_{valleys}$

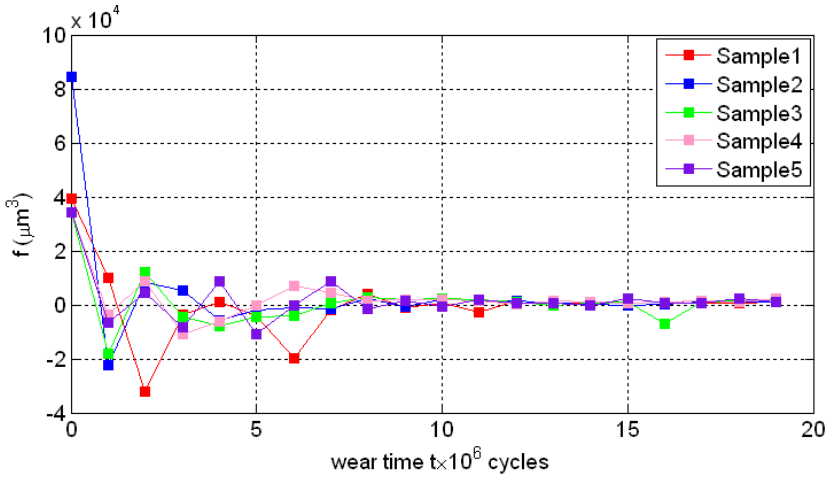

Figure 8.18: The evolution of the difference between the bearing and the void volumes with wear time on five samples of the UHMWPE surface at 45°

during wear time, is evaluated for the selected 5 samples (Fig. 8.18) in order to describe the functional behaviour of the surface at the 45° latitude. This function demonstrates, as *a priori* assumption, a homogeneous functional behaviour over the different samples measured at the 45° latitude. At the first 10×10^6 wear cycles, the function shows fast variations due to a significant evolution of the surface roughness, contrary to the wear periods after 10×10^6 cycles where a fatigue mechanism governs the surface and the roughness evolution becomes slow with the time. Nevertheless, more tests should be performed on different UHMWPE specimen to insure this assumption.

8.5.2 Quantitative comparison between worn regions at 45° and 100° latitudes

A quantitative comparison is performed between regions selected from two different latitudes at 45° and 100° of the convex side of the UHMWPE component. Eight samples have been selected for the tests, four samples belong to the region located at 45°, and the other ones were measured from the region located at 100°. The evolution of the surface upcrossing's levels h_{hills} and $h_{valleys}$ for each sample (Fig.8.19) illustrates the non-homogeneous behaviour of the roughness throughout the UHMWPE latitudes, and hence the non homogeneity of the wear mechanisms. The regions at 100° undergo less wear if compared with the ones at 45° latitude. The results in Fig.8.19 show that the levels slightly alternate around $h_{hills} = 3\mu m$ and $h_{valleys} = -2.7\mu m$, respectively, where the surface roughness model does not exhibit significant changes, conversely to the regions at 45° latitude. These results are convenient with the *in-vitro* experimental test results drawn in [GBF11].

8.6 Conclusion

Firstly, this chapter was concerned on applying the linear mixture Gaussian$-t$ random field model on the UHMWPE surface after a machining process. This random field model enabled estimating the large-scale and small-scale features on the surface. Furthermore, the model shows that the Gaussian hills/valleys are mostly concentrated at low height levels, where at high levels, the hills/valleys follow another model refereed to as t random field. When the UHMWPE get worn, the wear process affects the whole scale-space structures (hills/valleys) dependently, so the separation between these scales becomes complicated. Thereby, the second step is focused on modelling the small-scale structures of the worn rough UHMWPE surface. The skewness and kurtosis parameters are the most significant parameters that have changed during the wear process. Thus, the skew$-t$ random field was suggested to predict the functional hills/valleys related to wear. Notice that we can assume that the small-scale structures for both machined and worn UHMWPE surface are modelled by the skew$-t$ random field since the later is an extension of the t random field including the skewness concept to the heights distribution function. The results illustrated in this application part were obtained during 20×10^6 cycles of wear, on samples selected from two longitudes. These results demonstrate the importance of the functional parameters such as hills/valleys level's heights and their mean area in describing the wear mechanisms and the functional behaviour of the surface during the wear. In this chapter, we focused on the intrinsic volumes (LKCs) and precisely Euler-Poincaré characteristic for estimating the roughness evolution of the surface. Even if the surface model could change from one material to another, the strategy given in this chapter is applicable for any surface.

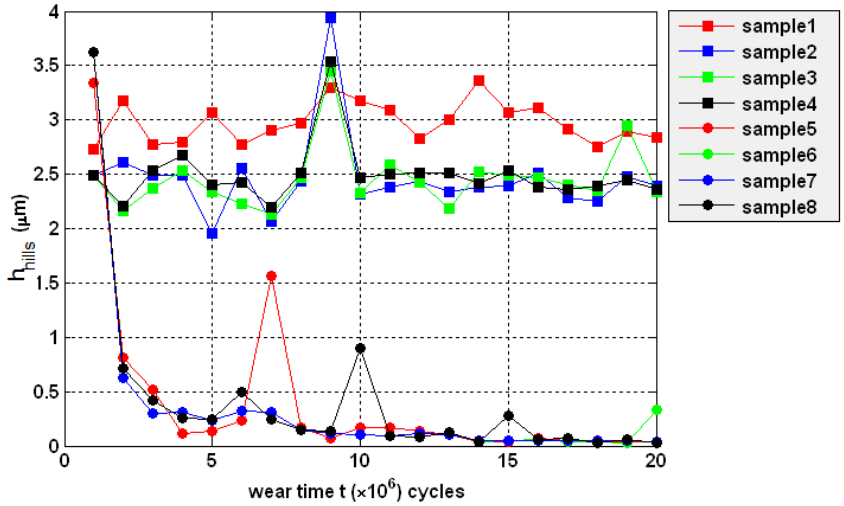

(a)

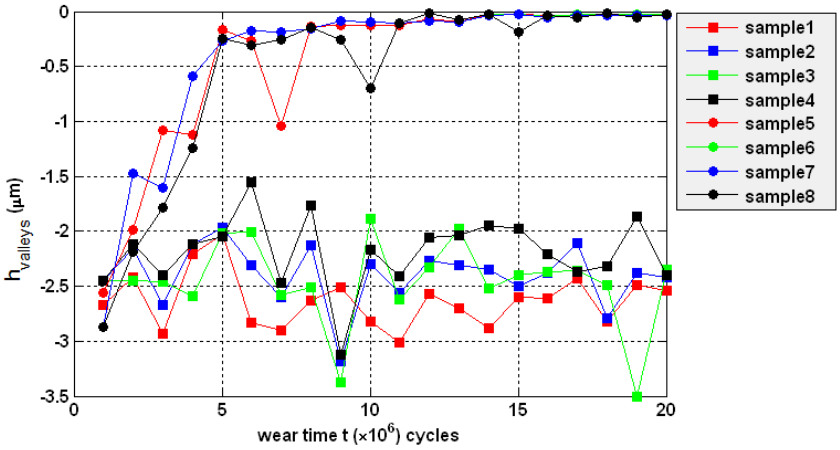

(b)

Figure 8.19: A quantitative comparison between the hills and valleys levels of the UHMWPE samples located at latitudes 45° latitude, labelled by ● , and 100° latitude, labelled by ■ , showing different degrees of wear. (a) hills levels. (b) valleys and pits levels.

Part V

GENERAL CONCLUSION AND FUTURE WORK

Chapter 9

Space−Time Skew−t Random Fields

Contents

9.1 Introduction 97
9.2 Preliminaries 98
9.3 Definition 98
9.4 Expectations 99
9.5 Simulation example 100
9.6 Application 101
9.7 Conclusion 105

This chapter includes some work in progress and further investigations that have been realized later and they have not been finished yet. So, we suggested to put all those investigations in this concluding part of dissertation.

9.1 Introduction

We consider a class of real-valued random fields that appears throughout the modelling of spatio-temporal phenomena, such as the application provided in this thesis, modelling the surface roughness topography when the material undergoes wear and mechanical contact processes over time, or in other applications such as those in physical oceanography [AMR96], and brain imaging [SSSW03]. For example, space-time random fields have been used to describe the time-evolution of the spatial parameter of the observed measurements and to predict future values [Ma07].

In the previous chapters, a spatial model of the roughness topography has been realized by the skew−t random fields. An extension of this model can be considered to include the temporal changes of the surface features, such as the temporal covariance, and the temporal skewness functions. So, this chapter concerns on introducing the skew−t random field in space and time, and in deriving the LKCs of the excursion sets, towards their potential use in practice.

9.2 Preliminaries

Let $G_0(\boldsymbol{x}), G_1(\boldsymbol{x}), ..., G_\nu(\boldsymbol{x})$, $\boldsymbol{x} \in S$ where S is a compact non-empty subset of $\mathbb{R}^N$, be a set of i.i.d. Gaussian random fields, so each has a mean zero, and covariance function $C(\boldsymbol{x}_1, \boldsymbol{x}_2)$, $\boldsymbol{x}_1, \boldsymbol{x}_2 \in S \subset \mathbb{R}^N$, with a second order spectral moment matrix $\boldsymbol{\Lambda}_{\boldsymbol{x}}$. Then, the skew−$t$ random field, $Y(\boldsymbol{x})$, has been defined as extension of the known t random field including the concept of skewness, as discussed in chapter 5, such that:

$$Y(\boldsymbol{x}) = \frac{\delta|z| + \sqrt{1-\delta^2}Z(\boldsymbol{x})}{\left(\sum_{i=1}^{\nu} G_i^2(\boldsymbol{x})/\nu\right)^{1/2}} \tag{9.1}$$

where $\delta \in (-1, 1)$ is a skewness index, $z \sim Normal(0, 1)$ is a normal random variable independent of $G_0, G_1, ..., G_\nu$ components.
It can be noticed immediately that the spatio-temporal skew−t random field might be realized from the i.i.d. centered spatio-temporal Gaussian random field components each has mean zero, and covariance function $C(\boldsymbol{x}_1, \boldsymbol{x}_2; t_1, t_2)$, with $\boldsymbol{x}_1, \boldsymbol{x}_2 \in S \subset \mathbb{R}^N$ and $t_1, t_2 \in \mathbb{R}$.

9.3 Definition

Let $G_0(\boldsymbol{x}, t), ..., G_\nu(\boldsymbol{x}, t)$, $\boldsymbol{x} \in S$ and $t \in T$, be i.i.d. homogeneous, real-valued spatio-temporal Gaussian random fields, each with mean zero, variances $\sigma_{\boldsymbol{x}}^2$ and σ_t^2, and with the second spectral moment matrix $\boldsymbol{\Lambda}_{\boldsymbol{x}} = Var(\partial G_i(\boldsymbol{x}, t)/\partial \boldsymbol{x})$, $i = 0, ..., \nu$, and the second spectral moment $\lambda_t = Var(\partial G_i(\boldsymbol{x}, t)/\partial t)$, for all $i = 0, ..., \nu$. Let Z be a standard normal random variable independent of all G_i, and the temporal skewness function $\delta(t)$ such that $\delta : T \to (-1, 1)$, then a real-valued spatio-temporal skew−t random field is defined at any fixed $\boldsymbol{x}$ and t as follows:

$$Y(\boldsymbol{x}, t) = \frac{\delta(t)|Z| + \sqrt{1-\delta^2(t)}G_0(\boldsymbol{x}, t)}{\left(\sum_{i=1}^{\nu} G_i^2(\boldsymbol{x}, t)/\nu\right)^{1/2}} \tag{9.2}$$

where ν is the degree of freedom and it is considered as constant over the time, with respect to the aforementioned condition $\nu \geq N$ as discussed in chapter 5. In more general case, the degree of freedom could be also assumed to change temporally, so the shape (peakedness and tail-weight) of the marginal distribution function will change with time.
The next section concentrate on calculating the Lipchitez-Killing curvatures (LKCs) and the expected Euler-Poincaré characteristic function of the excursion sets of the spatio-temporal skew−t random field in one simple case proposed for the spatial space parameter space defined by rectangles of $\mathbb{R}^N$.

9.4 LKCs and the expected Euler-Poincaré characteristic of the space−time excursion sets

Let consider the subset S is a rectangle of the form $S = \prod_{i=1}^{N}[0, S_i]$ in $\mathbb{R}^N$, and a time interval $T = [t_{min}, t_{max}] \subset \mathbb{R}$. Then, the Riemannian space induced by the spatio-temporal Gaussian components on the product space $S \times T$, will be equipped with a Riemannian metric defined by the variogram of the first order partial derivatives of the Gaussian random field components, i.e., $\mathbb{E}[\partial G_i/\partial \boldsymbol{s}_1 \partial G_i/\partial \boldsymbol{s}_2]$ with $\boldsymbol{s}_1, \boldsymbol{s}_2 \in (S \times T)$.

For Gaussian and Gaussian-related random fields, it was shown [AT07] that the $j-$th dimensional LKCs for the aforementioned products of the Riemannian space induced by such random fields, for any $j \geq 0$, can be derived using Hadwiger's theorem [Had57], as:

$$\begin{aligned}\mathcal{L}_j(S \times T) &= \sum_{i=0}^{j} \mathcal{L}_i(S)\mathcal{L}_{j-i}(T) \\ &= \mathcal{L}_j(S) + |T|\mathcal{L}_{j-1}(S)\end{aligned}$$

where $|T|$ is the length of the temporal interval T.

In the following, a simple case will be discussed which suggests that: **Firstly**, the spatio-temporal covariance function, of each Gaussian random field, is stationary and separable such that:

$$C(\boldsymbol{x}_1, \boldsymbol{x}_2; t_2, t_1) = C_x(|\boldsymbol{x}_1 - \boldsymbol{x}_2|)C_t(|t_1 - t_2|) \tag{9.3}$$

where C_x and C_t are positive-definite functions, with variances σ_x^2 and σ_t^2, respectively, and with second order spectral moments $\boldsymbol{\Lambda}_{\boldsymbol{x}}$, λ_t, respectively.

Note: the assumption that the spatio-temporal covariance function $C(\boldsymbol{x}, t)$ is separable means that the first order temporal and spatial partial derivatives of each Gaussian random field component $G_i, i = 0, ..., \nu$ are uncorrelated, i.e., $\mathbb{E}[\partial G_i/\partial \boldsymbol{x} \partial G_i/\partial t] = 0$, and so for Y.

Secondly, the skewness function will be considered invariant with time, i.e.; $\delta(t) = \delta$, so the spatio-temporal effects of the skew$-t$ random field are all restricted to the covariance function of its Gaussian components, or equivalently the second order spectral moments.

Under the previous assumptions, and the result given in equation (3.16), chapter 3, the $j-$th dimensional LKCs of Y on $S \times T$ can be expressed as:

$$\mathcal{L}_j(S\times T) = \sigma_{\boldsymbol{x}}^{-j} \sum_{J \in \mathcal{O}_j} \det(\boldsymbol{\Lambda}_{\boldsymbol{x}_J})^{1/2} vol_j(J) + \frac{\lambda_t^{1/2}(t_{max} - t_{min})}{\sigma_t \sigma_x^{j-1}} \sum_{J \in \mathcal{O}_{j-1}} \det(\boldsymbol{\Lambda}_{\boldsymbol{x}_J})^{1/2} vol_{j-1}(J) \tag{9.4}$$

where $\mathcal{O}_j$ is the $\binom{N}{j}$ elements of $\partial_j S$ and J are as mentioned in chapter 3.

Using the general formula in equation (3.10), the expected Euler-Poincaré charac-

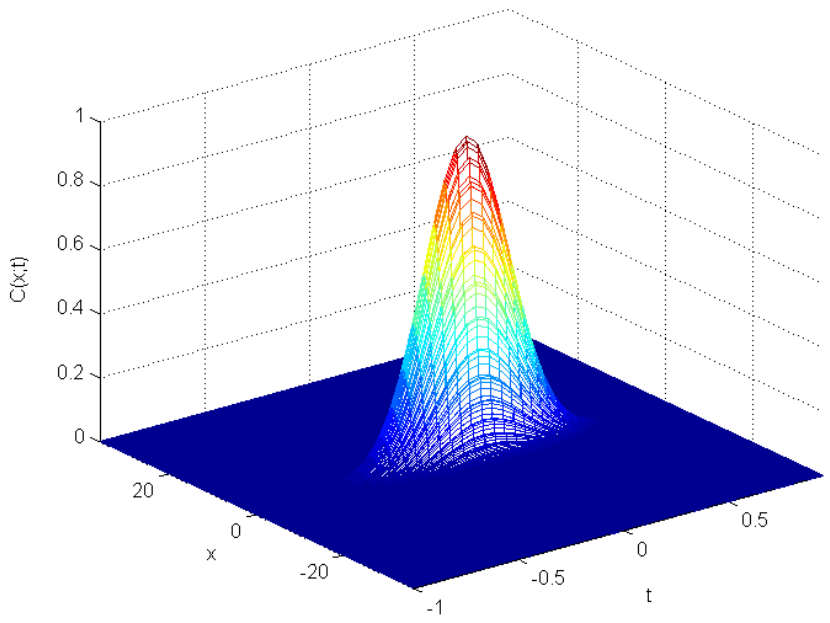

Figure 9.1: A space−time separable covariance function $C(x,t)$ of exponential form with $\sigma_x^2 = 1$, $\sigma_t^2 = 1$, and $\boldsymbol{\Lambda_x} = 9 \times 10^3 I_x$, and $\lambda_t = 40$.

teristic of the spatio-temporal skew−t excursion sets can be expressed as:

$$\mathbb{E}[\chi(Y, S \times T)] = \sum_{j=0}^{dim(S\times T)} \mathcal{L}_j(S \times T)\rho_j^{ST}(h) \tag{9.5}$$

where $dim(S \times T) = N + 1$, and $\rho_j^{ST}(h)$, for $j = 0, ..., N + 1$, are the EC densities for the skew−t random field derived implicitly in chapter 5, theorem 5.4.1.

9.5 Simulation example

This section illustrates simulation example of a spatio-temporal skew−t random field with 5 degrees of freedom and fixed skewness $\delta = 0.5$, for $N = 2$. The field is generated using i.i.d. Gaussian random fields with separable spatio-temporal covariance function of the exponential form:

$$C(x;t) = \sigma_x^2\sigma_t^2 e^{-\boldsymbol{\tau_x}^t \boldsymbol{\Lambda_x} \boldsymbol{\tau_x}} e^{-\tau_t^2 \lambda_t} \tag{9.6}$$

where $\tau_{\boldsymbol{x}}$, $\tau_{\boldsymbol{t}}$ reefer to the spatial and temporal differences $(\boldsymbol{x}_1 - \boldsymbol{x}_2)$, $(t_1 - t_2)$, respectively (see Fig. 9.1). All the space-time Gaussian random fields are simulated on time interval $[0, 1]$ and spatial interval $[0, 0.2]^2$ of 100×100 points. The temporal and spatial Gaussian covariance kernels are chosen such that $\lambda_t = 0.01$ and $\boldsymbol{\Lambda_x} = 10^3 \times I_2$. Then, the spatio-temporal skew−t random field is generated using the

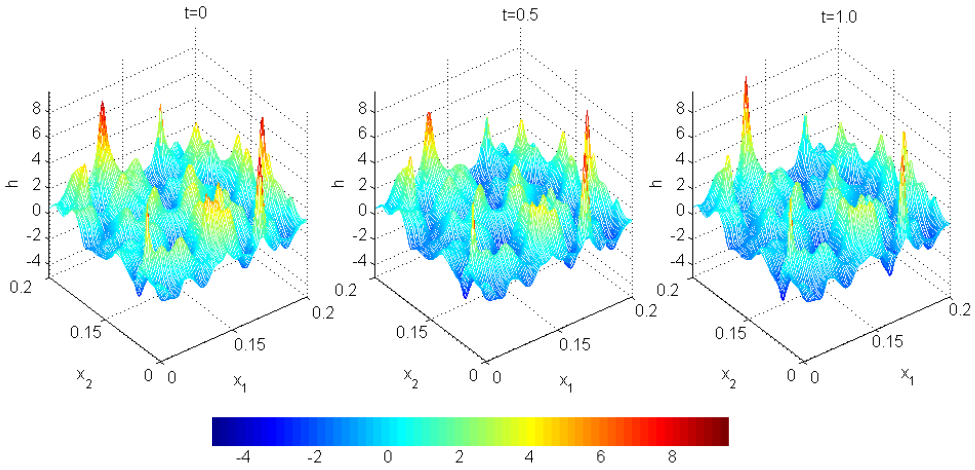

Figure 9.2: A synthesized spatio-temporal skew$-t$ random field of 5 degrees of freedom, and fixed skewness $\delta = 0.5$ at different periods. (a). at $t = 0$, (b) at $t = 0.5$, and (c) at $t = 1$.

definition given in (9.2) for skewness index $\delta = 0.5$ and $\nu = 5$ degrees of freedom. The results are illustrated in Fig. 9.5 for $t = 0$, $t = 0.5$, and $t = 1$, where Fig. 9.3 represents the evolution of the spatio-temporal skew$-t$ random field over all time and space. The expected Euler-Poincaré characteristic function is calculated for the spatio-temporal skew$-t$ random field and illustrated in Fig. 9.4(a) with the simulated ones computed at each time. In Fig. 9.4(b), the simulated Euler-Poincaré characteristic is illustrated as a function of time t and height levels h in order to show the invariance behavior of the spatial parameters with the time due to the separability assumption.

9.6 Application

An interesting application of the space$-$time random fields can be derived from the need to predict the evolution of the surface roughness variability during wear simulation process, without the need to do further experimental tests.
The spatiotemporal Euler-Poincaré characteristic is estimated over 19×10^6 cycles, during wear process, from ones sample at the 45° latitude of the UHMWPE (Fig. 9.5). As can be seen from the evolution of the spatio-temporal Euler characteristic function that the variation of the spatial roughness, described by the matrix Λ_x, depends on the wear cycles, which can be noticed through the variations of its width according to the surface heights. Furthermore, the function exhibits changes in its symmetry, that means the skewness parameter changes with time. The skewness variability during wear time $\alpha(t) = \delta(t)/\sqrt{1-\delta^2(t)}$ (see Fig. 9.6), becomes a significant characteristic function that interprets the effect of the wear process on the surface roughness functionality as discussed in chapter 8. Consequently, the separa-

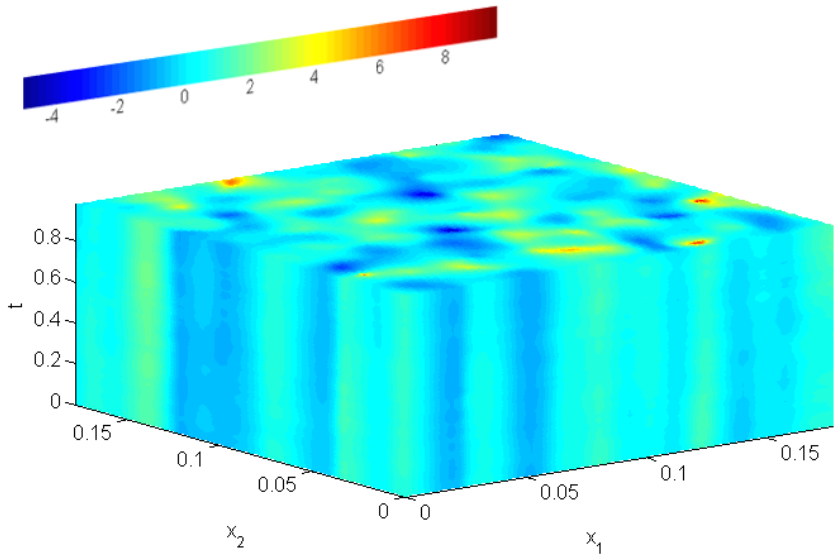

Figure 9.3: Spatio-temporal skew−t random field with 5 degrees of freedom and skewness index $\delta = 0.5$.

bility assumption will not be valid in this case, where the effect of the wear process on the spatial features of the surface roughness is time dependent, and hence, further development are required to well establish the space-time skew−t random field, and the LKCs of its excursion sets, taking into consideration the non-separability assumption. We suggested a regression method in order to model the temporal evolution of the skewness index, estimated from the skew−t random field at each time, at the 45° latitude of the UHMWPE surface (see Fig.9.7). The method aims at finding the best-fitting skewness index values α through a least squares regression in a polynomial function $p(t)$ of n degrees such that:

$$p(t) = p_1 t^n + p_2 t^{n-1} + ... + p_{n+1} \tag{9.7}$$

where t is a variable indicating the time (number of cycles per second), and $\{p_i\}_{i=1,...,n+1}$ are the polynomial coefficients. The fitted α represented in the solid line in Fig.9.7 is produced using the regression method for k samples (k=5) as inputs as follows:

$$\frac{1}{k}\sum_{j=1}^{k} \alpha^{(j)}(t) = p(t) + e(t) \tag{9.8}$$

where $\alpha^{(j)}(t)$ is the skewness function $\alpha(t)$ of the jth sample, and $e(t) \sim Normal(0, Var(\alpha(t)))$ is the regression error term which is assumed to have normal distribution with zero mean and variance function $Var(\alpha(t))$ (see Fig.9.8). The best-fit is obtained for a polynomial of 6 degrees. Thus, the regression model of the temporal skewness index $\alpha(t)$ is expressed as:

$$\alpha(t) = 3.8 \times 10^{-5} t^6 - 0.002t^5 + 0.055t^4 - 0.65t^3 + 3.74t^2 - 8.59t + 0.92 \tag{9.9}$$

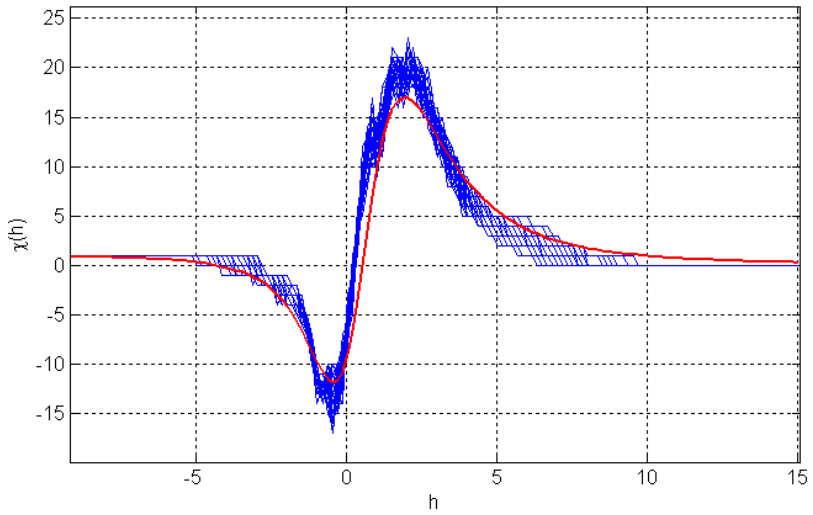

(a)

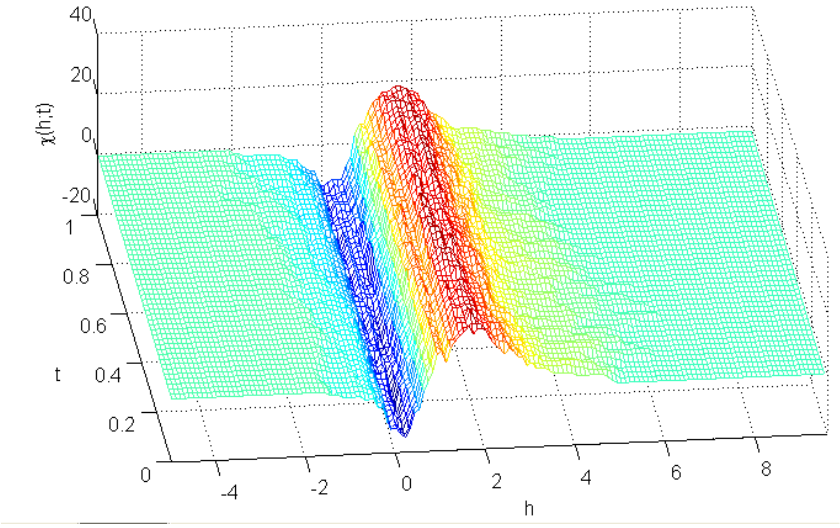

(b)

Figure 9.4: (a) and (b) illustrate the Euler-Poincaré characteristic for the synthesized spatio-temporal skew$-t$ random field estimated at each time $t \in [0, 1]$. The red line in Fig. (a) illustrates the analytical Euler-Poincaré characteristic for the spatio-temporal skew$-t$ random field on the space $S \times [0, 1]$ with $S = [0, 0.2]^2$.

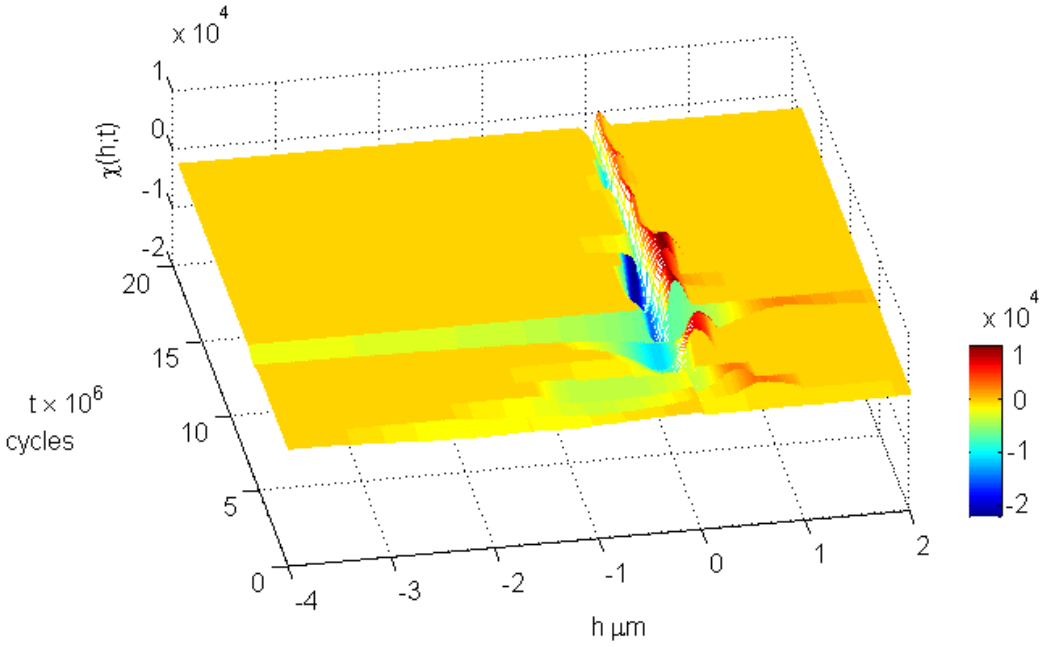

Figure 9.5: The empirical spatio-temporal Euler-Poincaré characteristic estimated, from one sample topography of the UHMWPE, over $t = 0, ..., 19 \times 10^6$ cycles of wear simulation process at each 1×10^6 cycles.

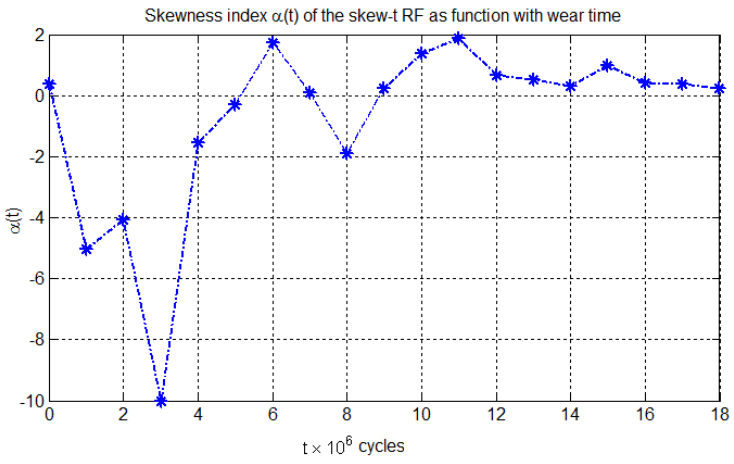

Figure 9.6: Estimation of the skewness index variability $\alpha(t) = \delta(t)/\sqrt{1-\delta^2(t)}$ of the skew−t random field during wear time simulation from one sample of the UHMWPE component at 45° latitude.

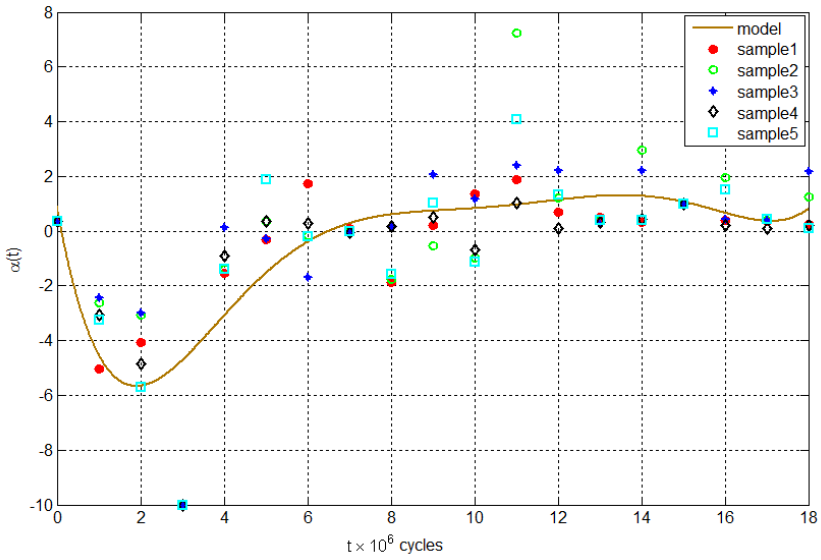

Figure 9.7: Illustration of the regression method to fit the skewness index α in a polynomial of 6 degrees. The geometric shapes in the figure refer to the estimated skewness α of The skew$-t$ random field for five selected samples of the worn UHMWPE surface located at the 45° latitude. The solid line is the predicted skewness index α by the regression method.

over the worn regions located at 45° latitude. Giving $\alpha(t)$ yields to evaluate $\delta(t) = \alpha(t)/\sqrt{1+\alpha^2(t)}$, one of the spatio-temporal skew$-t$ random field's parameters.

9.7 Conclusion

The space$-$time skew$-t$ random field model is introduced using separable spatio-temporal stationary Gaussian random fields. A simple case is introduced in this chapter by fixing the skewness and the degree of freedom of the spatio-temporal skew$-t$ random field. The Lipschitz-Killing curvatures and the expected Euler-Poincaré characteristic are derived for this simple case. However, using the proposed spatio-temporal random field in practice requires go far from the simple case and assume that the skewness index and the degree of freedom are variant with the time. Furthermore, the separability assumption does not take into consideration the interactions between spatial and temporal features. Notice that the LKCs given in equation (9.4) will change since the spectral moments can not be separated between space and time. A practical example on the UHMWPE surface in Fig.9.5 shows by the evolution of the spatio-temporal Euler-Poincaré characteristic function that the surface exhibits high roughness with alternative and fast variations at the first 12×10^6 cycles of the wear time, so that the spatio-temporal model of the surface topography is of non-homogeneous nature, whereas after 12×10^6 cycles the roughness is significantly decreased, and the model of the worn surface exhibits isotropic

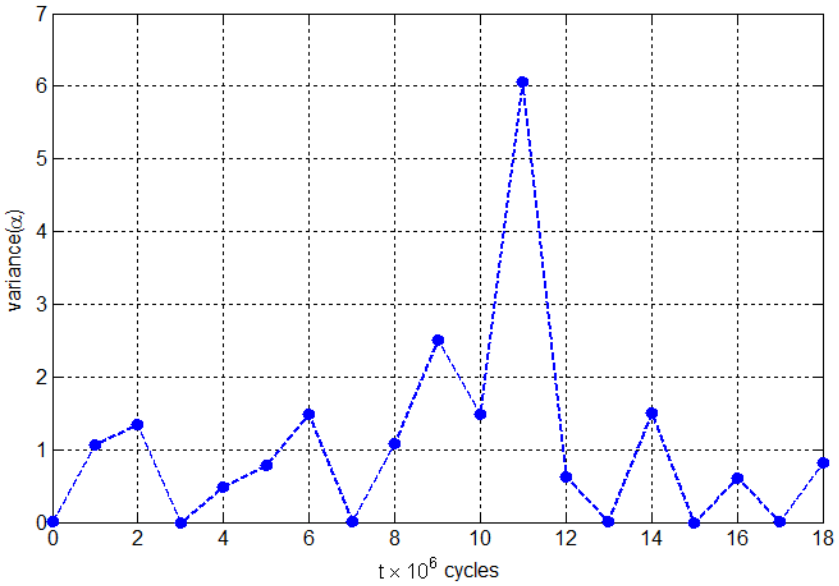

Figure 9.8: Illustration of the variance of the error term $e(t)$ of the predicted skewness function $\alpha(t)$.

and homogeneous behaviour throughout the periods 12×10^6 cycles until 19×10^6 cycles. Also in this chapter, we introduced a regression method for predicting the temporal evolution of the skewness parameter $\alpha(t)$ of the spatio-temporal skew−t random field over the regions at 45° latitude.

Chapter 10

Conclusion and future work

10.1 General Conclusion

This Ph.D. thesis has focused on a theoretical framework driven by the random field models that has been used in many scientific applications, and more specifically in the ones related with rough engineered surfaces. A bibliographic background about the surface roughness metrology, and the most common approaches used to represent and characterize the topography of rough surfaces were summarized within the first part of this dissertation. Due to the random nature of rough surfaces, the topography is represented by the theory of random fields. A random field model defines the joint distribution function of the heights, the geometry and the topological properties of these later with their neighbours, which can be quantified, using the integral geometry, via the excursion sets of the random fields. The basic theoretical background of random fields and the geometric properties of their excursion sets have been reported in the second part of this thesis. The analytical formulae of the intrinsic volumes for a random field is used for fitting the model with the real surface, for estimating its parameters, and for the surface roughness analysis.

The main theoretical developments, in the third part of the manuscript, were concerned on the integral geometry of random fields, due to the lake in the literature in giving the aforementioned formulae for some random fields that have of great interest in practice. We, firstly, derived the analytical formulae of the intrinsic volumes, or Lipschitz-Killing curvatures (LKCs), of the two-dimensional excursion sets of a mixture model defined by the linear combination of a Gaussian random field and a $t-$field. The motivation comes from the fact that surface topography can be partitioned into two components, one with a large-scale structure and narrow roughness which is modelled by Gaussian random fields, and the second with small-scale features and heavy-tailed distribution which are modelled by the $t-$field. The LKCs have been derived based on Morse theory in the case that the Gaussian$-t$ random field is isotropic, called in this case by Minkowski functionals. We proved by means of the expected Euler-Poincaré characteristic that the behaviour of the local maxima and minima of the mixture random field depends on two basic factors, the degree of freedom ν, and mainly on the scale factor β of the $t-$field that control the non-Gaussianity behaviour of the surface heights. Secondly, the analytical formulae of the LKCs have been derived for the skew$-t$ random field in the $N-$dimensional Euclidean space. The skew$-t$ random

field was introduced as an extension of the $t-$field including the concept of the skewness to the height's distribution. Thus, the small-scale features, defined by the maxima and the minima (hills and valleys) of a rough surface, can be represented and characterized by the skew$-t$ random field, and thereby they will behave in asymmetry according to their mean. An asymptotic formulae of the expected number of the hills and valleys was calculated and also expressed in terms of the expected Euler-Poincaré characteristic at high levels. In practice, the later could be considered as a useful technique to estimate the mean number of the hills and valleys which are defined by different confusing ways in surface metrology, or to estimate the significant levels including those small-scale features from the uncertain heights.

A specific application proposed in this thesis was for analysing and modelling the topography of worn rough surfaces, particularly, those involved in the total hip arthroplasty, and known by UHMWPE components. Considering both the medical and the scientific problems related with the wear of the UHMWPE component when the later articulates with other type of materials, it was necessary to understand how the UHMWPE surface gets worn, and which wear mechanisms are mostly predominant. This study would help for an ultimate aim related with improving the quality and the life duration of the artificial hip implants, and improving the manufacturing process. The UHMWPE surface in the non-worn state was modelled by the Gaussian$-t$ random field, so that the small-scale features (hills/valleys) of the surface which diverge from Gaussianity were represented and estimated by the $t-$field, and the large-scale features were assumed to be of a multivariate Gaussian distribution and they are characterized using the covariance function. During the wear process, which has been generated artificially (*in-vitro*) using a hip wear simulator machine, the heights of the UHMWPE surface topography became to behave in asymmetry according to their mean, and led to represent the worn topography by the skew$-t$ random field.

A statistical analysis approach based on the skew$-t$ random field was then proposed to study the evolution of the surface roughness during the wear simulation process, by hierarchically estimating the evolution of the skewness parameter, the evolution of the hills/valleys, their mean area and their significant height's levels during wear time, which indicate the most important characteristics that interpret the wear mechanisms, tribological properties and the functionality during the mechanical contact between the articulating surfaces. The evaluation of these characteristics demonstrated fast and significant variations of roughness at the first $10 \times 10^6 - 12 \times 10^6$ cycles where the roughness evolution tends to be very slow after 12×10^6 cycles due to important fatigue wear mechanism on the surface. During the first $10 \times 10^6 - 12 \times 10^6$ cycles the UHMWPE surface at 45° latitude exhibits an alternative functional behaviour, which was dominantly affected by abrasion and adhesion wear mechanisms. From topological point of view, the excursion sets detected at the significant levels include more holes with significant spatial extent

than peaks (connected components), which implies that the void area is much prominent than the bearing area and yields to low friction and contact influence between the UHMWPE and the metal-back. This concluding result was also illustrated by computing the difference between bearing and void areas multiplied by their significant levels, and by the evolution of the Euler-Poincaré characteristic function in terms of time and heights.
The quantitative comparison between different zones of the UHMWPE surface at 45° and 100° latitudes showed non-homogeneous behaviour of the surface where they demonstrated an important wear on the zones at 45° latitude contrary to 100° latitude. These *in-vitro* experimental results confirm the *ex-vivo* observations on cups from dual mobility concept.

To conclude, the Lipschitz-Killing curvatures (LKCs) of the excursion sets of random fields have three advantages, in practice, for analysing rough surfaces: -firstly they can be used to fit the rough surface geometry with the appropriate random field model, -secondly, some model's parameters can be determined from these characteristic functions, -and finally, the expected Euler-Poincaré characteristic is a robust technique that can be used to control and estimate the surface levels including the hills and valleys, and so for analysis of worn surfaces.

10.2 Future work

There are several possible ideas to extend the work of this thesis, in both theoretical and practical fields. We derived the analytical formulae of LKCs and the mean number of the maxima and minima for both Gaussian$-t$, and skew$-t$ random fields. However, the local size of these maxima and minima (size of each connected component), if combined with the height levels of each one, can increase the robustness of the statistical analysis approach in detecting the significant hills and valleys from the uncertain ones.

A space-time skew$-t$ random field has been introduced in chapter 9 for a work in progress which can be continued in the future. This model can be used to estimate and to predict the spatial and temporal evolution of the surface roughness during the time wear process. In such case, one can estimate an approximate time of the final degradation of the surface without the need to do further wear tests, i.e., the age of the UHMWPE component inside the artificial implant.

The skew$-t$ random field has been defined only over one set of length scales. Thus, further development can be investigated by extending the model to multi-scales using the scale-space approach, and so define a scale-space skew$-t$ random field. In this case, independent and identically distributed scale-space Gaussian random field components will be used to realize the model. Each Gaussian component can be realized by smoothing a Gaussian white noise with a spatial filter over a

range of filter scales related with λ where $\lambda \in [\lambda_1, \lambda_2]$, closely to the space-time case (see chapter 9).
The scale-space approach from a practical point of view enables estimating the location and the scale of the maxima and minima, and can be considered as one solution of how estimating their local size. This can increase the reliability of the statistical analysis approach and also enables the detection of the roughness parameters associated with each scale. Furthermore, the wear process leads to, according to the results shown in this manuscript, a strong anisotropic roughness patterns, that are surely mechanically very important features which could be explored by the rotation scale-space random fields.

For the medical application given in this thesis, the experimental developments have been tested on one UHMWPE specimen. Further experimental tests on more specimens will increase the robustness of the drawn results and conclusions.

Appendices

Appendix A

Lemmas

Lemma A.0.1 ([Adl81]). *Let G be a real-valued centred Gaussian random field with unit variance. Let $\Lambda = Var\,(\partial G/\partial x)$ be the $N \times N$ variance-covariance matrix of its first partial derivatives with elements λ_{ij}, $(i, j = 1, ..., N)$, then,*

(i) $\dot{G} \sim Normal_N(0, \Lambda)$ *independent of* G *and* $\ddot{G}$
(ii) *Conditioning on* G,

$$\ddot{G} \mid G \sim Normal_{N\times N}(-G\Lambda, M(\Lambda))$$

where the elements of $M(\Lambda)$ *are such that:*

$$Cov\left(\frac{\partial^2 G}{\partial x_i \partial x_j}, \frac{\partial^2 G}{\partial x_k \partial x_l} | G\right) = \varepsilon(i, j, k, l) - \lambda_{ij}\lambda_{kl}$$

where $\varepsilon(i, j, k, l)$ *is symmetric in its arguments.*

Lemma A.0.2 ([Wor94]). *The first two derivatives of a χ^2 random field, with ν degrees of freedom, $U = U(x), x \in \mathbb{R}^N$ can be expressed in terms of independent random variables, where the equality $\stackrel{D}{=}$ is equality in law, as follows:*

(i) $\dot{U} \stackrel{D}{=} 2U^{\frac{1}{2}}\boldsymbol{z}$
(ii) $\ddot{U} \stackrel{D}{=} 2(\boldsymbol{P} + \boldsymbol{z}\boldsymbol{z}^t - U\Lambda + U^{\frac{1}{2}}\boldsymbol{H})$

where $U \sim \chi^2_\nu$, $\boldsymbol{z} \sim Normal_N(0, \Lambda)$,$\boldsymbol{P} \sim Wishart_N(\Lambda, \nu - 1)$ *and* $\boldsymbol{H} \sim Normal_{N\times N}(0, M(\Lambda))$, *all independently.*

Lemma A.0.3 ([Wor94]). *The first and second order partial derivatives of the $t-$field $T^\nu = T^\nu(x), x \in \mathbb{R}^N$ with ν degrees of freedom, (at any fixed point x), can be expressed in term of independent random random variables as follows:*

(i) $\dot{T^\nu} \stackrel{D}{=} \nu^{\frac{1}{2}}(1 + (T^\nu)^2/\nu)W^{-\frac{1}{2}}\boldsymbol{z}_1$
(ii) $\ddot{T^\nu} \stackrel{D}{=} \nu^{\frac{1}{2}}(1 + (T^\nu)^2/\nu)W^{-1}\{-\nu^{-\frac{1}{2}}T^\nu(\boldsymbol{Q} - 2\boldsymbol{z}_1\boldsymbol{z}_1^t) - \boldsymbol{z}_1\boldsymbol{z}_2^t - \boldsymbol{z}_2\boldsymbol{z}_1^t + W^{\frac{1}{2}}\boldsymbol{H}\}$

where $T^\nu \sim t_\nu$, $W \sim \chi^2_{\nu+1}$, $\boldsymbol{z}_1, \boldsymbol{z}_2 \sim Normal_N(0, \Lambda)$, $\boldsymbol{Q} \sim Wishart_N(\Lambda, \nu - 1)$ *and* $\boldsymbol{H} \sim Normal_{N\times N}(0, M(\Lambda))$, *all independently.*

Lemma A.0.4. *If $H \sim Normal_{N\times N}(0, M(I)$ then:*

$$\mathbb{E}(det(H)) = \begin{cases} \frac{(-1)^{2j}(2j)!}{2^j j!} & if N = 2j \text{ is even} \\ 0 & if N \text{ is odd} \end{cases} \tag{A.1}$$

Lemma A.0.5 ([Wor94])**.** *Let $H \sim Normal_{N\times N}(0, M)$ and let A be a fixed symmetric $N \times N$ matrix. Then*

$$\mathbb{E}[det(A + H)] = \sum_{j=0}^{\lfloor N/2 \rfloor} \frac{(-1)^j (2j)!}{2^j} detr_{N-2j}(A) \tag{A.2}$$

Lemma A.0.6 ([CW99])**.** *Let $P \sim Wishart(I_N, \nu)$, $H \sim Normal_{N\times N}(0, M)$ are independent, and A be a fixed symmetric $N \times N$ matrix. Let a, b be fixed scalars. Then*

$$\mathbb{E}[det(A + aP + bH)] = \sum_{j=0}^{\lfloor N/2 \rfloor} \frac{(-1)^j}{2^j j!} b^{2j} \sum_{k=0}^{N-2j} a^k \binom{\nu}{k} (2j + k)! detr_{N-2j-k}(A) \tag{A.3}$$

Appendix B

Simulation of Gaussian random fields with isotropic/anisotropic correlation functions

B.1 Orthogonal expansion (Karhunen-Loève expansion)

One of the most important practical aspects in Gaussian modelling and simulation is the orthogonal expansion, or *Karhunen-Loève expansion*, using its covariance function [AT03]. It states that every centred Gaussian random field, $Y(\boldsymbol{x})$, $\boldsymbol{x} \in S$, defined on a compact subset S of $\mathbb{R}^N$ (in the following, S is assumed a rectangle $[0,1]^N$), with a continuous covariance function has an expansion of the form:

$$Y(\boldsymbol{x}) = \sum_{n=1}^{\infty} \sqrt{\lambda_n}\psi_n(\boldsymbol{x})g_n \tag{B.1}$$

where $\{g_n\}_{n\geq 1}$, is the orthonormal sequence of i.i.d. centred Gaussian variables, $\lambda_1 \geq \lambda_2 \geq ...$, and $\psi_1, \psi_2, ...$ are, respectively, the eigenvalues and the normalized eigenfunctions of the covariance matrix such that λ_n and ψ_n solve the integral:

$$\int_S C(\boldsymbol{x}, \boldsymbol{s})\psi(\boldsymbol{s})d\boldsymbol{s} = \lambda\psi(\boldsymbol{x}) \tag{B.2}$$

with the normalization

$$\int_S \psi_n(\boldsymbol{x})\psi_m(\boldsymbol{s}) = \begin{cases} 1 & n = m \\ 0 & n \neq m \end{cases} \tag{B.3}$$

These eigenfunctions are the natural expansion of C defined by Mercer's Theorem [Mer09], such that:

$$C(\boldsymbol{x}, \boldsymbol{s}) = \sum_{n=1}^{\infty} \lambda_n\psi_n(\boldsymbol{x})\psi_n(\boldsymbol{s}) \tag{B.4}$$

Thus, for Gaussian random field, Y, on $S \subset \mathbb{R}^N$, $\{\sqrt{\lambda_n}\psi_n(\boldsymbol{x})\}$ is a complete orthonormal system in the Hilbert space H equipped by the following inner product $\langle ., . \rangle$:

$$\langle f, h \rangle_H = \sum_{n=1}^{\infty} a_n b_n \tag{B.5}$$

where $f(\boldsymbol{x}) = \sum_{n=1}^{\infty} a_n \sqrt{\lambda_n} \psi_n(\boldsymbol{x})$ and $h(\boldsymbol{x}) = \sum_{n=1}^{\infty} b_n \sqrt{\lambda_n} \psi_n(\boldsymbol{x})$, with $\sum_{n=1}^{\infty} a_n^2 < \infty$ and $\sum_{n=1}^{\infty} b_n^2 < \infty$. Notice that the coefficients a_n and b_n will be replaced by the i.i.d. Gaussian variables.
The Karhunen-Loève expansion is the general approach for simulation of Gaussian random fields that might be defined on the non-Euclidean space, or they might be non-stationary fields in the Euclidean-space. However, the Karhunen-Loève is an infinite expansion, even if the random field is isotropic. Thus, one might take a finite expansion using a finite number the eigenvalues which is not enough [AT03]. Further demonstrations can be found in [GM07].

B.2 Spectral expansion using Fourier transform

For stationary Gaussian (or non-Gaussian) random fields, the direct approach to generate such random fields is via the spectral representation approach (see chapter). Dealing with stationary Gaussian random fields using the spectral representation means that Y can be considered as a complex-valued Gaussian random field. Thus, its covariance function can be expressed as , and the eigenfunctions of $C(\boldsymbol{x}, \boldsymbol{s})$ can be established in Fourier space via complex exponentials such that:

$$\begin{aligned} \int_S C(\boldsymbol{x}, \boldsymbol{s}) e^{i\mathcal{K}\boldsymbol{s}} d\boldsymbol{s} &= \int_S C(\boldsymbol{x} - \boldsymbol{s}) e^{i\mathcal{K}\boldsymbol{s}} \\ &= e^{i\mathcal{K}\boldsymbol{x}} \int_S C(\boldsymbol{u}) e^{-i\mathcal{K}\boldsymbol{u}} \\ &= \tilde{C}(\mathcal{K}) e^{i\mathcal{K}\boldsymbol{x}} \end{aligned} \tag{B.6}$$

where $\mathcal{K}$ stands for spectral measure (frequency).
Since Y is stationary field, so the covariance function C is symmetric and $\tilde{C}(\mathcal{K})$ is the power spectral density of Y, or the Fourier transform of the autocorrelation function. Following the orthogonal expansion theorem, the real-valued Gaussian random field can be written as:

$$Y(\boldsymbol{x}) = Re\{\sum_{n=1}^{\infty} \sqrt{\tilde{C}_n(\mathcal{K})} g_n e^{i\mathcal{K}\boldsymbol{x}}\} \tag{B.7}$$

where Re stands for the real part, g_n is a complex-valued zero mean Gaussian noise. The last expansion is the inverse Fourier transform of the spectral coefficients $\sqrt{\tilde{C}_n(\mathcal{K})} g_n$. Furthermore, the sum in the expansion can be considered to finite number, when Y is defined on a finite number of points giving exact generation of Y.

B.3 Some isotropic covariance functions

In the following some isotropic positive definite [1] covariance function models depicted in [Yag87a, Mat86] are introduced as examples (see Fig. B.1) to generate stationary isotropic Gaussian random fields (see Fig. B.2). We remind that stationary Gaussian random fields with zero mean are uniquely determined by a positive definite covariance function C which depends only on the distance $\boldsymbol{\tau} = \|\boldsymbol{x} - \boldsymbol{y}\|$. The following covariance function models are parametrized by r and ν which define the correlation length and the slope of the covariance function, respectively.

– **Exponential covariance function:**

$$C(\tau;\nu,r) = \sigma^2 e^{-\left(\frac{\tau}{r}\right)^{\nu}}, \;\; 0 \leq \nu \leq 2 \tag{B.8}$$

When $\nu = 2$ the corresponding function is the known Gaussian covariance function. Note that $\nu = 0$ corresponds to the white noise with constant covariance equals to σ^2 (see Fig. B.1(a)).

– **Cauchy covariance function:**

$$C(\tau;\nu,r) = \sigma^2 \left(1 + \frac{\tau^2}{r^2}\right)^{-\nu}, \;\; \nu > 0 \tag{B.9}$$

This covariance function decays rapidly for small values of ν, but very slowly when $\nu > 2$. It is close to the exponential covariance function. Fig. B.1(b) shows different sample paths for different ν.

– **Modified Bessel covariance function:**

$$C(\tau;\nu,r) = \sigma^2 2^{\nu}\Gamma(\nu+1)\,(\omega\tau)^{-\nu}\,J_{\nu}(\omega\tau), \;\; \nu \geq (N-2)/2 \tag{B.10}$$

where J_ν is the modified Bessel function of the first kind of order ν, and $\Gamma(.)$ is the Gamma function. Notice that Bessel type functions can have negative values. Nevertheless, the covariance function is positive definite [Yag87a, Mat86] for any arbitrary integer ν. This covariance function has a damped oscillation behaviour with period $2\pi/\omega$ (see Fig. B.1(c) for different sample paths).

– **Exponentially damped cosine covariance function:**

$$C(\tau;\omega,r) = \sigma^2 Cos\,(\omega\tau)\,e^{-3\left(\frac{\tau}{r}\right)} \tag{B.11}$$

where $\nu \geq 0$. Notice that when $\omega > 0$ and $r \geq 0$, then the corresponding function is continuous and positive definite only for $N = 1$. If $\omega > 0$ and $3/\omega \geq r \geq 0$, then it will be continuous and positive definite for $N = 2$, and for $N = 3$ it should be satisfied that $\omega > 0$, $\sqrt{3}/\omega \geq r \geq 0$. This oscillating function (Fig. B.1(d)) has a period of $2\pi/\omega$.

1. C is a positive definite function on $S \times S$, if for any choice of n, $(\boldsymbol{x}_1, ..., \boldsymbol{x}_n) \in S$, and $(c_1, ..., c_n) \in \mathbb{R}$: $\sum_{i=1}^{n}\sum_{j=1}^{n} c_i c_j C(\boldsymbol{x}_i, \boldsymbol{x}_j) > 0$. Matérn [Mat86] has been shown that the covariance function C of centred, isotropic random fields on $\mathbb{R}^N$ that satisfies: $C(\boldsymbol{\tau}) \geq -C(0)/N$, $\boldsymbol{\tau} \in \mathbb{R}^N$, is never negative.

The parameter σ^2, in the last examples, denotes the correlation amplitude at the origin $C(0) = \sigma^2$. Further isotropic covariance families can be seen in [Yag87a, Mat86, Abr97].

B.4 Numerical simulation of anisotropic stationary GRFs

In the case of stationarity and anisotropy, then following the discussion in chapter 2, the covariance function will depend on the distance $\boldsymbol{\tau}_{\boldsymbol{D}} = \|\boldsymbol{x} - \boldsymbol{s}\|_{\boldsymbol{D}}$, where $\boldsymbol{D}$ is $N \times N$ positive definite matrix, and $\boldsymbol{x}, \boldsymbol{s} \in \mathbb{R}^N$.
The matrix $\boldsymbol{D}$ determines the correlation properties of the spatial structures, such as their correlation length and their directions. We take the simple case $N = 2$, then $\boldsymbol{D}$ can be written as:

$$\boldsymbol{D} = \begin{bmatrix} cos(\theta) & -sin(\theta) \\ sin(\theta) & cos(\theta) \end{bmatrix} \begin{bmatrix} c_1^2 & 0 \\ 0 & c_2^2 \end{bmatrix} \begin{bmatrix} cos(\theta) & -sin(\theta) \\ sin(\theta) & cos(\theta) \end{bmatrix}^t \tag{B.12}$$

where $\theta \in [-\pi, \pi]$ is the rotation angle, and $c_1, c_2 \in \mathbb{R}$ are, generally, the correlation length parameters, (see Fig. B.3).
we illustrate in Fig. B.4 two examples of two-dimensional anisotropic Gaussian random fields generated numerically using the anisotropic exponentially damped covariance function in $\mathbb{R}^2$, seen in Fig. B.3. The corresponding anisotropic covariance function is defined in this example such as:

$$C(\boldsymbol{d}; \theta, \omega_1, \omega_2, r_1, r_2) = \sigma^2 exp^{-3(\boldsymbol{d}^t \boldsymbol{K}^{-1} \boldsymbol{d})^{1/2}} cos((\boldsymbol{d}^t \boldsymbol{A} \boldsymbol{d})^{1/2}) \tag{B.13}$$

where σ, is the covariance amplitude at the origin ($C(0) = \sigma^2$), $\boldsymbol{d}$ is the difference vector $\boldsymbol{x} - \boldsymbol{s}$, for any $\boldsymbol{x}, \boldsymbol{s} \in S$, and

$$\boldsymbol{A} = \boldsymbol{R}_\theta \begin{bmatrix} \omega_1^2 & 0 \\ 0 & \omega_2^2 \end{bmatrix} \boldsymbol{R}_\theta^t, \quad \boldsymbol{K} = \boldsymbol{R}_\theta \begin{bmatrix} r_1^2 & 0 \\ 0 & r_2^2 \end{bmatrix} \boldsymbol{R}_\theta^t \tag{B.14}$$

where r_1, r_2 are the damping parameters, and $2\pi/\omega_1$, $2\pi/\omega_2$ are the oscillation periods, all in the orthogonal coordinates in $\mathbb{R}^2$. $\boldsymbol{R}_\theta$ is the rotation matrix given by:

$$\boldsymbol{R}_\theta = \begin{bmatrix} cos(\theta) & -sin(\theta) \\ sin(\theta) & cos(\theta) \end{bmatrix} \tag{B.15}$$

The damping coefficient should be restricted to $0 \leq r_1 \leq 3/2\omega_1$ and $0 \leq r_2 \leq 3/2\omega_2$, in order to satisfy that C is positive definite in $\mathbb{R}^2$.

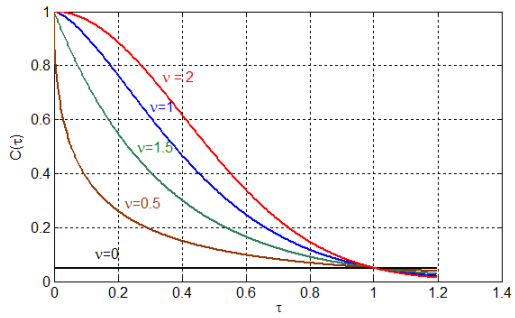

(a)

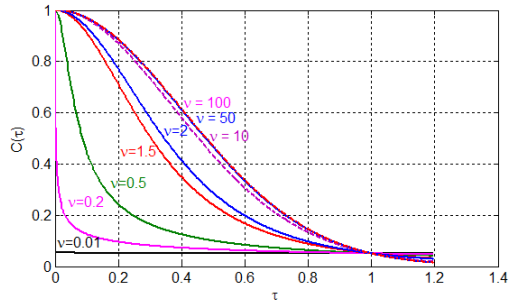

(b)

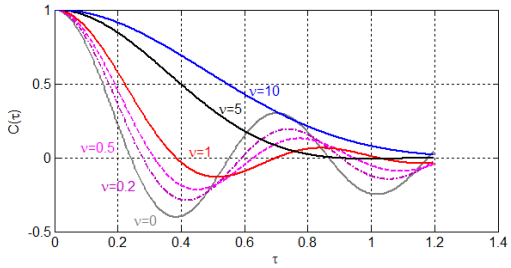

(c)

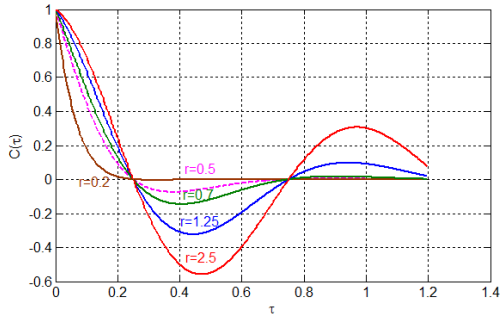

(d)

Figure B.1: Different isotropic continuous and positive definite covariance functions.(a) Exponential covariance function for $\nu = 0, 0.5, 1, 1.5$ and 2.0 with correlation length $r = 1$ for all. (b) Cauchy covariance function for $\nu = 0.01, 0.2, 0.5, 1.5, 2, 10, 50$ and 100, with correlation length $r = 1$ for all. Notice the very fast and very slow decays of the covariance function with decreased and increased ν, respectively. (c) Bessel covariance function for $\nu = 0, 0.2, 0.5, 1, 5$ and 10, with angular frequency $\omega = 2$ for all. (d) Exponentially damped cosine covariance function with damping $r = 0.2, 0.5, 0.7, 1.25$ and 2.5. The angular frequency $\omega = 1$ for all.

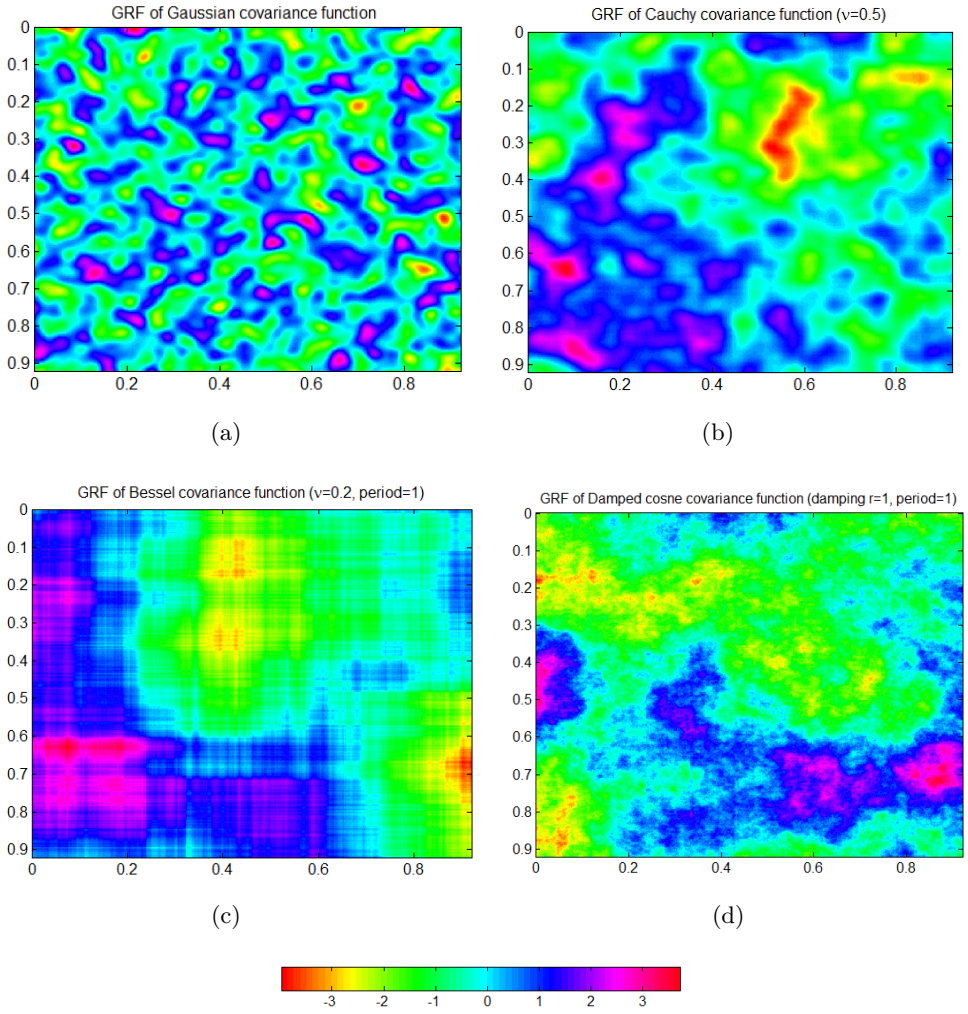

Figure B.2: Numerical simulation of stationary isotropic Gaussian random fields (GRFs) generated by Fourier transform on $[0,1]^2$ using one example of each of the four isotropic covariance function models illustrated in Fig. B.1.(a) GRF with Gaussian covariance function of $\nu = 2$ and correlation length $r = 1$. (b) GRF with Cauchy covariance function of $\nu = 0.5$ and correlation length $r = 1$. (c) GRF with Bessel covariance function of $\nu = 0.2$ and period $2\pi/\omega = 1$. (d) GRF with exponentially damped cosine covariance function of period $2\pi/\omega = 1$ and damping $r = 1$.

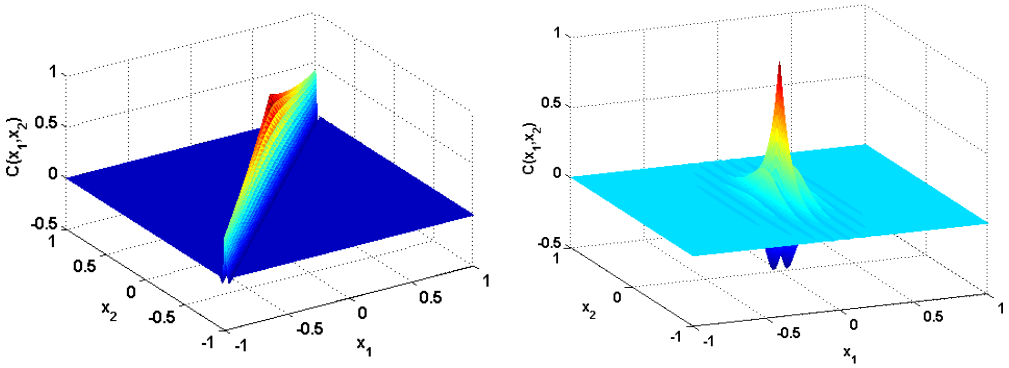

(a) (b)

Figure B.3: Examples of a two-dimensional anisotropic exponentially damped cosine covariance function with different correlation parameters. (a) Correlation rotation angle $\theta = 45°$ with damping parameters $r_1 = 100, r_2 = 0.03$, and periods $2\pi/\omega_1 = 0.01, 2\pi/\omega_2 = 15$. (b) Correlation direction $\theta = 0°$, with damping $r_1 = 0.5, r_2 = 0.2$ and period $2\pi/\omega_1 = 0.01, 2\pi/\omega_2 = 10$.

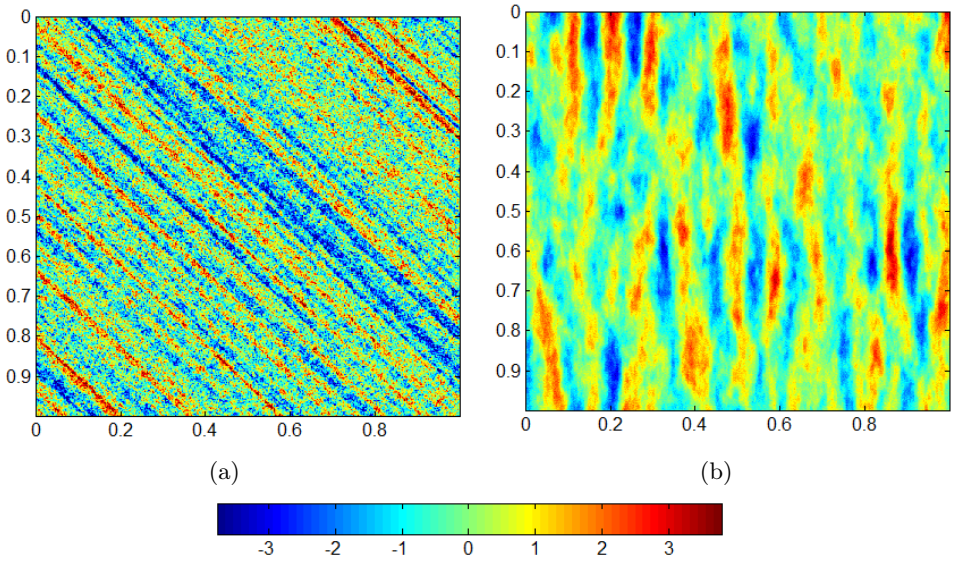

(a) (b)

Figure B.4: Numerical simulation of two-dimensional stationary anisotropic GRFs generated by the covariance functions illustrated in B.3 (a), and B.3 (b), respectively..

List of Abbreviations

pdf	probability density function
cdf	cumulative distribution function
EC	Euler Characteristic
RMS	Root Mean Square
UHMWPE	Ultra-High-Molecular-Weight Polyethylene
THA	Total Hip Arthroplasty
ISO	International Organization for Standardization
ACF	Auto-Correlation Function
LKCs	Lipschitz-Killing Curvatures
i.i.d.	independent and identically distributed

Notation Index

N	Dimension of the parameter space
$\phi(.)$	Normal pdf
$\Phi(.)$	Normal cdf
ν	The degree of freedom
T^{ν}	$t-$field with ν degrees of freedom
$t_{\nu}(.)$	The t distribution with ν degrees of freedom
t^{d}	The $d-$dimensional t variate pdf
$T_1(.)$	The scalar student's t cdf
χ^2	Squared-Chi random field
χ^2_{ν}	Squared-Chi distribution with ν degrees of freedom
$ST_{\nu;\alpha}(.)$	skew$-t$ distribution with ν degrees of freedom and skewness index α
$\mathbb{R}^N$	The $N-$dimensional Euclidean space
Wishart_N	Wishart distribution
GT^{ν}_{β}	Gaussian$-t$ distribution
$\mu(.)$	First order moment function
$C(.)$	Covariance function
Σ	Covariance kernel matrix
σ	Standard deviation
μ_Y	First order moment of Y
σ_Y	Standard deviation of Y
Λ	Second order spectral matrix
S	A compact subset of $\mathbb{R}^N$
λ	second order spectral moment
Λ_J	Second order spectral matrix
$\lambda_{i_1 \ldots i_n}$	Spectral moments
λ_{ij}	second order spectral moment
δ, α	Skewness index
β	Scale factor

Sq RMS value

Ssk skewness

Sku kurtosis

E_h The excursion set at a level h

Y A random process

$\rho_n(.)$ The $n-$dimensional EC density

$\mathcal{M}_n(.)$ The $n-$dimensional Minkowski functional

$\mathcal{L}_n(.)$ The $n-$dimensional Lipschitz-killing curvature

$\mathcal{H}_n$ Hausdorff measure of n dimension

ω_n The volume of the unit ball in $\mathbb{R}^n$

χ Euler-Poincaré characteristic

$\begin{bmatrix} n \\ m \end{bmatrix}$ Flag coefficient

χ_G Euler-Poincaré characteristic of Gaussian random field

χ_T Euler-Poincaré characteristic of t random field

detr_n The sum over principal minors

$\text{Graff}(N,k)$ The affine Grassmanian

$\dot{Y}$ The first partial derivative of Y

$A_r(.)$ The area function

$C_r(.)$ The contour function

M_h^+ The number of maxima

M_h^- The number of minima

$|.|$ Determinant

det Determinant

$\Gamma(.)$ Gamma function

$\ddot{Y}$ The second partial derivative of Y

$p_Y(.)$ The marginal pdf of Y

$P_Y(.)$ The cdf of Y

$\text{Normal}_d(.)$ $d-$variate Normal distribution

Bibliography

[AA09] M. T. Alodat and M. Y. Al-Rawwash. Skew-Gaussian random field. *J. Comput. Appl. Math.*, 232(2):496–504, October 2009.

[Abr97] Petter Abrahamsen. A review of Gaussian random fields and correlation functions. Technical Report 917, Norwegian Computing Center, Blindern, N-0314 Oslo, Norway, April 1997.

[AC99] A. Azzalini and A. Capitanio. Statistical applications of the multivariate skew normal distribution. *Journal Of The Royal Statistical Society Series B*, 61(3):579–602, 1999.

[AC03] Adelchi Azzalini and Antonella Capitanio. Distributions generated by perturbation of symmetry with emphasis on a multivariate skew "t"-distribution. *Journal Of The Royal Statistical Society Series B*, 65(2):367–389, 2003.

[Adl81] Robert J. Adler. *The Geometry of Random Fields*. Wiley, Chichester, UK, June 1981.

[Adl08] Robert Adler. Some new random field tools for spatial analysis. *Stochastic Environmental Research and Risk Assessment*, 22:809–822, 2008.

[AF33] E. J. Abbott and F. A. Firestone. Specifying surface quality: a method based on accurate measurment and comparision. *Mechanical Engineering*, 55:569–572, 1933.

[AF81] R.J. Adler and D. Firman. A non-gaussian model for random surfaces. *Philosophical Transactions of the Royal Society of London. Series A, Mathematical and Physical Science*, 303(1479):433–462, 1981.

[AGGP13] O. Ahmad, Y. Gavet, J. Geringer, and J.-C. Pinoli. Roughness varaibility estimation of microscopic surfaces during engineering wear process–application to total hip implant. In *In 11th International Conference on Quality Control by Artificial Vision, Fukuoka, Japan*, 2013.

[AH76] Robert J. Adler and A. M. Hasofer. Level crossings for random fields. *The Annals of Probability*, 4(1):1–12, 1976.

[AMR96] Robert Adler, Peter Müller, and B. L. Rozovskii. *Stochastic Modelling in Physical Oceanography*, volume 42. Birkhäuser, Boston, softcover reprint of the original 1st ed. 1996 edition, September 1996.

[AP12] Ola Suleiman Ahmad and Jean-Charles Pinoli. On the linear combination of the gaussian and student-t random fields and the geometry of its

excursion sets. In *Lecture Notes in Engineering and Computer Science: Proceedings of the World Congress on Engineering and Computer Science 2012, WCECS 2012, 24-26 October, San Francisco, USA*, pages 1–5, 2012.

[AP13a] Ola Ahmad and Jean-Charles Pinoli. On the linear combination of the gaussian and student's t random field and the integral geometry of its excursion sets. *Statistics & Probability Letters*, 83(2):559 – 567, 2013.

[AP13b] Ola Suleiman Ahmad and Jean-Charles Pinoli. Lipschitz-killing curvatures of the excursion sets of skew student' s t random fields. *Stochastic Models*, 29(2):273–289, 2013.

[AP13c] Ola Suleiman Ahmad and Jean-Charles Pinoli. Lipschitz-killing curvatures of the excursion sets of skew student-t random fields. In *2nd Annual International Conference on Computational Mathematics, Computational Geometry & Statistics*, volume 1, Feb 2013.

[ASZ+08] S. Affatato, M. Spinelli, M. Zavalloni, C. Mazzega-Fabbro, and M. Viceconti. Tribology and total hip joint replacement: Current concepts in mechanical simulation. *Medical Engineering & Physics*, 30(10):1305 – 1317, 2008.

[AT03] R. J. Alder and J. E. Taylor. *Random fields and their geometry.* Birkhäuser, Boston, 2003.

[AT07] R. J. Adler and Jonathan Taylor. *Random Fields and Geometry.* Springer, Berlin, 1 edition, June 2007.

[AT11] R.J. Adler and J.E. Taylor. *Topological complexity of smooth random functions: École d'Été de Probabilités de Saint-Flour XXXIX-2009.* Springer Berlin Heidelberg, july 2011.

[ATW11] Robert J Adler, Jonathan E Taylor, and Keith J Worsley. *Applications of Random Fields and Geometry: Foundations and Case Studies.* Number -. Springer-Verlag, Berlin, Heidelberg, 2011.

[AWC02] Yong Ao, Q.Jane Wang, and Penny Chen. Simulating the worn surface in a wear process. *Wear*, 252(1-2):37 – 47, 2002.

[BGG+85] G. Bousquet, D. Gazielly, P. Girardin, J.L. Debiesse, M. Relave, and A. Israeli. The ceramic coated cementless total hip arthroplasty. basic concepts and surgical technique. *Journal of Orthopaedic surgery*, 1:15–28, 1985.

[Bhu99] Bharat Bhushan. *Principles and Applications of Tripology.* Wiley-Interscience, 1 edition, March 1999.

[Bla36] Wilhelm Blaschke. *Integralgeometrie. erstes Heft.* B. G. Teubner, Leipzig; Berlin, 1936.

[Bla06] Françoise Blateyron. New 3D parameters and filtration techniques for surface metrology. http://www.qualitymag.com/articles/85037-new-3d-parameters-and-filtration-techniques-for-surface-metrology, 2006.

[BLCG10] Rodrigo M. Basso, Víctor H. Lachos, Celso Rômulo Barbosa Cabral, and Pulak Ghosh. Robust mixture modeling based on scale mixtures of skew-normal distributions. *Computational Statistics & Data Analysis*, 54(12):2926 – 2941, 2010.

[Boc33] S. Bochner. Monotone funktionen stieltjessche integrale and harmonishe analyse. *Mathematische Annalen*, 108:378, 1933.

[Bra00] Ronald Newbold Bracewell. *The Fourier transform and its applications.* McGraw Hill, 2000.

[Cao97] Jin Cao. *Excursion sets of random fields with applications to human brain mapping.* PhD thesis, Departement of Mathematics and Statistics, McGill University, Quebec, Canada, 1997.

[CLP12] Celso Rômulo Barbosa Cabral, Víctor Hugo Lachos, and Marcos O. Prates. Multivariate mixture modeling using skew-normal independent distributions. *Computational Statistics & Data Analysis*, 56(1):126 – 142, 2012.

[Cor04] Zygo Corporation. Metropro reference guid, 2004.

[Cos00] Michael Allan Costa. *Fractal description of rough surfaces for haptic display.* PhD thesis, Stanford University, 2000.

[CW99] Jin Cao and Keith J. Worsley. The detection of local shape changes via the geometry of hotelling's T^2 fields. *The Annals of Statistics*, 27(3):925–942, June 1999.

[DS95] W. P. Dong and K. J. Stout. An integrated approach to the characterization of surface wear i: Qualitative characterization. *Wear*, 181-183(Part 2):700 – 716, 1995. 10th International Conference on Wear of Materials.

[DSS94] W.P. Dong, P.J. Sullivan, and K.J. Stout. Comprehensive study of parameters for characterising three-dimensional surface topography: Iii: Parameters for characterising amplitude and some functional properties. *Wear*, 178(1-2):29–43, 1994.

[FPDF09] C.G. Figueiredo-Pina, P.A. Dearnley, and J. Fisher. UHMWPE wear response to apposing nitrogen s-phase coated and uncoated orthopaedic implant grade stainless steel. *Wear*, 267(5-8):743 – 752, 2009.

[GBF11] J. Geringer, B. Boyer, and F. Farizon. Understanding the dual mobility concept for total hip arthroplasty. investigations on a multiscale analysis-highlighting the role of arthrofibrosis. *Wear*, 271(9 - 10):2379 – 2385, 2011.

[GBFF10] Jean Geringer, Bertrand Boyer, Bernard Forest, and Frédéric Farizon. Concept de double mobilité pour les prothéses totales de hanche: analyses multi-échelles de son fonctionnement. In *Materiaux 2010 – Nantes, France*, 2010.

[Gen04] Marc G. Genton. *Skew-Elliptical Distributions and Their Applications: A Journey Beyond Normality.* Taylor & Francis, London, UK, July 2004.

[GM07] Stefanou George and Papadrakakis Manolis. Assessment of spectral representation and karhunen-loève expansion methods for simulation of gaussian stochastic fields. *Computer methods in applied mechanics and engineering*, 196(21-24):2465–2477, 2007.

[GW66] J. A. Greenwood and J. B. P. Williamson. Contact of nominally flat surfaces. *Proceedings of the Royal Society of London. Series A, Mathematical and Physical Sciences*, 295(1442):300–319, December 1966.

[GWG+08] Shirong Ge, Shibo Wang, Norm Gitis, Michael Vinogradov, and Jun Xiao. Wear behavior and wear debris distribution of uhmwpe against si3n4 ball in bi-directional sliding. *Wear*, 264(7-8):571 – 578, 2008.

[Had57] H. Hadwiger. *Vorlesungen über Inhalt, Oberfläche und Isoperimetrie*, volume 93. Springer-Verlag, Berlin, Heidelberg, 1957.

[Has78] A. M. Hasofer. Upcrossings of random fields. *Advances in Applied Probability*, 10:14–21, March 1978.

[HS02] D Hug and R. Schneider. Kinematic and crofton formulae of integral geometry: recent variants and extensions. In *In C. Barceló i Vidal, editor,* Homenatge al Proffessor Lus Santaló i Sors, pages 51–80. Universitat de Girona, Girona, Spain, 2002.

[HT92] Y.Z. Hu and K. Tonder. Simulation of 3d random rough surface by 2d digital filter and fourier analysis. *International Journal of Machine Tools and Manufacture*, 32(1-2):83 – 90, 1992.

[ISO97] ISO 4287. Geometrical product specification (GPS) - surface texture: profile method, 1997.

[ISO02] ISO 14242-1. Implants for surgery – wear of total hip-joint prostheses – part 1: Loading and displacement parameters for wear-testing machines and corresponding environmental conditions for test, 2002.

[ISO05] ISO TC 213 WORKGROUP 16. Geometrical products specifications (GPS) surface texture: Areal part 2: Terms, definitions and surface texture parameters, 2005. standared proposal n756, 2005.

[ISO06] ISO/TS CD 25178-2. Geometrical product specification (GPS) — surface texture: areal—part 2: terms, definitions and surface texture parameters., 2006.

[JBL02] Bruno Josso, David R. Burton, and Michael J. Lalor. Frequency normalised wavelet transform for surface roughness analysis and characterisation. *Wear*, 252(5-6):491–500, March 2002.

[JBS01a] X. Q. Jiang, L. Blunt, and K. J. Stout. Lifting wavelet for three-dimensional surface analysis. *International Journal of Machine Tools and Manufacture*, 41(13-14):2163 – 2169, 2001.

[JBS01b] X.Q. Jiang, L. Blunt, and K.J. Stout. Application of the lifting wavelet to rough surfaces. *Precision Engineering*, 25(2):83 – 89, 2001.

[Joh49] N. L. Johnson. Systems of frequency curves generated by methods of translation. *Biometrika*, 36(1-2):149–176, January 1949.

[Jon08] M. C. Jones. The t family and their close and distant relations. *Journal of the Korean Statistical Society*, 37(4):293–302, 2008.

[JP68] M. Kubo J. Pekleink. A basic study of a three-dimensional assessment of the surface generated in a manufacturing process. *Annals of the CIRP*, 16:235–242, 1968.

[JSW08] X. Jiang, P. Scott, and D. Whitehouse. Wavelets and their applications for surface metrology. *CIRP Annals - Manufacturing Technology*, 57(1):555 – 558, 2008.

[JSWB07a] X Jiang, P.J Scott, D.J Whitehouse, and L Blunt. Paradigm shifts in surface metrology. part i. historical philosophy. *Proceedings of the Royal Society A: Mathematical, Physical and Engineering Science*, 463(2085):2049 – 2070, 2007.

[JSWB07b] X Jiang, P.J Scott, D.J Whitehouse, and L Blunt. Paradigm shifts in surface metrology. part II. the current shift. *Proceedings of the Royal Society A: Mathematical, Physical and Engineering Science*, 463(2085):2071 – 2099, 2007.

[JZS+08] Xiangqian Jiang, Wenhan Zeng, Paul Scott, Jianwei Ma, and Liam Blunt. Linear feature extraction based on complex ridgelet transform. *Wear*, 264(5-6):428 – 433, 2008.

[Kur04] Steven M. Kurtz. *The UHMWPE Handbook: Ultra-High Molecular Weight Polythylene in Total Joint Replacement.* Elsevier, 2004.

[Lew01] Gladius Lewis. Properties of crosslinked ultra-high-molecular-weight polyethylene. *Biomaterials*, 22(4):371 – 401, 2001.

[LLBG10] V. H. Lachos, F. V. Labra, H. Bolfarine, and Pulak Ghosh. Multivariate measurement error models based on scale mixtures of the skew normal distribution. *Statistics*, 44(6):541–556, 2010.

[LXLZ05] Yuan Lin, Xu Rui Xiao, Xue Ping Li, and Xiao Wen Zhou. Wavelet analysis of the surface morphologic of nanocrystalline tio2 thin films. *Surface Science*, 579(1):37 – 46, 2005.

[LZCM98] S-H. Lee, H. Zahouani, R. Caterini, and T.G. Mathia. Morphological characterisation of engineered surfaces by wavelet transform. *International Journal of Machine Tools and Manufacture*, 38(5-6):581 – 589, 1998.

[Ma07] Chunsheng Ma. Stationary random fields in space and time with rational spectral densities. *IEEE Trans. Inf. Theor.*, 53(3):1019–1029, March 2007.

[Mat86] B. Matérn. *Spatial Variation*. Springer, 2nd ed. edition, December 1986.

[MC69] Marston Morse and Stewart S. Cairns. *Critical point theory in global analysis and differential topology, Volume 33: An introduction*. Academic Press INC. New York, USA, 1st edition, February 1969.

[Mec98] Klaus R. Mecke. *Integral Geometry in Statistical Physics*, volume 12. International Journal of Modern Physics, 1998.

[Mec00] Klaus Mecke. Additivity, convexity, and beyond: Applications of minkowski functionals in statistical physics. In Klaus Mecke and Dietrich Stoyan, editors, *Statistical Physics and Spatial Statistics*, volume 554 of *Lecture Notes in Physics*, pages 111–184. Springer, Berlin, Heidelberg, 2000.

[Mer09] James Mercer. Functions of positive and negative type and their connection with the theory of integral equations. *Philos. Trans. Roy. Soc. London*, 209:415–446, 1909.

[MN68] Benoit B. Mandelbrot and John W. Van Ness. Fractional brownian motions, fractional noises and applications. *SIAM Review*, 10(4):422–437, 1968.

[MRS10] K.K. Manesh, B. Ramamoorthy, and M. Singaperumal. Numerical generation of anisotropic 3D non-gaussian engineering surfaces with specified 3D surface roughness parameters. *Wear*, 268(11-12):1371 – 1379, 2010.

[Nay73] P.R. Nayak. Random process model of rough surfaces in plastic contact. *Wear*, 26(3):305 – 333, 1973.

[NBMI06] D. Najjar, M. Bigerelle, H. Migaud, and A. Iost. About the relevance of roughness parameters used for characterizing worn femoral heads. *Tribology International*, 39(12):1527 – 1537, 2006.

[NT-] Wyko NT-9100. Wyko nt9100.

[PG07] Y. F. Peng and Y. B. Guo. An adhesion model for elastic-plastic fractal surfaces. *Journal of Applied Physics*, 102(5):053510 –053510–7, September 2007.

[PS99] P Podsiadlo and G.W Stachowiak. Applications of hurst orientation transform to the characterization of surface anisotropy. *Tribology International*, 32(7):387 – 392, 1999.

[PS00] P. Podsiadlo and G. W. Stachowiak. Scale-invariant analysis of wear particle surface morphology i: Theoretical background, computer implementation and technique testing. *Wear*, 242(1-2):160–179, July 2000.

[PS02] P. Podsiadlo and G.W. Stachowiak. Hybrid Fractal-Wavelet method for characterization of tribological Surfaces-a preliminary study. *Springer-Tribology Letters*, 13(4):241–250, 2002.

[PS03] P. Podsiadlo and G. W. Stachowiak. Fractal-wavelet based classification of tribological surfaces. *Wear*, 254(11):1189–1198, October 2003.

[PS05] P. Podsiadlo and G.W. Stachowiak. Development of advanced quantitative analysis methods for wear particle characterization and classification to aid tribological system diagnosis. *Tribology International*, 38(10):887 – 897, 2005. Ferrography and Friends - Pioneering Developments in Wear Debris Analysis.

[Rei11] R. Reizer. Simulation of 3d gaussian surface topography. *Wear*, 271(3-4):539 – 543, 2011.

[Rus94] John C. Russ. *Fractal Surfaces*. Springer, February 1994.

[San76] Luis Antonio Santalo. *Integral geometry and geometric probability*, volume 12. Addison-Wesley Pub. Co., Advanced Book Program, November 1976.

[Sch06] Jochen Schmähling. *Statistical characterization of technical surface microstructure*. PhD thesis, Ruprecht-Karls University, Heidelberg, 2006.

[Sco04] Paul J. Scott. Pattern analysis and metrology: the extraction of stable features from observable measurements. *Proceedings of the Royal Society of London. Series A: Mathematical, Physical and Engineering Sciences*, 460:2845 –2864, octobre 2004.

[Sco09] Paul J. Scott. Feature parameters. *Wear*, 266(5-6):548 – 551, 2009.

[SJ95] J. S. Siopack and H. E. Jergesen. Total hip arthroplasty. *Western Journal of Medicine*, 162(3):243–249, March 1995.

[SJLG03] Philippe Saint-Jean, Jean-Marc Lina, and Bernard Goulard. Maxima of the continuous wavelet transform of correlated data. *Applied and Computational Harmonic Analysis*, 15(1):1 – 17, 2003.

[SP01] G. W. Stachowiak and P. Podsiadlo. Characterization and classification of wear particles and surfaces. *Wear*, 249(3-4):194–200, May 2001.

[SP08] Gwidon Stachowiak and Pawel Podsiadlo. 3-D characterization, optimization, and classification of textured surfaces. *Tribology Letters*, 32(1):13–21, 2008.

[SSD+93] K.J. Stout, P.J. Sullivan, W.P. Dong, E. Manisah, N. Luo, T. Mathia, and H. Zahouani. The development of methods for the characterization of roughness in three dimensions. Technical report, Commission of the European Communities, 1993.

[SSSW03] K Shafie, B. Sigal, D. O. Siegmund, and K. J. Worsley. Rotation space random fields with an application to fmri data. *The Annals of Statistics*, 31(6):1732–1771, 2003.

[ST78] R. S. Sayles and T. R. Thomas. Surface topography as a nonstationary random process. *Nature*, 271(5644):431–434, February 1978.

[SW08] Rolf Schneider and Wolfgang Weil. *Stochastic and Integral Geometry*. Springer, 1 edition, October 2008.

[TA03] J. E. Taylor and R. J. Adler. Euler characteristic for Gaussian fields on manifolds. *The Annals of Probability*, 31(2):533–563, 2003.

[Tay08] J. E. Taylor. Random fields of multivariate test statistics, with applications to shape analysis. *The Annals of Statistics*, 36(1):1–27, February 2008.

[TRA99] T.R Thomas, B.-G Rosén, and N Amini. Fractal characterisation of the anisotropy of rough surfaces. *Wear*, 232(1):41 – 50, 1999.

[Van83] Erik Vanmarcke. *Random Fields: Analysis and Synthesis*. The MIT Press, March 1983.

[Wal69] J. Wallach. Surface topography description and measurements. In *Proceedings of ASME Winter Annual Meeting, Nov. 16-21*, pages 1–22, 1969.

[WEP+98] A Wang, A Essner, V.K Polineni, C Stark, and J.H Dumbleton. Lubrication and wear of ultra-high molecular weight polyethylene in total joint replacements. *Tribology International*, 31(1-3):17 – 33, 1998.

[Whi94] D. Whitehouse. *Handbook of Surface Metrology*. Institute of Physics Publications, Bristol, 1994.

[Whi02] D. J. Whitehouse. Fractal or fiction. *Wear*, 252(9-10):842–843, 2002.

[WM97] Yiding Wang and Kee S. Moon. A methodology for the multi-resolution simulation of grinding wheel surface. *Wear*, 211(2):218 – 225, 1997.

[Wor94] K. J. Worsley. Local maxima and the expected euler characteristic of excursion sets of χ^2, F and t fields. *Advances in Applied Probability*, 26(1):13–42, 1994.

[Wor95] K.J. Worsley. Boundary corrections for the expected euler characteristic of excursion sets of random fields, with an application to astrophysics. *Advances in Applied Probability*, 27:943–959, 1995.

[WPS10] M. Wolski, P. Podsiadlo, and G.W. Stachowiak. Applications of the variance orientation transform method to the multiscale characterization of surface roughness and anisotropy. *Tribology International*, 43(11):2203–2215, November 2010.

[Wu00] Jiunn-Jong Wu. Simulation of rough surfaces with fft. *Tribology International*, 33(1):47 – 58, 2000.

[Wya02] J. C. Wyant. White light interferometry. *Proceedings of SPIE*, 4737:98–107, 2002.

[Yag87a] A. M. Yaglom. *Correlation Theory of Stationary and Related Random Functions: Volume I: Basic Results*. Springer, Berlin, 1 edition, June 1987.

[Yag87b] A. M. Yaglom. *Correlation theory of stationary and related random functions. Volume II: Supplementary Notes and References*. Springer, Berlin, 1st edition, November 1987.

[ZVL98] H. Zahouani, R. Vargiolu, and J. L. Loubet. Fractal models of surface topography and contact mechanics. *Mathematical and Computer Modelling*, 28(4-8):517 – 534, 1998.

[ZZ04] Lixian Zhang and Ya-Pu Zhao. Adhesion of rough surfaces with plastic deformation. *Journal of Adhesion Science and Technology*, 18(6):715–729, 2004.

École Nationale Supérieure des Mines
de Saint-Étienne

NNT : 2013 EMSE 0704

Ola AHMAD

STOCHASTIC REPRESENTATION AND ANALYSIS OF ROUGH SURFACE TOPOGRAPHY BY RANDOM FIELDS AND INTEGRAL GEOMETRY

Application to the UHMWPE cup involved in total hip arthroplasty

Speciality: Image, Vision, Signal

Keywords: Random Fields; Integral Geometry; Excursion sets; Intrinsic Volumes; Roughness; Surface Topography; Simulation; Characterization; Statistical Analysis; Wear; UHMWPE (Ultra-High-Molecular-Weight Polyethylene).

Abstract:

Surface topography is, generally, composed of many length scales starting from its physical geometry, to its microscopic or atomic scales known by roughness. The spatial and geometrical evolution of the roughness topography of engineering surfaces avail comprehensive understanding, and interpretation of many physical and engineering problems such as friction, and wear mechanisms during the mechanical contact between adjoined surfaces. Obviously, the topography of rough surfaces is of random nature. It is composed of irregular hills/valleys being spatially correlated. The relation between their densities and their geometric properties are the fundamental topics that have been developed, in this research study, using the theory of random fields and the integral geometry.

An appropriate random field model of a rough surface has been defined by the most significant parameters, whose changes influence the geometry of its excursion. The excursion sets were quantified by functions known as intrinsic volumes. These functions have many physical interpretations, in practice. It is possible by deriving their analytical formula to estimate the parameters of the random field model being applied on the surface, and for statistical analysis investigation of its excursion sets. These subjects have been essentially considered in this thesis. Firstly, the intrinsic volumes of the excursion sets of a class of mixture models defined by the linear combination of Gaussian and t random fields, then for the skew-t random fields are derived analytically. They have been compared and tested on surfaces generated by simulations. In the second stage, these random fields have been applied to real surfaces measured from the UHMWPE component, involved in application of total hip implant, before and after wear simulation process. The primary results showed that the skew-t random field is more adequate, and flexible for modelling the topographic roughness. Following these arguments, a statistical analysis approach, based on the skew-t random field, is then proposed. It aims at estimating, hierarchically, the significant levels including the real hills/valleys among the uncertain measurements. The evolution of the mean area of the hills/valleys and their levels enabled describing the functional behaviour of the UHMWPE surface over wear time, and indicating the predominant wear mechanisms.

École Nationale Supérieure des Mines
de Saint-Étienne

NNT : 2013 EMSE 0704

Ola AHMAD

MODÉLISATION STOCHASTIQUE ET ANALYSE DE TOPOGRAPHIE DE SURFACES RUGEUSES PAR CHAMPS ALÉATOIRES ET GÉOMÉTRIE INTÉGRALE

Application aux cupules à double mobilité pour prothèse totale de hanche

Spécialité: Image, Vision, Signal

Mots clefs : Champs Aléatoires; Géométrie Intégrale; Ensembles de Niveaux; Volumes Intrinsèques; Rugosité ; Topographie Surfacique; Simulation; Caractérisation; Analyse Statistique; Usure Mécanique; UHMWPE (Ultra-High-Molecular-Weight Polyéthylène).

Résumé :

La topographie d'une surface se compose généralement de plusieurs échelles, depuis l'échelle macroscopique (sa géométrie physique), jusqu'aux échelles microscopiques ou atomiques appelées rugosité. L'évolution spatiale et géométrique de la rugosité fournit une description plus complète de la surface, et une interprétation physique de certains problèmes importants tels que le frottement et les mécanismes d'usure pendant le contact mécanique entre deux surfaces. La topographie d'une surface rugueuse est de nature aléatoire, ce qui traduit par des altitudes spatialement corrélées, appelées pics et vallées. La relation entre leurs densités de probabilité et leurs propriétés géométriques sont les aspects fondamentaux qui ont été développés dans cette thèse, en utilisant la théorie des champs aléatoires et la géométrie intégrale.

Un modèle aléatoire approprié pour représenter une surface rugueuse a été mis en place et étudié au moyen des paramètres les plus significatifs, dont les changements influencent la géométrie des ensembles de niveaux (excursion sets) de cette surface. Les ensembles de niveaux ont été quantifiés par des fonctionnelles connues sous le nom de fonctionnelles de Minkowski, ou d'une manière équivalente sous le nom de volumes intrinsèques. Dans un premier temps, les volumes intrinsèques des ensembles de niveaux sont calculés analytiquement sur une classe de modèles mixtes, qui sont définis par la combinaison linéaire d'un champ aléatoire Gaussien et d'un champ de t-student (t-field), et ceux d'une classe de champs aléatoires asymétriques appelés skew-t. Ces volumes sont comparés et testés sur des surfaces produites par des simulations numériques. Dans un second temps, les modèles aléatoires proposés ont été appliqués sur des surfaces réelles acquises à partir d'une cupule d'UHMWPE (provenant d'une prothèse totale de hanche) avant et après les processus d'usure. Les résultats ont montré que le champ aléatoire skew-t est un modèle mieux approprié pour décrire la rugosité de surfaces usées, contrairement aux modèles adoptés dans la littérature. Une analyse statistique, basée sur le champ aléatoire skew-t, est ensuite proposée pour détecter les niveaux des pics/vallées de la surface usée et pour décrire le comportement et la fonctionnalité de la surface usée.